

Optical properties of metallic nanoparticles and metallic nanocomposite materials

Mohammed Alsawafta

A Thesis
in
The Department
of
Physics

Presented in Partial Fulfillment of the Requirements
For the Degree of
Doctor of Philosophy (Physics) at
Concordia University
Montreal, Quebec, Canada

August 2012

© Mohammed Alsawafta, 2012

ABSTRACT

Optical properties of metallic nanoparticles and metallic nanocomposite materials

Mohammed Najim Alsawafta, Ph.D.

Concordia University, 2012

The optical behaviour of both gold and silver nanoparticles has been studied in both experimental and theoretical aspects. In the theoretical part of our thesis, to contribute to a better understanding of particles of various shapes and configurations, the versatile Discrete Dipole Approximation (DDA) has been employed to simulate in depth the absorption spectra of single isolated oriented nanoparticles of different symmetry (nanocube, nanobar and nanoellipsoid). The effect of the plasmonic coupling and the size of spherical particles assemblies on their optical response have also been addressed. It was shown that the plasmonic coupling in the interacting particles in close proximity configuration disturbs the homogenous distribution of surface charges and results in splitting the plasmonic band into two bands. The excitations of two different bands (longitudinal and transverse bands) have been also observed in the absorption spectra of many fold symmetry particles. The diversity of the polarization factors along different symmetry axis was established as the main key for observing several bands. Thus the importance of particle shape and the different interesting possibilities offered by this single factor has been well demonstrated in the DDA calculations performed while our treatment of ensembles of nanospheres showed in detail the effect of interacting particles on the overall optical properties of actual samples.

In the experimental part of this thesis, a first part is devoted to the study of the influence of dielectric host material on the optical properties of gold nanoparticles. For this purpose, gold, -poly(methyl methacrylate) (PMMA) and -gelatin nanocomposite materials have been prepared by an in-situ method. Two reduction methods (photochemical and chemical) were used to reduce the gold salt in the presence of the polymer matrix. Firstly, annealed and non annealed samples were prepared by different photochemical methods (UV-, thermal-, and MW-irradiation). Gold-

poly(methyl methacrylate) nanocomposites were prepared by irradiating spin-coated films containing the polymer and the gold precursor dissolved in acetone. The reduction of gold ions resulted in the formation of gold that nucleated and grew within the polymer films. It was shown that, depending on the energy source, gold nanoparticles with different shapes could be formed. The nanocomposites prepared through the photochemical methods, showed a low sensitivity toward the environment. However, by annealing the samples at temperatures well above the glass transition temperature of the polymer, the response to dielectric environment appeared to be enhanced significantly. The increased sensitivity of the annealed sample (increase the surface particle density) was accounted for by the increased mobility of both polymer chains and gold nanoparticles in the rubbery state of the material and the presence of the monomer. The results showed that, by using adequate post-synthesis heat treatments, gold-polymer nanocomposites could be used as plasmonic sensing platforms.

Secondly, gold–gelatin bionanocomposite films were prepared by the reduction of gold ions by sodium borohydride in an aqueous solution. It was shown that both the solution and the films on glass substrates contained entrapped hydrogen micro- and nanobubbles with diameters in the range of 200 nm–3 μ m. The composite films having micro- and nanobubble inclusions have been found to be very stable. The optical properties of gold nanoparticles in the presence of gelatin and hydrogen nanobubbles were measured and simulated by using the discrete dipole approximation (DDA) method. The calculated localized surface plasmon resonance band was found in agreement with the experimental band position only when the presence of hydrogen bubbles around the gold nanoparticles was taken into account. The different morphological features engendered by the presence of the bubbles in the film (gelatin receptacles for the nanoparticles, gelatin hemispheres raised by the bubbles under the surface, cavities on the surface of the film, etc) are potential candidates for many applications.

Acknowledgments

I would like to express my sincere gratitude to my advisor Prof. Truong Vo-Van for the continuous support of my Ph.D study and research, for his patience, motivation, enthusiasm, and immense guidance. I could not have imagined having a better advisor and mentor for my Ph.D study. Throughout my thesis-writing period, he provided encouragement, sound advices and lots of good ideas.

I also wish to thank my Co-supervisor Prof. Sushil K. Misra for his detailed and constructive comments, and for his important support throughout this work.

I am also extremely indebted to Dr. Simona Badilescu for providing valuable advices, constructive criticism and extensive discussions about my experimental work.

I also thank Prof. Muthu Packirisamy for allowing me the room to work in my own way. I am grateful to him for offering the necessary research equipments.

Besides my advisors, I would like to thank the other members of my thesis committee, namely Prof. Mariana Frank, Dr. Valter Zazubovich and Prof. Ricardo Izquierdo for their encouragement, pertinent comments and questions.

I'm indebted to B. T. Draine and P. J. Flatau for the free DDSCAT 7.1 code.

I want to thank all of my group members especially Mamoun Wahbeh for his willingness to discuss the simulation of the optical properties of metallic nanostructures, Hamid Sadabadi for his encouragement and sharing the literature.

DEDICATION

TO MY PARENTS

Table of contents

TABLES OF FIGURES	xi
--------------------------------	----

CHAPTER ONE	1
--------------------------	---

Introduction

1.1 Background and thesis overview.....	2
1.1.1 Modeling of the absorption spectrum of metallic spherical nanoparticles arranged in planar hexagonal arrays.....	2
1.1.2 Modeling of the absorption spectrum of metallic nanoparticles with many symmetry axes.....	3
1.1.3 Effect of the physical host material on the optical properties of gold-polymer nanocomposite materials.....	5
1.2 Structure of the thesis.....	8

CHAPTER TWO	10
--------------------------	----

Localized surface plasmonic resonance of metallic nanoparticles

2.1 Nanoscale materials <i>versus</i> bulk materials.....	10
2.2 Basic idea of the plasmonic resonance.....	11
2.3 Types of electron resonance.....	12
2.4 LSPR modes of sub-wavelength noble metallic nanoparticles.....	13
2.5 Free electron gas model: Drude's theory.....	14
2.6 Tunability of the LSPR properties.....	18
2.6.1 Dependence on the nanostructure size.....	18
2.6.1.1 Size effect on the plasmon oscillations.....	18
2.6.1.2 Size-corrected dielectric function.....	20
2.6.2 Dependence on the dielectric function of the host material.....	21
2.6.3 Dependence on the orientation of the particles in the incident light.....	22
2.6.4 Dependence on the morphology of the nanoparticle.....	23
2.6.5 Effect of the coupling in the nearby nanoparticle.....	24

2.7	Conclusions.....	25
-----	------------------	----

CHAPTER THREE	26
----------------------------	-----------

Discrete dipole approximation

3.1	Basic ideas of DDA.....	26
3.2	Mathematical description of DDA.....	28
3.3	What does DDA calculate?.....	30
3.4	Application and validity of DDA.....	30
3.5	Conclusions.....	32

CHAPTER FOUR	34
---------------------------	-----------

Optical properties of metallic nanoparticles

4.1	Optical properties of spherical nanoparticles.....	34
4.1.1	Simulated absorption spectrum of the single isolated ultrafine spherical particle....	35
4.1.2	Effect of plasmonic coupling on the optical properties of ultrafine spherical particles arranged in 2D arrays.....	37
4.1.2.1	Target geometry of the 2D arrays.....	38
4.1.2.2	Target orientation relative to the incident light.....	39
4.1.2.3	Absorption efficiency of the ultrafine particles arranged in a hexagonal arrays.....	40
4.1.2.4	Effect of the array size on the optical properties of particles.....	41
4.2	Optical response of anisotropic nanoparticles.....	42
4.2.1	Morphology and structural parameters of the targets.....	43
4.2.2	Orientation of the target.....	45
4.2.3	Optical properties of an isolated gold nanocube.....	45
4.2.4	Optical properties of an isolated nanobar.....	48
4.2.4.1	Effect of orientation on the optical response of the nanobar.....	48
4.2.4.2	Effect of the length distributions on the optical response of the ellipsoidal nanoparticles.....	49
4.2.5	Optical properties of an isolated nanoellipsoid.....	50

4.2.5.1	Effect of orientation on the optical response of the ellipsoidal nanoparticles.....	50
4.2.5.2	Effect of the length distribution on the optical response of the ellipsoidal nanoparticles.....	56
4.3	Conclusions.....	57

CHAPTER FIVE..... 59

**Optical properties of gold- poly(methyl methacrylate)
nanocomposite films**

5.1	Synthetic technique of gold-PMMA nanocomposite films.....	60
5.1.1	Experimental details.....	61
5.1.1.1	Materials and methods.....	61
5.1.1.2	Preparation the nanocomposite materials.....	62
5.2	Results and discussion.....	62
5.2.1	UV photo-reduction.....	62
5.2.2	Microwave-assisted reduction.....	65
5.2.3	Thermal reduction.....	66
5.2.4	Effect of annealing temperature on the surface particles density.....	67
5.2.5	Refractive index sensitivity measurements.....	69
5.2.6	Biosensing experiments by using LSPR nanosensor.....	71
5.2.7	Comparison between the observed and simulated LSPR band in gold-PMMA Nanocomposite.....	73
5.3	Conclusions.....	74

CHAPTER SIX..... 76

**Optical and surface properties of gold–gelatin bio-nanocomposite
films**

6.1	Experimental details.....	78
6.1.1	Material and methods.....	78

6.1.2	Preparation of the gold nanoparticles-embedded gelatin.....	78
6.2	Results and discussion.....	79
6.2.1	Optical properties of gold-gelatin nanocomposite and the formation of trapped hydrogen bubbles.....	79
6.2.2	Morphological features of the gold- gelatin nanocomposite film with hydrogen bubbles inclusions.....	81
6.2.3	Stability mechanism of the bubbles.....	86
6.2.4	Formations of nanoindentations.....	88
6.2.5	Influence of the bubbles on the gold particles stability.....	91
6.2.6	Simulation of the optical properties of gold – gelatin nanocomposite films with hydrogen bubble inclusions using DDA.....	93
6.3	Conclusions.....	95
CHAPTER SEVEN.....		96

Conclusions

7.1	Modeling the optical properties of metallic nanoparticles.....	96
7.1.1	Spherical nanoparticles arranged in planar arrays.....	96
7.1.2	Single oriented nanoparticles of different shapes (multi-fold symmetry)	97
7.2	Effect of the host material on the optical properties of gold nanoparticles.....	98
7.2.1	Gold- Poly(methyl methacrylate) nanocomposite material.....	98
7.2.2	Gold-Gelatin nanocomposite material.....	99
7.3	Future perspectives.....	99

TABLE OF FIGURES

Figure 1: Schematic representation of the plasmon resonance. The electron cloud is shifted relative to the positive background due to the interaction with the incident radiation. The electronic collective oscillations are called plasmons.....	11
Figure 2: (a) SPR, the arrows indicate the electric field lines due the distribution of the polarization charge. (b) LSPR, the surface charges are locally oscillated around the metal nanoparticles. Figure is reproduced from reference 4.....	12
Figure 3: Contribution from free and bound electrons to the (a) real part and the (b) imaginary part of the bulk dielectric function, the calculated values are the summation of both contributions. The experimental dielectric function has been extracted from Johnson and Christy [98]. The figure is reproduced from reference 86.....	17
Figure 4: (a) Absorption spectrum corresponding to gold colloidal solution of different sizes, (b) linear variation of the peak position with the particle size. Figure is reproduced from reference 87.....	19
Figure 5: (a) Sensitivity of the LSPR to the refractive index of the surrounding medium for a gold spherical nanoparticle of size of 50 nm , black (in air),red (in water), green (in pentanol, $n=1.41$) and blue (in gelatine , $n=1.5$). (b) Band position of the LSPR mode is linearly red shifted with the refractive index of the host medium.....	21
Figure 6: Dependency of the excited type of LSPR mode on the orientation of the gold nanorod of aspect ratio of 3 (the black arrow indicates the direction of incident electric field (E)).....	22
Figure 7: Optical spectra for different gold nanoparticles morphologies. (a) Sphere of size of 20 nm, and a nanorod of length of 60 nm and width of 20 nm. (b) Effect of the sharper edges on the optical response of a single silver triangle; figure is reproduced from reference 107.....	23

Figure 8: The object is represented by a finite array of polarizable points which are setting on a square lattice of side d (the inter-dipole spacing). The target can be represented as well by a sphere of effective radius of equal volume as well.....28

Figure 9: Calculated absorption (black), scattering (red) and extinction (green) efficiencies of a single gold spherical particle of size of (a) 40 nm and (b) 140 nm.....34

Figure 10: Real (red solid lines) and imaginary (red dashed lines) components of the complex dielectric function of (a) gold and silver nanoparticles of 5 nm in diameter as compared to those of bulk materials (black lines). (c) Absorption spectra for a single spherical particle by using size-corrected (dashed line) and bulk (solid line) dielectric function. (d) calculated absorption efficiency for both gold (black line) and silver (red line) spherical particle of the same size (5 nm).....36

Figure 11: The geometry of 61-sphere hexagonal monolayer array of 5 nm nanoparticles, the interparticle separation is represented by both the border-border (D) and the center-to-center (CC) distances between two nearest-neighbour nanospheres.....38

Figure 12: Schematic representation of the target orientation in the external incident electric field (E). K indicates the direction of the propagation of the incident light39

Figure 13: absorption spectra of (a) gold and (b) silver ultrafine particle arranged in a close-packed hexagonal array of 61 spheres.....40

Figure 14: Absorption efficiency for the (a,b) gold and (b) silver nanoparticles in planar hexagonal arrays for different target's size.....42

Figure 15: Structural parameters of (a) a cube, (b) a nanobar, (c) orientation of the nanobar with respect to the incident radiation (p-polarized light).....44

Figure 16: (a) The geometrical parameters of the ellipsoidal nanoparticle, and the orientation of the particle in the lab frame around the x-axis with angle θ , (b) the rotation of the nanoellipsoid in the target frame around the a-axis with angle β44

Figure 17: (a) Dependency of the absorption spectrum on the nanocube width, (b) the maximum absorption efficiency as a function of the width, (c) Comparison between observed and calculated absorption spectra of a gold nanocube of width 45 nm embedded in water, (d) Absorption spectra of both gold (red) and silver (black) cubic nanoparticles of the same size embedded in air.....46

Figure 18: Absorption spectra for a gold nanobar (40 x 80 nm) at different incident angles and p-polarized light.....48

Figure 19: (a) Calculated absorption spectra of a nanobar of width of 40 nm and different aspect ratios at $\Theta=30^\circ$, (b) Position of the longitudinal band versus the nanobar length.....49

Figure 20: Normalized absorption spectra as a function of the incident wavelength for (a) gold and (b) silver ellipsoidal nanoparticle. In both cases, the principal axis of the particle is aligned parallel to the incident electric field. The corresponding structural parameters are $2a= 40$ nm, $2b=20$ nm and $2c= 10$ nm.....51

Figure 21: Dependency of the absorption efficiency on the rotation angle for (a) gold and (b) silver ellipsoidal nanoparticles. The corresponding structural parameters are $2a= 40$ nm, $2b=20$ nm and $2c= 10$ nm.....52

Figure 22: Dependency of the absorption efficiency on the incident angle at a constant rotation angle ($\beta=60^\circ$) for (a) gold and (b) silver ellipsoidal nanoparticles. The insets represent the spectra in selected wavelength ranges.....53

Figure 23: Normalized absorption spectra of a (a) gold and (b) silver ellipsoid of different a-axis length, (c) the band position of LM versus the length of the a-axis. (d) the band position of LM as a function of the nanoellipsoid effective radius. The b-axis and the c-axis are respectively 10 and 5 nm.....54

Figure 24: Absorption efficiency spectra of (a) gold and (b) silver ellipsoid at different b-axis lengths, (c) the band position of LM versus the length of the b-axis. The respective values for a-axis and c-axis are 50 and 10 nm.....55

Figure 25: Absorption coefficient of (a) gold and (b) silver ellipsoid at different c-axis lengths. The respective lengths of the a-axis and the b-axis are 50 and 40 nm.....56

Figure 26: UV-Vis absorption spectra of Au-PMMA nanocomposites corresponding to different (a) irradiation times (sample annealed for 30 min at 90°C) and (b) annealing temperature (time of irradiation is kept constant at 90 min).....63

Figure 27: SEM images of samples UV-irradiated for 90 min and annealed for 30 min at (a) 70°C and (b) 90°C.....64

Figure 28: SEM image of the MW-irradiated sample for 2 min.....65

Figure 29: UV-Vis spectra corresponding to the thermal-reduced samples (red: sample is heated after 30 min after the deposition, black: the sample is heated immediately).....67

Figure 30: Height-AFM image of the Au-PMMA film on a glass substrate (a) before annealing and (b) after annealing.(c) Normalized absorption Spectra of the Au-PMMA samples prepared by MW-irradiation before annealing (black curve) and after annealing at 300°C for 30 min (red curve).....68

Figure 31: Refractive index sensitivity of the Au-PMMA nanocomposite of non-annealed (■) and annealed (●) samples for (a) MW-irradiated sample, (b) thermally- reduced sample, (c) UV-irradiated samples.....70

Figure 32: Sensing experiment performed on the annealed sample. Red curve: LSPR gold band in the annealed nanocomposite, green curve: after immersion in ethanol solution of 1-octadecane thiol, black curve: after immersion in the antibody solution, and blue curve: after immersion in the antigen solution.....72

Figure 33: Comparison between the observed (black) and simulated optical properties (blue for the DDA-simulated curve and red corresponding to Mie’s theory) of Au-PMMA nanostructure. The curve corresponding to the experimental results corresponds to the MW-irradiated sample.73

Figure 34: (a) Suspension of the gold -gelatin nanocomposite with hydrogen bubbles. The inset shows the nanocomposite film on a glass substrate. (b) UV-Vis absorption spectrum of gold-gelatin nanocomposite, (black curve: measured in solution directly after synthesis, red curve: in solution, one month from the synthesis; green curve: solution, 2 months from the synthesis; blue curve: film on glass).....80

Figure 35: AFM image of gold–gelatin nanocomposite film on a glass substrate shows the embedded gold nanoparticles (white dots) in the gelatine matrix. The inset shows the bubbles trapped inside a gelatin patch.....82

Figure 36: AFM-height image (a) of well distrusted bubbles and the corresponding phase image (b). (c) Line scan profile across the bubble marked by a segment in figure a.....83

Figure 37: Schematic representation of a bubble formed on the gold -gelatin film.....84

Figure 38: Histogram of (a) bubbles height and (b) Width.....85

Figure 39: (A) 2D AFM topography image of nanoindent, (b) the corresponding 3D image...89

Figure 40: Schematic representation of a bubble formed on the gold-gelatin film.....89

Figure 41: 3D AFM-height image of stable nanoindent.....90

Figure 42: AFM images of the traces of nanobubbles (a) that left the surface of the film (dark holes in the 2D image) and the corresponding 3D image (b).(c) 1D scan profile across the hole marked by a segment in the height image.....91

Figure 43: 3D AFM-height image, the scan size is 10.2 and 6.2 micron for image a and b respectively. Gold nanoparticles appear sparks in the images92

Figure 44: DDA simulation of the optical properties of gold nanoparticles of size of 50 nm embedded in gelatin. The green curve shows the experimental band (520 nm) and the others

show the position of the bands by assuming different refractive indices to simulate the environment.....93

Figure 45: DDA simulation of the position of the Au-LSPR band (black curve) by assuming $n = 1$ (air); red curve: experimental spectrum (510 nm)94

CHAPTER ONE

Introduction

Due to the interaction of the incident electromagnetic radiation with metallic structures at the nanometric-scale, an electronic oscillatory motion is induced. If the frequency of the incident radiation matches the electronic oscillation frequency, a resonance occurs. Depending on the dimensions of the resonator material, resonance fluctuations are categorized into two types, namely, Surface Plasmon Resonance (SPR) [1-3] and Localized Surface Plasmon Resonance (LSPR) [4-6]. LSPR is confined electronic oscillations that occur locally around a finite volume of metallic structures, while the SPR occurs on the surface of metallic thin films of infinite extent.

The importance of the metallic nanostructures originates from their ability to absorb and scatter the incident light in both the visible and the infrared regions [7-8]. The tuning of their optical response depends on their morphology [9-12], size [10-12], type of the metal [10-11,13] and the surrounding medium [13]. Controlling the nanostructure morphology results in changing the way the light can be polarized. The separation of the opposite charges along the polarization axis is considered a unique way to control the characteristics (band position, band width and intensity) of Plasmonic Mode (PM) [14], while the orientation of the nanoparticles in the incident electric field controls the type of the excited PM [15-19].

Although these most interesting properties have been the subject of many studies, there are still areas that are not well understood and explored. This thesis aims at contributing in the theoretical modeling of some types of nanoparticles using the Discrete Dipole Approximation (DDA) method [20-22] and the experimental studies of novel polymer composite structures that incorporate the plasmonic nanoparticles.

1.1 Background and thesis overview

1.1.1 Modeling of the absorption spectrum of metallic spherical nanoparticles arranged in planar hexagonal arrays

Tailoring the optical properties of the metallic nanostructures of different sizes and shapes is a desired aim for technological applications. The application of the metallic nanostructures requires the deposition of a close-packed assembly of particles of different shapes, sizes and configurations. Therefore, understanding the optical response of an isolated oriented individual particle is the main key for tuning the optical properties of large clusters. Simulation of the optical response of the metallic nanoparticles is considered as the first step to achieve this goal. Many computational tools have emerged to model the optical properties of metallic nanostructures [23-25]. Based on the analytical solution of Maxwell's equations, the DDA method is one of the well-known and reliable computational tools for simulating the optical properties of nanostructures. It can be used for an isolated particle and for assemblies of particles of different sizes and shapes embedded in a complex dielectric medium. DDA has also been used to study the plasmon-coupling effect on the optical response of interacting metallic nanoparticles, arranged in various dimensional arrays [17, 26].

Due to the high symmetry order of spherical nanoparticles, their optical response exhibits only a single dipolar PM (isotropic optical behaviour) [27-28]. The anisotropic optical response of the spherical nanoparticles is observed as they are brought in contact with other particles. The optical response of metallic clusters can be controlled by the metal type [29-31], interparticle distance [26, 31], polarization state of the incident radiation [29-30] and the relative orientation in the incident field [29-31].

The absorption spectra of both gold and silver ultrafine particles (size = 5 nm) arranged in a 2D hexagonal array have been studied theoretically by using DDA [26, 31]. The target consisted of 81 identical spherical particles. The effect of the interparticle spacing on the plasmonic coupling between the interacting particles has been investigated [26, 31]. The simulation results showed that the anisotropic/isotropic optical aspects can be controlled by the ratio of particles spacing to the size of the target unit cell (single spherical particle). Another

theoretical study by using the DDA method revealed that the optical response of those metallic nanoparticles can be dramatically changed when the nanoparticles are arranged in a 3D hexagonal configuration [30]. The size of the array was controlled by the number of hexagonal layers used to generate the 3D target. Each layer consisted of a constant number of interacting spherical particles (61 particles). The result of simulations showed that the anisotropic optical response of metallic target composed of one layer turned to be an isotropic when the target is composed of many layers. In the previously motioned studies, the nanoparticles were arranged in either a 2D array of monolayer or a 3D array of many layers, in both cases, the number of nanoparticles was fixed in each layer. The anisotropic/isotropic optical properties of the metallic nanoparticles arranged in an array of monolayer can be effectively tuned by the changing the planar extension of the array. As well, the planar extension of the array is of great importance for many fields because of the possibility of miniaturization of devices for different applications.

The current work aims at demonstrating the effect of the target size on the optical properties of the ultrafine gold and silver nanoparticles arranged in both 2D hexagonal configurations of different sizes. DDA is employed to model the absorption spectra of the target under consideration. We adopted the hexagonal configuration to construct our target as this configuration is sufficiently general and close to common experimental situations. The size of the target under investigation is controlled by the number of the interacting particles. The smallest hexagonal target consisting of 7 spherical particles, and then the target size is augmented gradually to 127 particles.

1.1.2 Modeling of the absorption spectrum of metallic nanoparticles with many symmetry axes

Changing the morphology of the spherical nanoparticle resulted in changing the symmetry order, which has a dramatic effect on the distribution of the polarization charges over the surface area of the nanostructures. The redistribution of these charges results in tuning the frequency and the type of the excited PM, namely, the Transverse Mode (TM), the Longitudinal Mode (LM), and the high-order multipole resonance modes [32-34]. Updated nanofabrication

techniques are indeed able to produce well-defined nanoparticles of different shapes such as nanocubes [35], nanobars [36] and nanoellipsoids [37]. These nanoparticles are synthesized in different size distributions and even an ordered 2D array of different configurations [37-38]. Metallic particles of different morphologies have attracted a considerable attention because of many fundamental and practical considerations. First, the synthesis of controlled-shape particles has motivated experimental works for understanding both the shape-dependent optical properties and the growth mechanism of the metallic nanocrystals. Second, their distinguished optical features make them strong candidates for desirable applications in bio-labs [39-40], photovoltaic industry [41-42] and Surface Enhanced Raman Scattering (SERS) [43-44].

Many-fold symmetry nanoparticles (e.g rod-like shapes, ellipsoidal, triangular, cubic,...etc) exhibit most interesting selective absorption features in the visible and near infrared ranges. Their morphologies exhibit different polarization factors along each symmetry axis. This results in a change of the electrostatic interaction between the polarization charges and hence different plasmonic frequencies. The plain cylinder and hemi-spherical capped cylinder are used to approximate the nanorod shape. These morphologies have a uniform circular cross-sectional area which ensures the uniform distribution of the polarization charges over the particle surface area. The rod-like shapes have been extensively studied theoretically and experimentally. Two major results were found, first, the possibility to excite both LM and TM simultaneously [45-47]. Second, the band position of the LM is linearly red shifted with the nanorod length, while the change in the resonance wavelength of the TM is less pronounced with the nanorod size [45-47].

Among other interesting rod-like shapes, there are nanobars and nanoellipsoids. Both shapes have a non uniform cross-section of distinct symmetry axes compared to the circular cross-section of the nanorods (plain cylinder and hemi-spherical capped cylinder). The nanocubes are considered as preliminary seeds for the synthesis of the nanobar by stretching the former along one of its axes. In the same way, the nanoellipsoidal particles are generated by stretching, either a spheroidal plate-like particle vertically or a spherical particle along two orthogonal directions with different stretching lengths. The variety of cross-sectional areas of both nanobar and nanoellipsoid particles may introduce a unique way to tune their optical aspects in both the visible and UV spectral regions. The spatial distribution of the surface induced dipole

moments on a non uniform surface (nanoparticles of different symmetry axes) results in altering the coulombic restoring force between the polarization charges. This, in turn, yields to a change in the characteristics of the TM and it could even result in its splitting into several bands. Indeed, in a remarkable experiment, Kalkbrenner et al. [48] succeeded in rotating a single gold ellipsoidal nanoparticle attached to the tip of a glass fibre mounted on a stage of a Scanning Near-field Optical Microscope (SNOM). Due to the three-fold symmetry of the gold ellipsoidal particle, three PMs were observed individually at a distinct combination of the polarization angle and the rotation angle of the tip in the incident light. The size and orientation of these particles in the incident electric field under certain type of light polarization is the key for observing different PMs.

The effect of the orientation of nanorod/nanoellipsoid particles in both the lab and the target frames on the excitation of the desired PM has not yet been investigated in detail. To better evaluate the optical behaviour of these particles of this specific and quite interesting shapes, the current work aims at studying in a comprehensive way, the optical properties of an oriented isolated nanorod/nanoellipsoidal particle both for the cases of gold and silver. It would thus be of great interest to find whether there exist combinations of the rotation and orientation angles that would allow the simultaneous excitation of all PMs. To this end, the effect of different parameters on the optical response of gold and silver nanoparticles is discussed. The parameters include the orientation of the target in both the lab and the target frames and the sensitivity of the band position of the PM to the length distribution of each principal axis. To achieve this goal, the DDA is employed to calculate the absorption efficiency for both types of nanoparticles.

1.1.3 Effect of the physical host material on the optical properties of gold-polymer nanocomposite materials

The influence of the refractive index of an embedding material on the resonance wavelength of the metal-LSPR can be very important. Thus for the experimental part, we will study in detail the effect of the physical environment on the optical properties of metallic nanoparticles.

In colloid science, metal particles are usually prepared in a mixture of solvents and other chemicals (e.g. reducing and stabilizing agents). The relative concentrations and diversity of the chemical structures of the reactants may lead to a non homogenous surrounding. Because of their small size (high surface energy), the particles tend to aggregate and form large clusters. To prevent the aggregation/agglomeration processes, metallic suspensions are prepared in the presence of a polymer matrix to form hybrid materials known as metal–polymer nanocomposites. Incorporating metallic nanoparticles in non-absorbing materials provides important information on the host medium-dependent chemical and physical properties of the metallic nanostructures [49-61]. The generated novel functions lead to a wide range of interesting applications [51-53].

There are two types of polymers used to prepare nanocomposite materials, synthetic and biomaterial-based polymers. Basically, the polymer is used as a stabilizing/capping agent to prevent the natural aggregation process of the metallic nanoparticles and, in some cases, can be used as a reducing agent as well [54-55]. One of the most interesting synthetic polymers is Poly(methyl methacrylate) PMMA. Because of its high transparency, thermoplasticity and a relatively low glass-transition temperature, it is suitable for lower post-synthesis heat treatments [56].

In general, to prepare gold nanocomposite films, the samples are prepared in a common polar solvent for both the polymer and the gold precursor and then the gold salt is reduced in the presence of the polymer by using photochemical methods (Microwave- ,UV-irradiation and thermal-methods). Both the UV- and thermal-methods have been used to prepare gold nanocomposite films by using acetone as a solvent, while, microwave-assisted reactions have been carried out and studied only in solutions by using water because of its high dipole moment and high value of dielectric loss [62-63]. In the current work, MW-assisted synthesis of Au-PMMA material is carried out by using the acetone as a solvent. The optical properties of the nanocomposites are compared to that of nanocomposites prepared by the other photochemical methods.

The adopted reduction processes affect the shape, size and surface distributions of the gold nanoparticles and hence their sensing capabilities of the surrounding materials. The strong interactions between the chain segments of the polymer and nanoparticles contribute to the improvement the mechanical properties of the film but, at the same time, they may decrease the mobility of the particles and interfere with the interaction with the surrounding medium. Therefore, it is important to introduce a method to increase the population of the surface particles and therefore, enhance the sensing capability of the metallic nanocomposite materials. In the current work, we also explore several promising ways to increase the mobility of gold nanoparticles in order to increase their surface particle density and thus, make them accessible to the surrounding environment.

More recently, a new class of composites, called bio-nanocomposites (BNC), has emerged. In this case, natural polymers such as chitosan, gelatin, polysaccharides and starch, are used as a host material for the metallic nanoparticles [64-66]. Among the advantageous properties of natural polymers are biocompatibility, biodegradability and non-toxicity for the environment. The interest in the gelatin as an embedding material is based on the low cost, stability, the ability of cross-linking and the possibility for the material to be modified chemically. It has been used for a long time in food processing, pharmaceutical industry, medical applications and preparation of colloidal drug delivery systems based on nanoparticles.

Gelatin-BNCs with gold nanoparticles were prepared by using gelatin, sodium citrate and ascorbic acid as reducing/stabilizing agents. One of the versatile inorganic reducing agent used in preparation of the metallic suspension is sodium borohydride (NaBH_4). To the best of our knowledge, no experimental work has been reported on the preparation of gold-Gelatin-BNCs using sodium borohydride as a reducing agent. Sodium borohydride is considered as a source of hydrogen gas (H_2) when it dissolves in water. It is expected that the presence of the H_2 gas in the surrounding medium of the gold particles would change the effective refractive index of the medium and hence, the characteristics of the Au-LSPR. The hydrogen gas in the form of nanobubbles has been used as templates to form hollow gold nanoparticles [67] and core-shell nanoparticles [68].

It is therefore of great interest to investigate the effect of the NaBH_4 concentration (the H_2 gas concentration) on the optical properties and the stability of the gold particles. We attempt to develop structures where the gold nanoparticles are directly associated with hydrogen gas domains. The interfacial bubbles which are very close to the film surface are expected to be unstable and to explode during the drying process. The cavities left behind the exploded bubbles can be used to trap the metallic particles and hence increase their stability.

1.2 Structure of the thesis

A brief description of each chapter is given below

Chapter 2 demonstrates the physical origin of the electronic oscillations over a finite volume of the metallic structure at the nanometric scale. Depending on the surface spatial distribution of the polarization charges, the classification of the electronic oscillations into SPR and LSPR is presented. The validity of the adopted free-electron model to mathematically describe the origin of the plasmon resonance is addressed in terms of both the interband and intraband transitions. In the subsequent sections, the tunability of the nanoparticles optical response through the size, morphology, relative particle orientation in the incident light, dielectric function of both the metal particles and the surrounding material is discussed in detail.

The DDA method, as a computational tool to calculate the optical aspects of metallic nanostructures is presented in chapter 3. The mathematical formulations of the electromagnetic scattering problem are defined in terms of the particle polarizability, the local field and number of the polarizable points needed to describe the target geometry. The validity and limitations of DDA are discussed. The outputs of the DDA method are briefly discussed in the subsequent subsection.

In chapter 4, the absorption spectra of both single gold and silver spherical particles are calculated and compared to that of spherical particles arranged 2D planar array of a hexagonal configuration. The effect of the array size (the number of the interacting particles) on particles optical properties is investigated as well. This chapter also sheds light on the possibility of the simultaneous excitation of different plasmonic bands (LM and TM), by a unique combination of

Euler angles. In multi-fold symmetry particle configuration, this is achieved by controlling the particle size, shape and the orientation angle in both the lab and the target frames.

The influence of the embedding material (PMMA) on the optical properties of gold particles is discussed in chapter 5. The gold salt is photochemically reduced in the presence of the polymer matrix to form gold-nanocomposite films. The reduction process of the gold ions that occurs *via* three different methods: UV-irradiation, thermal-reduction, and MW-irradiation is described. The effect of the heat treatment on the particles' surface populations and, hence, their sensitivity toward the dielectric medium is investigated for samples synthesized by the three different methods. The sensitivity of the nanocomposite film to the host medium will be tested by monitoring the change in the band position gold-LSPR per unit refractive index. The sensitivity capability of both annealed and non-annealed samples will be compared.

The study of the optical and the morphological properties of gold–gelatin nanocomposite film prepared by using sodium borohydride as a reducing agent of the gold salt is the main scope of chapter 6. The reaction between the gold salt and the reducing agent results in gold nanoparticles and the formation of hydrogen domains of different spatial distributions. The surface features of the stable/unstable hydrogen bubbles and the formation of the gas nanoindentations are discussed in terms of the surface tension and the Laplace pressure. The effect of hydrogen gas on the absorption spectrum of gold nanoparticles is studied and then compared to that calculated by DDA for different gold/ borohydride molar ratios.

The conclusions of the main theoretical and experimental findings of the current work are summarized, along with the most interesting observations in chapter 7.

CHAPTER TWO

Localized surface plasmonic resonance of metallic nanoparticles

In the introduction, a basic knowledge of plasmon resonance phenomenon is introduced. The main features of the thesis, the novelty of the current work and how it relates to the previously published studies in the same domain have also been presented. In the present chapter, more details about Localized Surface Plasmon Resonance (LSPR) modes are introduced and then compared to the Surface Plasmon Resonance (SPR). The validity of the adopted theoretical model (free electron model) to describe mathematically the resonance phenomenon is addressed in detail. The tunability of the optical properties of metallic nanoparticles is also discussed in terms of several parameters (size, shape, host material, plasmonic coupling effect ...etc). This chapter aims at setting the theoretical foundation of the optical properties of the metallic nanoparticles by describing both the interband and intraband electronic transitions, starting with Clausius-Mossotti relation and the derivation of the dielectric function in the free electron gas model.

2.1 Nanoscale materials *versus* bulk materials

The transition metallic particles at the nano-metric scale have attracted considerable attention due to the unique electrical, optical, chemical and magnetic properties as compared to their bulk counterparts [69-70]. Noble-metal nanoparticles of a size smaller than the wavelength of the incident radiation can effectively scatter and selectively absorb light at a certain wavelength in the visible and near-infrared regions. The fascinating optical properties of the metallic nanostructures originate from the coupling between the electronic plasma and the incident light which results in an electronic oscillatory motion at the interface of metal/dielectric surface.

The nanoparticles are considered as a connecting bridge between the material of large scale (bulk) and the atomic structure. The optical, chemical and physical properties of bulk

material are invariant with the size, while those properties in nanometric scale show significant size dependency. The term of nanoparticle includes normally a cluster of hundreds of thousands of atoms of a total size that doesn't exceed 100 nm [70]. One of the interesting features of the reduced size particles is that the optical transition is shifted to the visible region as compared to the transitions in the near infrared region in the case of the bulk materials [69-71]. This distinctive behavior of smaller particles originates from the high surface atoms density relative to the interior atoms. In the finite extent system, the energy level density is high and the energy difference between the electronic states increases as the size of the particle decreases [72-73].

2.2 Basic idea of the plasmonic resonance

The atoms consist of a positive core surrounded by an electron cloud. Due to the interaction of the atoms with the incident radiation, the electrons in the conduction band are shifted as a result of the force exerted by the external electric field. As the opposite charges are separated, the electric dipoles are induced as shown in Figure 1. The columbic interaction between the electrons and the protons acts as a restoring force which leads to electronic oscillations. These electronic collective oscillations are called plasmons [1-6.74].

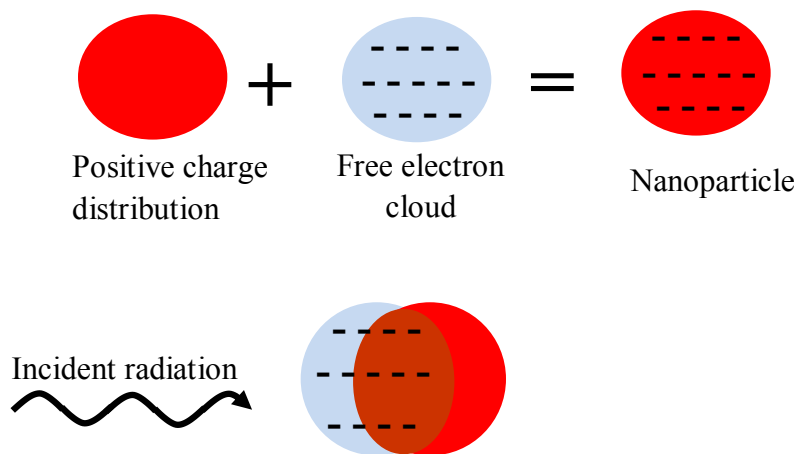


Figure 1: Schematic representation of the plasmon resonance. The electron cloud is shifted relative to the positive background due to the interaction with the incident radiation. The electronic collective oscillations are called plasmons.

2.3 Types of electron resonance

The electronic fluctuations are classified into SPR [1-3] and LSPR [4-6] according to the spatial distribution of the negative charges. In the former case, the alternating negative/positive charges along the metal surface generate a propagating electronic density wave in a direction parallel to the metal/dielectric interface as illustrated in Figure 2.a. The propagating length depends on the dielectric function of the metal and the wavelength of the exciting radiation [75]. The free-space light source is unable to excite the SPR, because of the mismatch in the momentum between the incident light and the SPR [76-77]. The excitation of the SPR requires an additional momentum which can be achieved by, either using the idea of the total internal reflection [78], or periodic corrugations in the metallic surface [79-80]. The frequency of the SPR is lower than the one for the bulk material when the air-metal interface is considered [81].

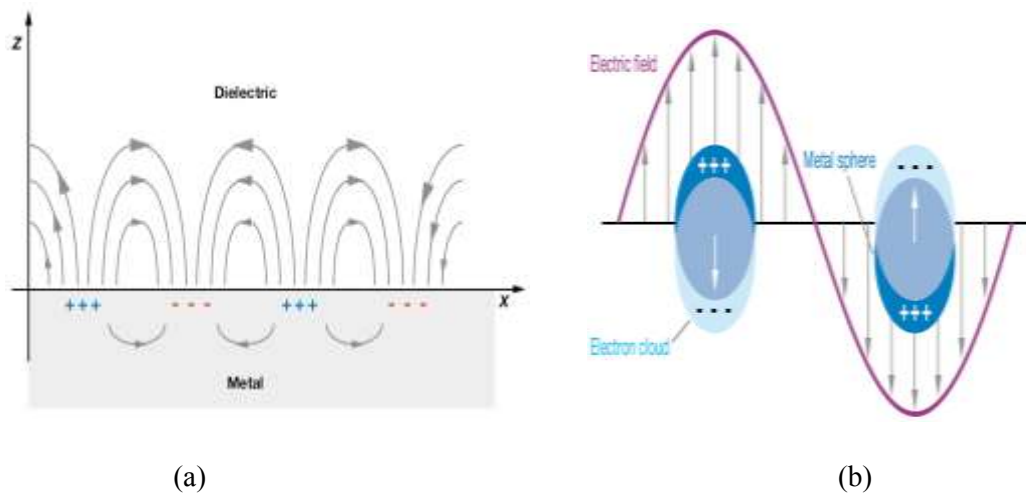


Figure 2: (a) SPR, the arrows indicate the electric field lines due the distribution of the polarization charge. (b) LSPR, the surface charges are locally oscillated around the metal nanoparticles. Figure is reproduced from reference 4.

If the electronic fluctuations occur locally around the nanoparticle as shown in Figure 2.b., the corresponding surface oscillation is called LSPR. In LSPR, the induced dipoles change their direction in the external field every half period, which forms a non-propagating oscillations mode. The confined electronic oscillations in the LSPR enhance the local field distribution at the surface of the nanostructures. That makes them a strong candidate in several potential technical applications such as the Surface-Enhanced Raman Scattering (SERS) [43-44], nanoantennas [82], optical waveguides [83-84], solar energy conversion technologies [41-42] and bio-sensing [39-40].

2.4 LSPR modes of sub-wavelength noble metallic nanoparticles

Metallic nanoparticles suspended in water-based dispersion mediums are known as colloidal solutions. Faraday [85] was the first who studied the optical properties of the gold suspensions. The gold nanoparticles have been synthesized by reducing a gold salt (gold chloride) by phosphorus. No advanced means were available to identify the morphology of the gold nanoparticles or to measure their size distributions. Early, in the nineteenth century, Mie explained the origin of the gold colloids' red color. He studied the effect of the size and the dielectric function of the host medium on the optical response of a single spherical nanoparticle. Mie's theory [86] provides the exact solution of the Maxwell's equations for the light interaction with an isotropic spherical nanoparticle surrounded by a non-absorbing homogenous medium. Knowing the great effect of the structural parameters of the metallic nanoparticles on their optical response, the researchers have tried to develop both theoretical and experimental techniques for better understanding their plasmonic characteristics.

The quasi-static approximation [87-88] is the lowest-order approach to describe the interaction between the light and particles with a size smaller than the incident wavelength. In this approximation, the spatial field variation is considered constant over the particle surface, so the interaction problem can be approximated as a particle in an electrostatic field. In the frame of the quasi-static approximation, the Clausius-Mossotti relation is used to describe the molecular polarizability (α) of the metallic nanoparticles of spherical shape

$$\alpha = 3V \varepsilon_0 \left(\frac{\varepsilon - \varepsilon_m}{\varepsilon + 2\varepsilon_m} \right) \quad 1$$

Where V is volume of the spherical particle and ε_0 , ε , ε_m are the dielectric functions of vacuum, metal and medium, respectively. In the real metal, the imaginary part (ε_i) of the dielectric function is varying slowly with the frequency, so the real part (ε_r) is mainly contributed to the dielectric function ($\varepsilon \approx \varepsilon_r$) [89]. The value of ε_r determines the resonance frequency of the LSPR while ε_i indicates the amount of the light being absorbed in the medium [89]. The resonance occurs when the polarizability is maximum which can be deduced from the last equation to be

$$\varepsilon_r + 2\varepsilon_m = 0 \quad 2$$

For the condition to be fulfilled, ε_r should be negative; this is satisfied by metals [90-91]. The absorption (C_{abs}) and scattering (C_{sca}) cross-sections [88] are given in terms of the dipolar polarizability

$$C_{abs} = k \text{Im}(\alpha) = 4\pi k a^2 \text{Im} \left[\frac{\varepsilon_1 - \varepsilon_m}{\varepsilon_1 + 2\varepsilon_m} \right] \quad 3$$

$$C_{sca} : \frac{k^4}{6\pi} |\alpha|^2 = \frac{8\pi}{3} k^4 a^6 \left[\frac{\varepsilon - \varepsilon_m}{\varepsilon + 2\varepsilon_m} \right]^2$$

Where Im refers to the imaginary component and k is the wave vector propagating in the metal which relates to the wave vector (k_0) in the free space by $k = k_0 \varepsilon_m^{1/2}$.

For sub-wavelength fine metallic nanoparticles, the extinction (= absorption + scattering) cross-section is mainly dominated by the absorption cross-section [46, 92].

2.5 Free electron gas model: Drude's theory

In the general case of the real bulk metals, the dielectric function consists of two contributions accounting for the interband and intraband electron transitions. That involves the

bound and the free electrons, respectively [91, 93]. The contribution of the intraband transition can be described by using the Drude free electron model [91, 94]. The equation of the motion of free electrons of an effective mass (m) and charge (e) in a sinusoidal electric field ($E(t)$) of angular frequency (ω), can be expressed as

$$m \frac{\partial^2 x}{\partial t^2} + m\gamma_0 \frac{dx}{dt} + kx = eE(t) = E_0 e^{-i\omega t} \quad 4$$

The second term describes the damping force that arises from the collisions between the electrons where γ_0 is the damping constant. The third force term indicates the spring-like restoring force which arises from the shift of the negative charges relative to the positive nuclei (induced dipole moments). In the case of the good conductors (free electron gas), the spring constant yields to zero. The solution of the previous second order differential equation is given by

$$x = \frac{eE_0 e^{-i\omega t}}{m(i\omega\gamma_0 + \omega^2)} \quad 5$$

Considering that N is the polarization charges per unit volume (free electron density), the polarization per unit volume (P) is

$$P = Nex = N \frac{e^2 E_0 e^{-i\omega t}}{m(i\omega\gamma_0 + \omega^2)} \quad 6$$

It's straightforward to derive ϵ for the metallic particles as a function of the incident angular frequency [90, 95], ϵ is given by

$$\epsilon = \epsilon_r + i\epsilon_i = 1 - \frac{\omega_p^2}{\omega^2 + i\gamma_0\omega} \quad 7$$

Where ω_p ($=\sqrt{\frac{4\pi Ne^2}{m}}$) is the plasma angular frequency of the bulk metal. It is clear that the plasma frequency depends only on the free electrons density of the metal and it is independent on

the particle size. Table 1 summarizes the electronic density of three selected noble metals and their corresponding plasma frequencies. The plasma frequency of both gold and silver is comparable while the one for the copper is higher.

Element	N ($10^{22}/\text{cm}^3$)	w_p (10^{16} Hz)
Gold	5.90 [96]	1.40 [96]
Silver	5.86 [96]	1.39 [96]
Copper	8.47 [96]	1.64 [96]

Table 1: Electronic density and the plasma frequency of gold, silver and copper.

From equation 7, the real and the imaginary parts can be written as

$$\varepsilon_r = 1 - \frac{w_p^2}{w^2 + \gamma_0^2}, \quad \varepsilon_m = \frac{w_p^2 \gamma_0}{w(w^2 + \gamma_0^2)} \quad 8$$

In the high frequency regime ($w_p^2 \ll w^2$), ε_r and ε_i can be approximated, as follows

$$\varepsilon_r = 1 - \frac{w_p^2}{w^2}, \quad \varepsilon_m = \frac{w_p^2 \gamma_0}{w^3} \quad 9$$

In terms of the w_p , the resonance condition becomes $1 - \frac{w_p^2}{w^2} + 2\varepsilon_m = 0$, which gives

$w_{LSPR} = \frac{w_p}{\sqrt{2\varepsilon_m + 1}}$, where w_{LSPR} is the angular frequency of the LSPR. In the case of air as the

embedding material $w_{LSPR} = w_p/(3)^{1/2}$.

The dependency of the spectral features of the metallic nanoparticles on the structural parameters is not shown in the last equation. In spite of comparable plasma frequencies of both the gold and the silver, the corresponding LSPR frequency of a spherical nanoparticle of a size of around 50 nm occurs at 530 nm and 420 nm for gold and silver respectively [94,97]. Such deviation originates from the additional contribution to the dielectric function from the interband electronic transitions. The effect of the bound electrons on the LSPR frequency is not considered in the free gas model and, therefore, that model can't be applied to calculate the resonance

wavelength of the metallic nanoparticles except at low frequency regimes. To account for that contribution, an additional term should be added to include the electronic transition from d level to the dielectric permittivity. The ϵ described in equation 9 becomes [91]

$$\epsilon = 1 - \frac{w_p}{w^2 + i\gamma_0 w} + \chi_b \quad (10)$$

Where $\chi_b (= \chi_{1b} + i\chi_{2b})$ is the complex interband susceptibility, the w_{LSPR} becomes [91]

$$w_{LSPR} = \frac{w_p}{\sqrt{2\epsilon_m + \chi_b + 1}} \quad (11)$$

The sensitivity (S) of the band position of the Plasmonic Mode (PM) to the dielectric function of the host medium is given by

$$S = \frac{d\lambda_{LSPR}}{d\epsilon_m} = \frac{\lambda_p}{\sqrt{2\epsilon_m + \chi_b + 1}} \quad (12)$$

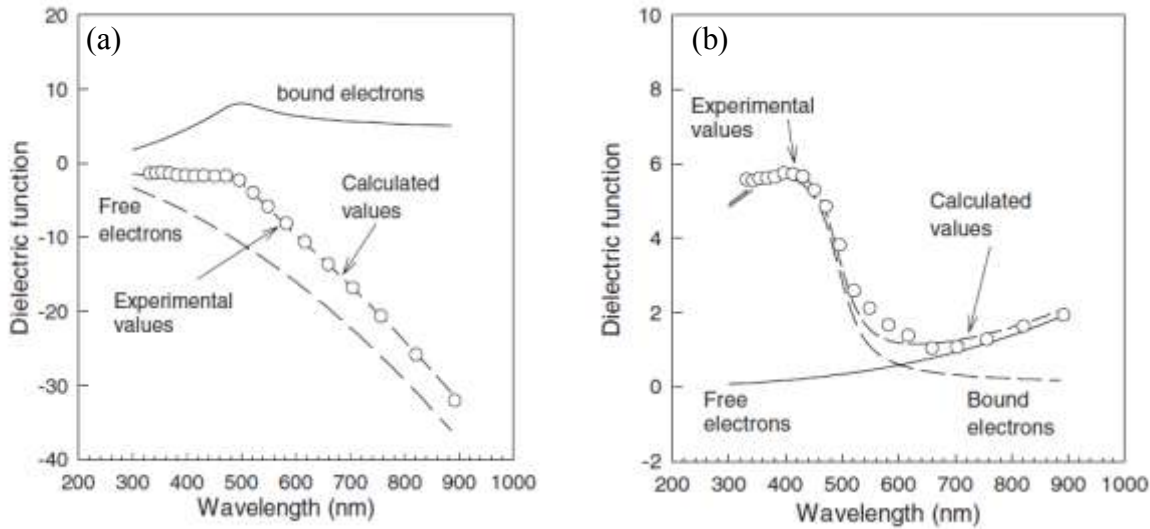


Figure 3: Contribution from free and bound electrons to the (a) real part and the (b) imaginary part of the gold bulk dielectric function, the calculated values are the summation of both contributions. The experimental dielectric function has been extracted from Johnson and Christy [98]. The figure is reproduced from reference 93.

because $\chi_{b\text{-Au}} > \chi_{b\text{-Ag}}$, silver is more sensitive to the physical surrounding environment than gold. Figure 3 compares the contribution from the free and bound electrons to both the real and the imaginary parts of the dielectric function. The calculated values are compared to the experimental ones.

In the framework of the free electron model, the band width (Γ) of the plasmonic band is equal to γ_0 [91]. To obtain the correct expression for Γ in a real metal, the effect of the bound electronic transitions should be taken into consideration. The value of Γ for the noble metal is given by [91]

$$\Gamma = \gamma_0 \sqrt{1 + \frac{2\chi_2 w_p}{(1 + \chi_1 + 2\varepsilon_m)\sqrt{1 + 2\varepsilon_m}}} \quad 13$$

2.6 Tunability of the LSPR properties

The unique optical properties of the metallic nanoparticles depend strongly on the structural parameters (size and shape), type of the metal and the dielectric function of the surrounding material where they are embedded. Other parameters that have a dramatic effect on their optical response are the coupling between the plasmonic resonances in nearby structures, the orientation of the particles relative to the incident radiation and the polarization state of the incident light. By tuning these variables, the optical properties of LSPR modes can be varied over the entire UV-Visible spectral regions. All these factors are addressed in detail in the subsequent subsections.

2.6.1 Dependence on the nanostructure size

2.6.1.1 Size effect on the plasmon oscillations

The use of the metallic nanostructure in the technical applications requires shape- and size-controlled synthesis techniques. The resonance frequency is a strong function of the particle

size such that the latter controls the spatial distribution of the polarization charges over the surface and the negative/positive charges separation as well. In the quasi-static approximation, the observed LSPR modes are attributed to the excitation of the dipolar resonance modes. As the size increases, the resonance wavelength the observed plasmon band increases due to the decrease in the restoring force between the opposite charges [94, 99-101]. Multipolar LSPR come into play as the nanoparticle size increases and the absorption spectra originate from the contribution of both dipolar and multipolar modes [88,101]. The general resonance condition [88] of these modes is given by

$$\frac{\epsilon_r}{\epsilon_m} = -\left[\frac{l+1}{l}\right] \quad 14$$

Where l is the order of the resonance mode and it takes the values $1,2,\dots,l$. The lowest order refers to the dipole excitation while the second order refers to the quadruple contribution and so on. The multipolar oscillations occur at higher energy compared with the dipolar one [88, 101]. The contribution of the higher order modes to the plasmon resonance affects its coherence phase due to the inhomogeneous charges distribution which results in broadening of the plasmon band [88, 94,101].

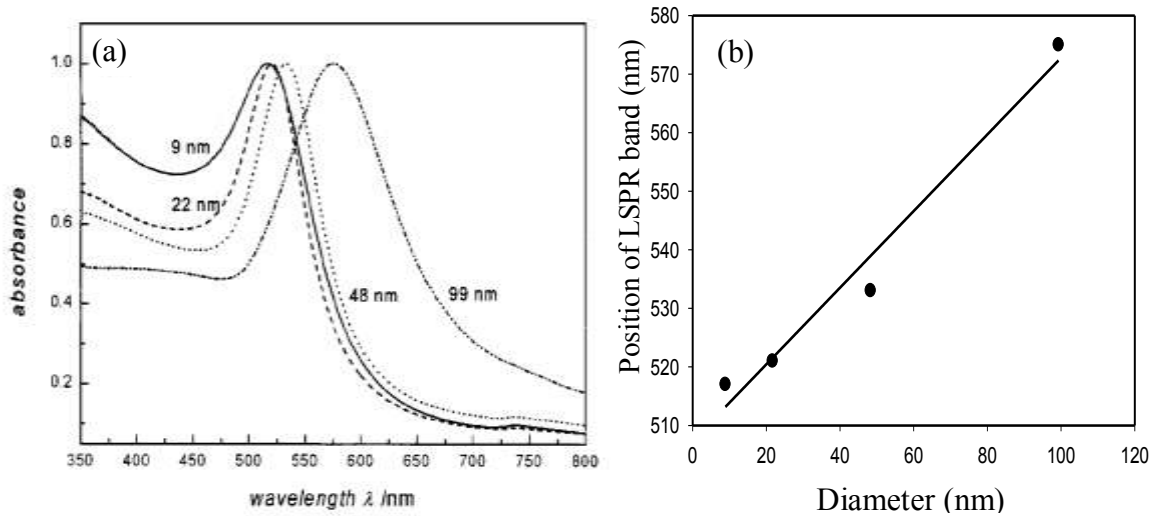


Figure 4: (a) Absorption spectrum corresponding to gold colloidal solution of different sizes, (b) linear variation of the peak position with the particle size. Figure is reproduced from reference 94.

Surface roughness, shape distortion and the scattering process effectively contribute to the plasmonic band broadening [102]. Due to radiation reemission of the larger particles, the extinction cross section has mainly contributions from the scattering properties [71]. The change in the phase between the incident and the scattered radiation (phase retardation effect) due to the depolarization of the driven charges across the nanoparticle results in an additional red shift of the dipolar resonance band [94]. Figure 4.a shows the UV-Visible absorption spectra of gold colloidal solution of different particle sizes [94]. It is clear that the band position of the gold-LSPR mode is linearly red shifted with the particle diameter as shown in Figure 4.b.

2.6.1.2 Size-corrected dielectric function

In the classical theory of the free electron gas, the γ_0 (the damping constant) is given by the reciprocal of the relaxation time (τ_0)

$$\gamma_0 = \frac{1}{\tau_0} = \frac{1}{\tau_{e-e}} + \frac{1}{\tau_{e-ph}} + \frac{1}{\tau_{e-d}} \quad 15$$

which counts for the electron-electron (τ_{e-e}), electron-phonon (τ_{e-ph}) and electron-defect (τ_{e-d}) relaxation times [94, 103]. The conduction electrons in the nanometer-sized metallic particles encounter an additional scattering process because their size becomes less or comparable to their mean-free-path (the intrinsic size effect) [94,103-105]. The scattering process results in a reduced mean-free-path according to $(\tau)^{-1} = (\tau_0)^{-1} + (\tau_s)^{-1}$, where (τ_s) is the relaxation time of the additional damping term. The latter relaxation time is given by $g v_f / a$ where v_f , a and g are the Fermi velocity, the particle effective radius and dimensionless parameter, respectively. The g -value is about unity [103]. According to the previous discussion, the dielectric function of the bulk metal should be modified to take into account the damping terms. The size-corrected dielectric function for the nanoparticle (ϵ_n) is expressed as follows

$$\epsilon_n(\omega) - \epsilon_{bulk}(\omega) = \frac{\omega_p^2}{\omega(\omega + i(1/\tau_0))} - \frac{\omega_p^2}{\omega(\omega + i(1/\tau))} \quad 16$$

2.6.2 Dependence on the dielectric function of the host material

The LSPR mode maxima of the metallic nanostructure are sensitive to the nature of the surrounding material. The adsorbances of the chemical molecules (chemical ligands) on the nanoparticle surface alter the surface charges distribution of the nanoparticles and hence their optical properties [106-107]. On the other hand, the deposition of the colloidal solutions on the solid substrate perturbs the electron density and redistributes the surface charge over both the nanoparticle and the supporting substrate. The nanoparticles-substrate electric field is no longer homogenous which results in excitation of higher order PMs [108-109].

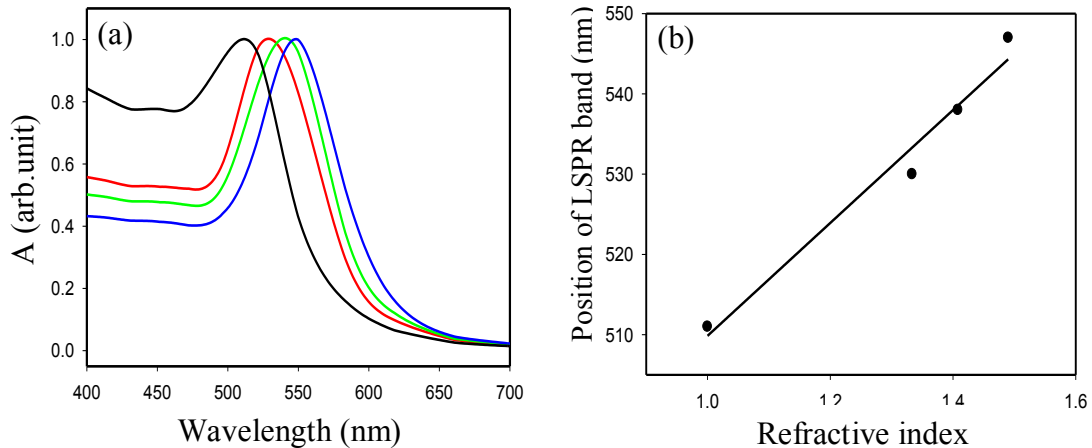


Figure 5 : (a) Sensitivity of the LSPR to the refractive index of the surrounding medium for a gold spherical nanoparticle of size of 50 nm , black (in air),red (in water), green (in pentanol, $n=1.41$) and blue (in gelatine , $n=1.5$). (b) Band position of the LSPR mode is linearly red shifted with the refractive index of the host medium.

The band position of the PM is red shifted linearly in a dense medium as compared to the one in the vacuum. Increasing the value of the dielectric function of the surrounding adjusts the resonance condition, results in lowering the restoring force (the columbic interaction) and hence the resonance occurs at lower frequency [107, 110]. Figure 5 shows the effect of the surrounding environment on the band position of the absorption spectrum of a gold spherical nanoparticle of size of 50 nm and the corresponding linear variation of the resonance wavelength.

2.6.3 Dependence on the orientation of the particles in the incident light

The relative orientation of the nanoparticle in the incident electric field determine the induction of the electric dipoles along different symmetry axes and hence, the type of the excited LSPR mode (LM and TM) [18-19]. For the spherical nanoparticles, the type of the incident light has no effect on the type of the excited LSPR mode due to their high order symmetry. In the many fold symmetry particles such as like-rod shapes, the incident light can be polarized in different directions.

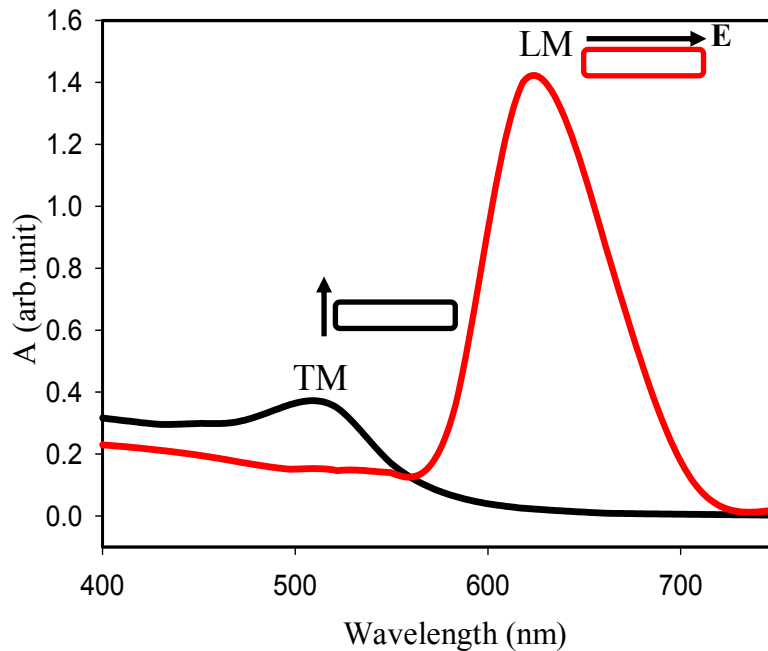


Figure 6: Dependency of the excited type of LSPR mode on the orientation of the gold nanorod of aspect ratio of 3 (the black arrow indicates the direction of incident electric field (E)).

Due to the length distribution of the symmetry axes, different polarization factors are observed and hence many PM can be simultaneously excited. In like-rod shape particles, the LM mode is accompanied with the electronic oscillation along the longer axis while the TM mode determines the charge oscillations along the shorter axes as shown in Figure 6. Depending on the incident angle, the electric field of p-type light (the electric field is parallel to the plane of incidence) might have two components along and perpendicular to the main axis of two old symmetry

nanoparticles. The s-type light (the electric field is perpendicular to the plane of incidence) has one component along the shorter axis leading to the excitation of only the TM.

Figure 6 shows the absorption spectra of plain cylinder (approximated shape for the nanorod) at different orientation relative to the incident electric field of the p-polarized light. When the electric field is oriented perfectly along one of the main axes, a single PM is observed.

2.6.4 Dependence on the morphology of the nanoparticle

The recent advances in the nanofabrication techniques allow the synthesis of well-defined nanoparticles of different shapes and sizes. This capability enables tailoring the optical properties of the nanoparticles over a wide optical range. One of the interesting features in the optical response of the metallic nanostructures is the variation of their optical characteristics with shape. Variations in their morphology results in changing the distribution and the separation of the surface charges and hence the optical response of the nanoparticles [18-19, 111].

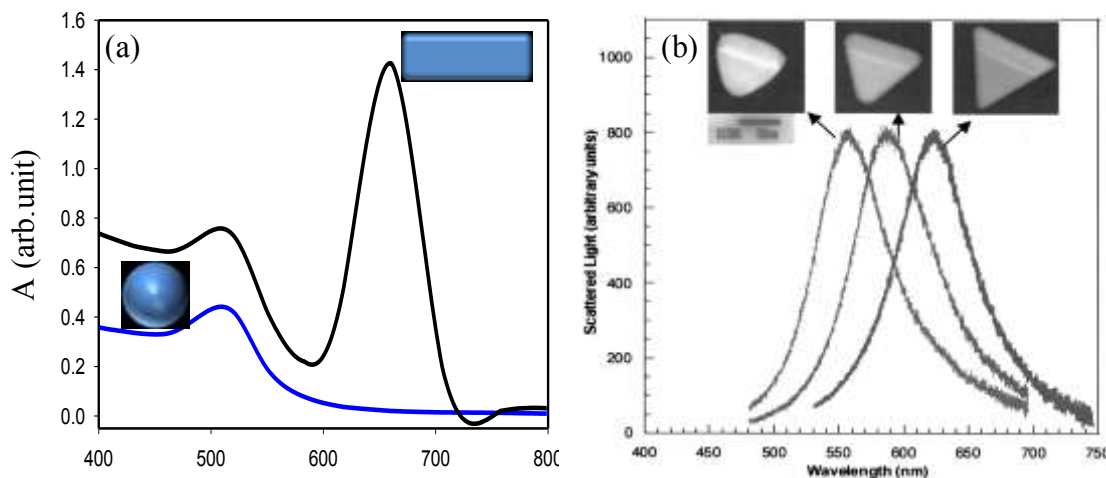


Figure 7: Optical spectra for different gold nanoparticle morphologies. (a) Sphere of size of 20 nm, and a nanorod of length of 60 nm and width of 20 nm. (b) Effect of the sharper edges on the optical response of a single silver triangle; figure is reproduced from reference 112.

The excited plasmonic band is combined with the ways that the particles can be polarized (the particle symmetry axis) [18-19,111-112]. The absorption spectrum of a gold nanoparticle of spherical shape (diameter = 20nm) exhibits one plasmonic band which is attributed to the dipole oscillation in the visible region, while the corresponding spectrum of the like-shape nanorod (length =60 nm, width = 20 nm) shows two resonance bands (TM and LM) as shown in Figure 7.a. The high intense band corresponds to the LM, while the other band corresponds to the TM mode. The accumulation of the surface charges on the sharper corners of the particles yields to a red shift in the plasmonic band as compared to the observed band of a rounded particle [112] as shown in Figure 7.b.

2.6.5 Effect of the coupling in the nearby nanoparticle

The optical properties of the plasmonic nanoparticles clusters are determined by the optical response of the individual nanoparticle and the coupling between the LSPR modes of nearby particles. Depending on the particles separation, the electromagnetic coupling between the PMs is classified into the near-field and the far-field interactions [113-114]. The strong enhancement of the local field originates from the effect of near-field coupling. When the interparticle separation is larger than the incident wavelength, the far-field interaction is dominant.

The electromagnetic coupling between the interacting particles changes the characteristic of their dipolar resonance. The band position of the extinction spectrum of closely spaced nanoparticles is shifted as compared to the one for the isolated particle. The type of the shift depends on the polarization state of the incident radiation. W. Rechberger [115] investigated the effect of the interparticle separation of gold nanoparticles pairs on their extinction spectrum. A distinguished red shift is observed as the separation is decreased for the incident polarization parallel to the connected axis, while a less pronounced blue shift is found for the orthogonal polarization. The anisotropy in their extinction spectra for different polarization direction can be explained in terms of the attractive and repulsive forces between the induced dipoles.

The effect of the particle separation on the dipolar plasmonic coupling of gold nanoparticles arranged in 1D and 2D close-packed array has been studied experimentally [115-117]. The extinction spectra of the particles array reveal the excitation of both the TM and LM. Similar observations have been found theoretically by employing the DDA to simulate the optical response of ultrafine metallic spherical nanoparticles arranged in hexagonal array [18-19, 26].

2.7 Conclusions

This chapter has highlighted the physical origin, the characteristics, and the excitation condition of the LSPR. The fundamental spectroscopic properties of LSPR have been also discussed. The effect of size, shape, plasmonic coupling, incident angle and dielectric function of the host surrounding medium on the optical response of the metallic nanoparticles has been demonstrated. Due to the high sensitivity of LSPR modes to the dielectric constant of the surrounding material, metallic nanoparticles are a strong candidate in sensing application. The change in the adsorbed molecules on the particles surface is monitored by the band position of the metal-LSPR. The resonance wavelength is red shifted linearly with the refractive index.

CHAPTER THREE

Discrete dipole approximation

In the previous chapter, the theoretical background of the resonance phenomenon that occurs locally around particles of finite volume is presented. The optical properties of metallic nanoparticles are also addressed in terms of many parameters (size, shape, type of material, etc). Tailoring the optical properties of the metallic nanostructures of different size and shape is a desired aim for specific applications. Many computational tools have emerged to model the optical properties of these nanostructures. Based on the analytical solution of Maxwell's equation, the Discrete Dipole Approximation (DDA) is a particularly powerful technique to calculate the absorption and scattering cross-sections of nanostructures of arbitrary shape, structure, and composition. In the current chapter, DDA is introduced as a computational tool to model the optical cross-section of the metallic nanoparticles. The basic idea, the mathematical treatment and validity of the adopted method are addressed in detail. The criteria and the applications of DDA are discussed in the subsequent two sections.

3.1 Basic ideas of DDA

The optical properties of an isolated nanospherical metallic particle embedded in a homogenous surrounding medium are well described by Mie's theory [86]. It was the first theory that allowed the calculation of the optical cross-sections of an isotropic spherical metallic nanoparticle. The exact solution of the Maxwell's equation for specific geometries is known, in particular, in the case of a spherical particle, infinite cylinder, and spheroid [118]. Since the exact solution is limited to certain particle shapes, for other morphologies, an approximated solution is often required. Many computational tools have emerged to model the optical response of those nanostructures such as the T-matrix method [119], the Modified Long-Wave Approximation (MLWA) [88], the Finite-Difference Time-Domain method (FDTD) [120] and the DDA.

Among all those, the DDA is considered as one of the most useful and reliable techniques used to calculate the optical cross-sections of the metallic nanostructure of different

shapes, structures, and compositions embedded in an isotropic/anisotropic host material with a complex dielectric function. As compared to other methods, the DDA calculation is less time consuming and it needs less computational resources. As well, the DDA is more flexible regarding the particle shapes and structures. The DDA can be used to calculate the optical properties of metallic nanoparticles near to a flat surface which is very close to configurations of particles produced by nanofabrication techniques. DDA is used effectively for an isolated nanoparticle and for a cluster of particles arranged in a two and three dimensional array in different configurations. The basic idea of the DDA was first introduced to calculate the molar reflection and extinction coefficients of an aggregate system build up from monomer units [121-122]. The retardation effect was not included in the first application of the DDA. Later, the retardation effect was introduced in the DDA to study the optical properties of non-spherical dielectric grains [123]. B. T. Draine employed the DDA to study the optical response of the interstellar graphite grains [124]. He improved the formalism of the method by incorporating a correction for radiative reactions and anisotropic dielectric functions.

In DDA, the polarization charges of the metallic nanoparticles are redistributed as a response of the incident electromagnetic field. Therefore, the electron cloud is shifted relative to the positive core, resulting in an induced electric dipole moment. Based on the interaction between the induced dipoles, the optical response of the metallic nanostructures can be calculated. The target of interest is represented by a three-dimensional array of N dipoles. The induced dipoles are sitting on a periodic square lattice of side length (d) which represents the dipole separation. To provide an accurate description of the target's geometry, a large number of the dipoles is required to mimic properly the structural parameters of the nanostructures. The description of the actual volume (V) of the target solid material depends on the number of dipoles and the size of the square unit lattice (d^3). The size of the target is also characterized by an equal volume sphere of effective radius $a_{\text{eff}} = (4V/3\pi)^{1/3}$. For the sake of accuracy, a large number of dipoles (typically $N > 10^4$) is required to provide an accurate description of the target's geometry.

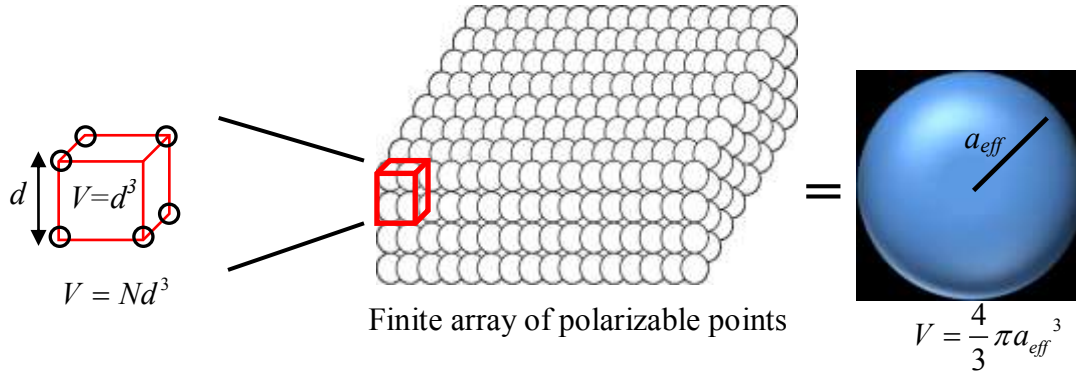


Figure 8: The object is represented by a finite array of polarizable points which are setting on a square lattice of side d (the inter-dipole spacing). The target can be represented as well by a sphere of effective radius of equal volume.

If we equate the volume given by these methods, we obtain the inter-dipole spacing in terms of the effective radius and number of the dipoles.

$$d = a_{\text{eff}} (4\pi/3N)^{1/3} \quad 17$$

DDA method can handle different geometries, sizes, and composites (anisotropic and isotropic). The chosen size of the nanostructure is limited because of the huge number of the dipoles needed to mimic the structure of the nanoparticles which is governed by the available memory.

3.2 Mathematical description of DDA

Consider an incident plan wave with its electric field vector is given as

$$E_{\text{ext}}(r) = E_0 \exp[i(\omega t - kx)] \quad 18$$

Where E_0 and k are the amplitude and the wave vector of the incident radiation, respectively. As stated earlier, the induced dipoles are located on a cubic lattice. The index $j = 1, \dots, N$ runs over the polarizable points in the Target Unit Cell (TUC). The corresponding oscillating dipole moment at each site (P_j) moment located at positions r_j is

$$P_j = a_j \bullet E_{ext,j}(r_j) \quad 19$$

Where a_j is the dipole polarizability given by Clausius-Mossotti (or Lorentz-Lorenz) relation

$$a_j = \frac{3d^3}{4\pi} \frac{\varepsilon_j - 1}{\varepsilon_j + 2} \quad 20$$

where ε_j is the dielectric function of the metallic material. The total electric field at each lattice site has contributions from both the external electric field and the electric field for the other dipoles located in the same particle ($E_{self,j}$). For an isolated particle the electric field vector can be written as

$$\begin{aligned} E_j &= E_{ext,j} + E_{self,j} \\ &= E_0 \exp(i[\omega t - kx]) - \sum_{i \neq j} A_{ji} \bullet P_i \end{aligned} \quad 21$$

Where A_{ji} is the square matrix of order $3N$. If we substitute equation 21 is substituted in equation 19, we have

$$A' \bullet P = E \quad 22$$

Where A' is $3N \times 3N$ matrix built from A_{ji} and E and P are $3N$ -dimensional vectors. Equation 21 represents a particular system of $3N$ complicated linear equations. The Complex-Conjugate Gradient (CCG) method is employed to solve that linear system. The Fast Fourier Transform (FFT) is employed to solve the matrix-vector multiplications involved in the iteration method (CCG). The optical properties can be calculated once the polarization is obtained from the solution of the last $3N$ complex linear equations.

3.3 What does DDA calculate?

The desired outputs of the DDA are the extinction, absorption and scattering cross-sections (C) of the nanostructure, normalized to its geometrical cross section (πa_{eff}^2) which yields the corresponding efficiencies $Q = C / \pi a_{\text{eff}}^2$. The calculated cross-sections are related directly to the oscillating dipole moment and they are given by

1- Absorption cross-section (C_{abs})

$$C_{\text{abs}} : \frac{4\pi k}{|E_0|^2} \sum_{j=1}^N \left[\text{Im}(P_j \bullet (\alpha_j^{-1})^* P_j^*) - \frac{2}{3} k^3 |P_j|^2 \right] \quad 23$$

Where $*$ is the complex conjugate.

2- Extinction cross-section (C_{ext})

$$C_{\text{ext}} : \frac{4\pi k}{|E_0|^2} \sum_{j=1}^N \text{Im}(E_{\text{inc},j}^* \bullet P_j) \quad 24$$

3- Scattering cross-section (C_{sca}) :

$$C_{\text{sca}} = C_{\text{ext}} - C_{\text{abs}} \quad 25$$

3.4 Application and validity of DDA

There are two validity criteria of DDA, the first criterion is $|m|kd \leq 1$, where m and k are the complex function of the refractive index and the wave number of the incident radiation, respectively. By using the equation (17), the first criterion reads as

$$N \geq \frac{4}{3} \pi (|m|ka_{\text{eff}})^3 \quad 26$$

The target with a large value of refractive index or a large value of ka_{eff} will require a large value N to represent the target properly.

One of the fundamental requirements in the modeling is that the inter-dipole separation should be smaller than the incident wavelength and any other structural parameters in the target under investigation. That represents the second criterion. Smaller inter-dipole spacing corresponds to a large value of N , so the target can be described properly. In general, DDA can be applied successfully when the modulus of the refractive index is less than 3 ($|m| < 3$). In the case of a large dielectric function, DDA overestimates the cross-sections. The scattering and absorption problems are characterized by a dimensionless parameter called the size parameter (x), such that

$$x = ka_{eff} = \frac{2\pi a_{eff}}{\lambda} \quad 27$$

The size parameter relates to N and $|m|kd$ by

$$x = \frac{2\pi a_{eff}}{\lambda} = \frac{62.04}{|m|} \left(\frac{N}{10^6}\right)^{1/3} |m|kd \quad 28$$

The effective radius can be written as

$$a_{eff} = 9.873 \frac{\lambda}{|m|} \left(\frac{N}{10^6}\right)^{1/3} |m|kd \quad 29$$

By applying the condition $|m|kd < 1$, so a_{eff} and x can be written as

$$a_{eff} < 4.94 \frac{\lambda}{|m|} \left(\frac{N}{10^6}\right)^{1/3} \quad \text{or} \quad x < \frac{31.02}{|m|} \left(\frac{N}{10^6}\right)^{1/3} \quad 30$$

The limitation on $|m|kd$ translates into the limitation of the ratio of the target size to the wavelength of the incident radiation. The effective radius can be determined from the actual

volume of the target and the equal volume sphere and it can be linked to d and N by using equation 29, simply as

$$\frac{a_{eff}}{d} = 0.62(N)^{1/3} \quad 31$$

The value of d can be easily calculated, it must be small enough, usually in the order of a few tenth of nanometre.

3.5 Conclusions

The DDA method is a flexible technique for computing scattering and absorption cross-sections of nanostructures of arbitrary shape, structure, and composition. Given a target of arbitrary geometry, the DDA breaks up the target by a finite 3D array of polarizable points. The points acquire dipole moments in response to the local electric field. It can be used for a single nanoparticle or for assemblies of particles that are surrounded by a medium with complex dielectric. In the next chapter, the DDA method is employed to model the absorption efficiencies of metallic nanoparticles (gold and silver) of different shapes. The target under investigation is either anisotropic isolated particles of different morphologies or ultrafine spherical particles arranged in planar arrays of different sizes.

CHAPTER FOUR

Optical properties of metallic nanoparticles

In the previous chapter, the DDA method is presented as a computational tool to model the optical properties of nanostructures. In principle, this method is completely flexible regarding the geometry of the target and, to some extent, the size of the target. In the present chapter, the DDA method is employed to calculate in detail the absorption efficiency for both gold and silver nanoparticles in aspects not well explored in previous studies. The nanostructures under investigation are, either single isolated oriented particle of different shapes (nanocube, nanobar and nanoellipsoid), or cluster of spherical particles arranged in 2D arrays of different sizes.

Due to the high symmetry of the spherical nanoparticles, it is expected that their extinction spectrum exhibits a single dipolar plasmonic band typically in the visible region. The isotropic optical properties of the spherical particle can be altered if it is placed close enough to the field of other particles. The anisotropy response in their optical behaviour results in excitation of many PMs. The relative orientation of the nanoparticles to the incident electric field and the type of the incident polarization are the main keys for observing several LSPR modes. The plasmonic coupling between the interacting particles changes the spatial distribution of the polarization charges over the surface area of the particle assemblies. This induces a dramatic change in the electronic oscillations and hence the resonance frequency. The anisotropic optical behaviour as well is observed in the optical properties of nanoparticles of different shapes other than spherical. The geometrical structure of these particles is characterized by many symmetry axes. The anisotropic response of asymmetric particle originates from the diversity of polarization factors along different symmetry axes. Due to the great tunability of the resonance wavelength and local field enhancement of metallic particles, they are strong candidates in many applications and as well, they serve as an ideal platform for active regions in integrated plasmonic devices. Thus, it is of great interest to study in detail the optical properties of these nanostructures.

This chapter is concerned with modeling of the optical properties of metallic nanoparticles of different shapes and configurations. The anisotropic optical properties are discussed for two different cases: first, for ultrafine spherical particles arranged in 2D arrays to show the effect of the coupling on their optical response, and secondly, for isolated asymmetric particles of different shapes to demonstrate the influence of the polarization factor on their optical behaviour. Various parameters are included, such as the type of metal, particle size, particle shape, inter-particle spacing, and orientation of the particles in the incident electric field.

4.1 Optical properties of spherical nanoparticles

The contribution from both the absorption and scattering properties to the extinction efficiency is controlled by the particle size. For nanoparticles of spherical shape, the only size variable is the diameter. For small particles of size of few tens of nanometres, the extinction cross-section is mainly dominated by the absorption one [46.125].

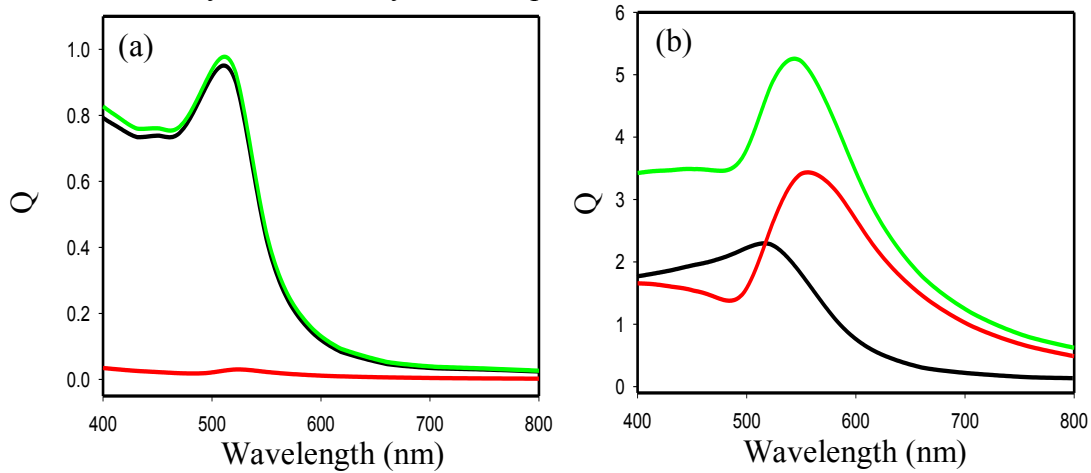


Figure 9: Calculated absorption (black), scattering (red) and extinction (green) efficiencies of a single gold spherical particle of size of (a) 40 nm and (b) 140 nm.

Figure 9 shows the simulated absorption and scattering efficiencies of an isolated gold nanosphere for two different sizes, 40 nm and 140 nm. For the smaller particle, the scattering properties contribute insignificantly to the extinction cross-section and the absorption cross section is comparable to the geometrical one as shown in Figure 9.a. At the resonance

wavelength, the extinction cross-section of the larger particle is about 5 orders of magnitude higher than the corresponding geometrical cross-section. The scattering occurs at higher wavelength as compared to the absorption as illustrated in figure 9.b.

Because of the high symmetry order of spherical particles, their optical response is independent on both the relative orientation in the incident field and the polarization state of the incident light. For modeling of the optical response of the nanostructure under investigation, the gold dielectric function has been extracted from Christy et al [98]. The air is considered as the host medium where the nanoparticles are embedded.

4.1.1 Simulated absorption spectrum of the single isolated ultrafine spherical particle

For spherical particles of size of few nanometres (ultrafine particles), their extinction spectrum is mainly represented by the absorption properties. Since the size of the nanoparticle considered here is comparable or smaller than the mean-free-path (40-50nm)[98] of the conduction electrons, the scattering process of those electrons on the nanoparticle surface has a significant effect on the dielectric function, and further size-correction is required for the bulk dielectric function.

Figure 10.a.b shows both the bulk and the size-corrected dielectric functions for both gold and silver. In the visible region, the real part of the bulk dielectric functions of both metals shows a strong energy dependency and size-independency. Because the real part determines the band position of the PM, no change is expected in the band position of the calculated absorption spectrum by using either the bulk or the size corrected functions. The imaginary part of bulk material shows less dependency on the incident energy as compared to the corresponding one of the size-corrected function. Decreasing the metal size to the nanometric-scale results in more sensitivity to the incident wavelength. Therefore, this affects both the absorption amplitude and the band width of the absorption spectrum.

Figure 10.c shows the absorption efficiency for an isolated spherical particle of size of 5nm. The absorption spectra are calculated using the size-corrected dielectric function and then

compared to the spectrum calculated by using the bulk dielectric function. The band position is not influenced by the scattering process of the conduction electrons at the particle surface. In the case where the size effect is considered, a change in the intensity and bandwidth is observed. It is noted that the size effect usually encountered in the ultrafine particles will generally lead to a broadening of the absorption curves without any shift in the peak locations.

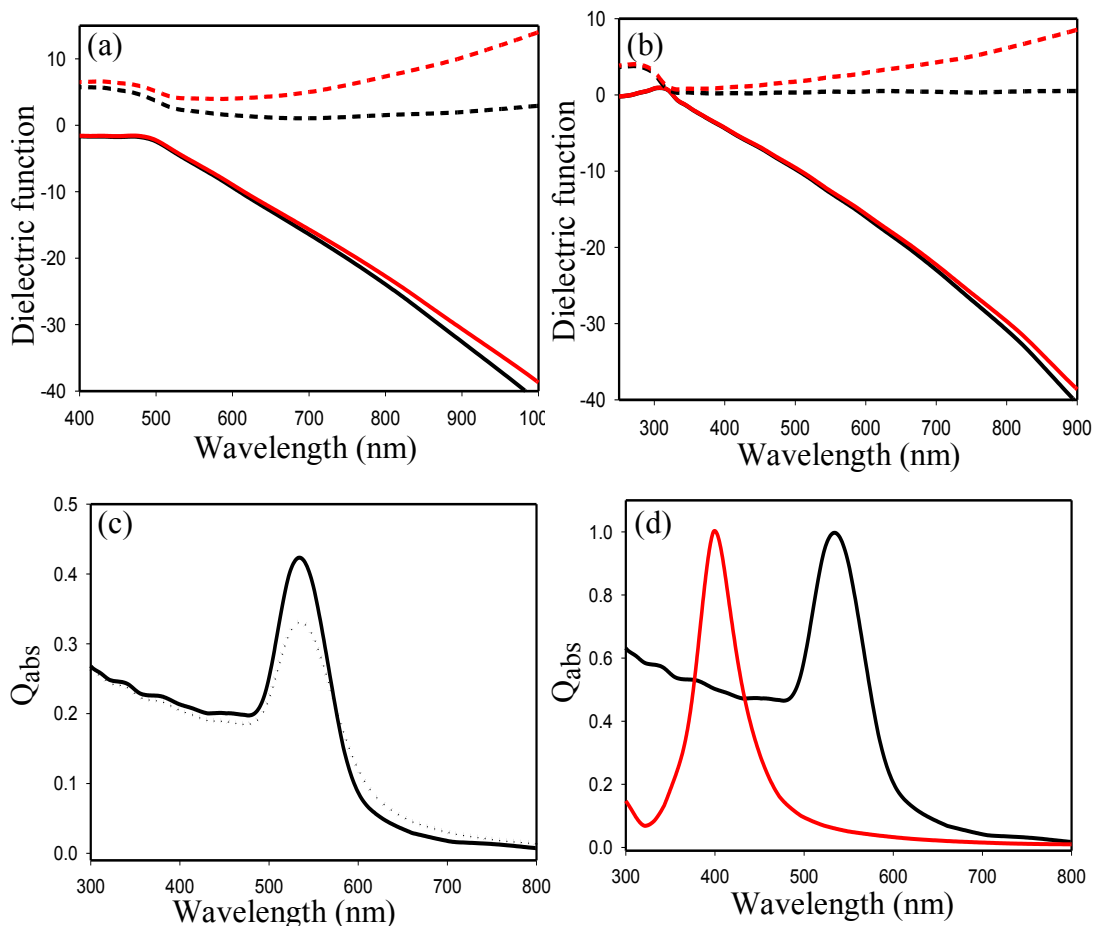


Figure 10: Real (red solid lines) and imaginary (red dashed lines) components of the complex dielectric function of (a) gold and (b) silver nanoparticles of 5 nm in diameter as compared to those of bulk materials (black lines). (c) Absorption spectra for a single spherical particle by using size-corrected (dashed line) and bulk (solid line) dielectric function. (d) calculated absorption efficiency for both gold (black line) and silver (red line) spherical particle of the same size (5 nm).

In the case of the silver spherical particle of the same size, the resonance wavelength occurs at higher energy. For the gold particles, the contribution from the complex interband susceptibility to the dielectric function is more significant than the corresponding contribution for silver. This explains the blue shift of the silver plasmonic band as compared to gold band (equation 11).

For silver, the value of χ_{2b} is small (χ_{2b} approaches zero) at the resonance frequency. The square root of the equation 13 yields 1, therefore, the value of the band width is equal to that described in the free electron model. The real part of the bound electron susceptibility has significant effect on the band position of the PM. It leads to red shift in the resonance wavelength as compared to the one calculated by using the free electron model. In the case of the gold, the imaginary part of the interband transition contributes more to the bulk dielectric function as compared to silver. It adds an additional contribution to the red shift of the band position of the optical spectrum. The width of the gold LSPR mode depends on the magnitudes of both the real and the imaginary parts of χ_b .

4.1.2 Effect of plasmonic coupling on the optical properties of ultrafine spherical particles arranged in 2D arrays

The electric field distribution across the surface of the spherical particle is uniform and thus all the free conduction electrons oscillate in-phase. This results in the excitation of one type of dipolar PM regardless of the type of incident polarization. The isotropic optical response of the spherical particles can be altered either by increasing their aspect ratio (changing the particles morphology) or placing them in close proximity of other particles. In the latter case, the plasmon coupling between the interacting particles changes the distribution of the induced surface dipoles and hence the electric field. This yields a disturbance in the electronic oscillations which results in a significant change in particle optical response.

The effect of the array size (the number of the interacting particles) on the coupling effect of spherical particles arranged in a planar array is addressed in the next sections. This includes

both silver and gold at a specific particle separation where the neighbouring particles interact via their plasmonic resonance.

4.1.2.1 Target geometry of the 2D arrays

The target under investigation consists of a cluster of spherical particles arranged in 2D arrays. The particle size has been chosen to be 5 nm in diameter. The monosized spherical nanoparticles are arranged in a hexagonal close-packed array. The array configuration is arbitrarily chosen, and the results of the simulation are still valid for different close-packed planar configurations (e.g circular and square). The size of the array is controlled by the number of particles used to generate the target. We started with a 7-sphere hexagonal array that was augmented up to a 127-sphere target. The geometry of the target is determined by the location of the individual sphere. Figure 11 shows the geometry of one of the hexagonal arrays that consists of 61 spheres. The inter-particle separation is represented by the border-to-border distance (D) between two nearest-neighbour spheres. To simulate the absorption spectra of the nanoparticle array by DDA, it is required to represent each particle by a sufficient number of dipoles which describes the geometry of the TUC properly. For such ultrafine particles, about 1800 dipoles are sufficient to describe the geometry of the target and achieve a good accuracy with inter-dipole spacing of around a few tenths of a nanometre.

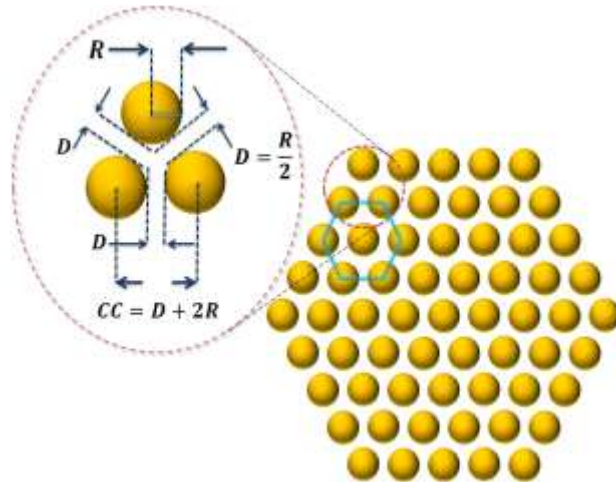


Figure 11: Geometry of 61-sphere hexagonal monolayer array of 5 nm nanoparticles, the interparticle separation is represented by both the border-border (D) and the center-to-center (CC) distances between two nearest-neighbour nanospheres.

4.1.2.2 Target orientation relative to the incident light

The polarization direction of the incident light could be either perpendicular (s-type) or parallel (p-type) to the incidence plane. Under p-polarization, at oblique angles, the incident electric field has two components: one parallel to the target surface and the other one oriented along the yz plane. The electric field of the s-polarized light has one component perpendicular to the target surface at any angle of incidence. No information, therefore, is reported on the excitation of all the PMs. Therefore, the simulations were achieved under p-polarization by considering that the incident light is linearly polarized in the y-direction while it propagates along the x-direction. In the lab frame, the desired orientation of the target can be achieved by rotating the array with respect to the propagation direction (k) by an angle Θ , as shown in Figure 12. The incident angle can be changed indirectly through a set of angles (Euler angles) which defined the relative target rotation to the lab coordinate system. In the case of unpolarized light, the optical spectrum is calculated as an average over the two polarization directions, and the spectrum exhibits all LSPR modes.

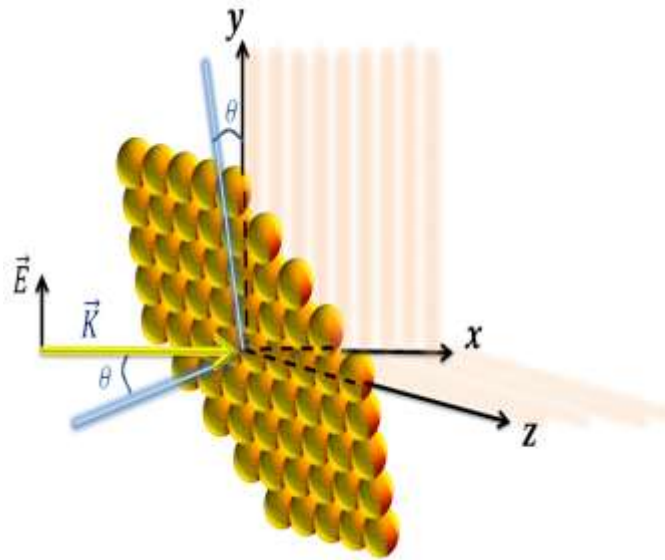


Figure 12: Schematic representation of the target orientation in the external incident electric field (E). K indicates the direction of the propagation of the incident light.

4.1.2.3 Absorption efficiency of the ultrafine particles arranged in a hexagonal array

To investigate the effect of the target orientation on the optical response of the metallic nanoparticles, a series of absorption spectra were modeled by using DDA. The calculations were performed between 0° and 90° in steps of 30° . Due to the anisotropic optical response of the metallic nanoparticles arranged in the 2D array, two different LSPR modes are found. The first mode (LM) occurs at lower energy and the TM mode occurs at higher energy.

At the two extremes of the incident angles (0° , 90°), the absorption spectra of both gold and silver target are characterized by either LM or TM, as shown in Figure 13. The observation of two PMs is attributed to the separation of the polarization charges along two symmetry axes of different lengths. When the incident angle is chosen to be 0° , the incident electric field is aligned parallel to the target surface, resulting in the excitation of the LM. In this case, no other plasmonic band is observed due to the absence of the induced charges along the orthogonal direction. At grazing-incidence, the target can be rotated in such a way that the electric field has one component perpendicular to the target surface. This distinct orientation ensures the excitation of the PM perpendicular to the direction of the propagation.

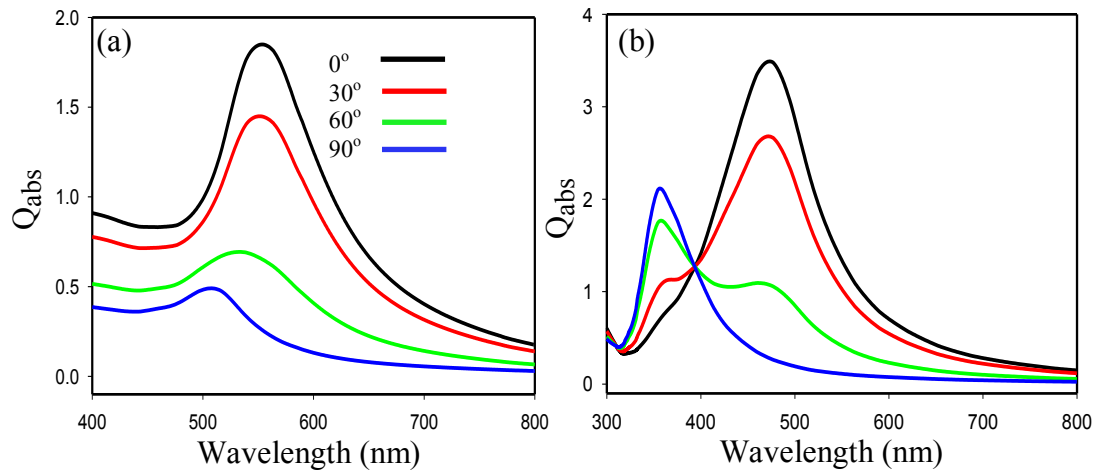


Figure 13: Absorption spectra of (a) gold and (b) silver ultrafine particles arranged in a close-packed hexagonal array of 61 spheres.

At intermediate angle of incidence ($15^\circ < \beta < 75^\circ$), the intensity of both TM and LM contributes to the intensity of the Au-PM. The intensity of LM and TM modes depends strongly on the incident

angle. The LM is inversely related to the angle, while the TM is directly proportional to it. In reality the band positions of both modes are very close to each other, making them indistinguishable and resulting in the excitation of a single broadened band (hybrid PM) as shown in Figure 13.a. The amplitude of the hybrid mode is decreased with the incident angle. Decreasing the value of θ results in increasing the amplitude of the excited electric field along the target surface. The latter enhances the absorption amplitude and shifts the PM to lower energy. The energy difference of the Ag-PMs is larger as compared to the calculated one for gold, resulting in well-separated modes. Therefore, the two PMs can be observed simultaneously when $15^\circ \leq \theta \leq 75^\circ$, as illustrated in Figure 13.b. The previous observations of the dependency of the absorption amplitude on θ are still valid for the Ag-PMs. The resonance condition of the LM is fulfilled at a higher wavelength as compared to the TM. This can be explained by the difference in opposite charges separation along the two different symmetry axes. The energy difference between both modes can be controlled by modifying the interparticle separation. The latter influences the coupling effect between the interacting particles and hence changes the resonance frequency of the PMs.

4.1.2.4 Effect of the array size on the optical properties of particles

To investigate the effect of the target size on the optical response of the metallic nanoparticles, the particles are arranged in close-packed hexagonal arrays of different sizes. As is mentioned earlier, the size of the array is controlled by the number of the particles used to generate the target. The absorption efficiency as a function of the incident wavelength is plotted for the six different sizes of hexagonal arrays of gold nanoparticles at both extreme values of the incident angle.

The amplitude of the absorption spectrum increases with the array size, so that the number of spheres used to represent the target is directly proportional to the absorption intensity. In the case of normal incidence, the band position of the LSPR is blue shifted as the array size is decreased as shown in Figure 14.a. As the incident angle is increased, a second absorption band is observed at higher energy with a lesser amplitude as compared to the low-energy band. The band position of the PM at grazing incidence is blue shifted with target size, as illustrated in

figure 14.b. Therefore, as the size of the target is decreased, the LM and TM move toward each other. When the target is composed of gold nanoparticles, both modes are not well-separated at intermediate angles. Therefore, the influence of the target size on simultaneously excited PMs is addressed for the silver target. Figure 14.c shows the calculated absorption spectra for the silver target at incident angle 60° . Every spectrum is characterized by the excitation of both LM and TM. Increasing the target size will result in increasing the difference in the resonance wavelength between the two PMs. Therefore, well-separated modes are observed.

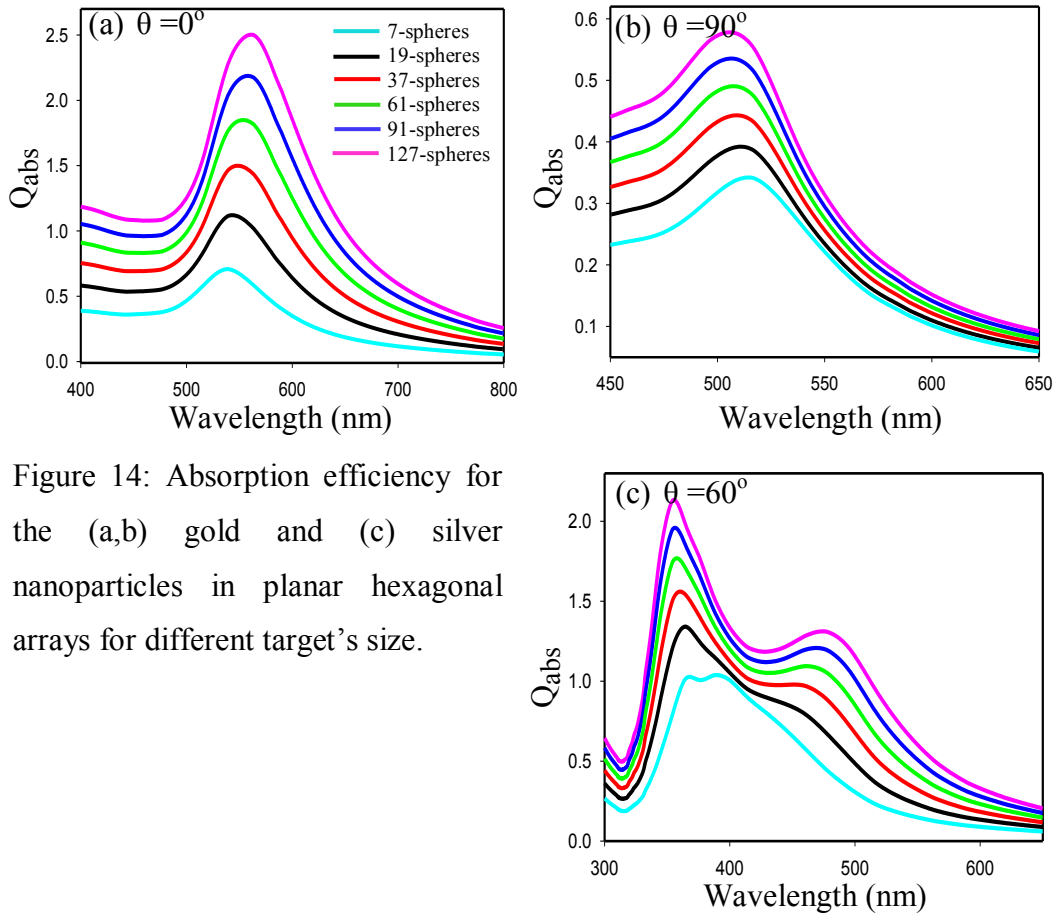


Figure 14: Absorption efficiency for the (a,b) gold and (c) silver nanoparticles in planar hexagonal arrays for different target's size.

4.2 Optical response of anisotropic nanoparticles

Nanoparticles of different morphologies show a distinguished optical properties-size dependency. Changing the morphology of the nanoparticles resulted in altering the symmetry order, which has a dramatic effect on the distribution of the polarization charges over the surface

area of the nanostructures. The redistribution of the charges results in tuning the frequency and the type of the excited PM.

Due to the symmetry of spherical nanoparticles, only one absorption band is observed which is attributed to the dipolar plasmonic resonance. As the morphology of the spherical particle is changed to that of rod-like shapes (such as nanorods and ellipsoidal particles), the single plasmon band splits into two/three bands, LM and TMs due, respectively, to the oscillations of the polarization charges along and perpendicular to the major axis of the elongated particles. The observation of different PMs depends on the particle fold symmetry, the length of the symmetry axis, angle of incidence and the type of the metal [10-11, 13]. Investigating the effect of these parameters on the optical characteristics of LSPR of the metallic nanoparticles is discussed in the following sections. Two different particle shapes are considered here, which are nanobar and nanoellipsoidal particles. These particles represent two and three symmetry order, respectively.

4.2.1 Morphology and structural parameters of the targets

Updated nanofabrication techniques are indeed able to produce well-defined nanoparticles of different shapes and size distributions and even an ordered 2D array of different configurations [37-38]. Among the interesting nanostructures, one can cite the nanocubes, nanobars and nanoellipsoids. These particles represent many fold symmetry structures where many PMs can be simultaneously observed. Tuning of the characteristics of the PMs of these particles over a wide range of the wavelength will be useful in applications such as designing the plasmonic solar cells [41-42]. On the other hand, the anisotropic particles have a significant number of hotspots which is considered of great interest for both fundamental studies and practical applications such SERS [43-44].

The nanocube is considered as seeds for the synthesis of the nanobar by stretching the former along one of its axis. The structural parameter of the nanocube is determined by the side length as shown in Figure 15.a. Scanning Electron Microcopy (SEM) images for experimentally prepared particles showed that the width of the nanocubes ranged between 20–100 nm [9,35]. Since the nanobars are evolved from the nanocubes, the width of the nanobar cross section will

still be represented by the side length of the preliminary seeds. The structural parameter of the nanobar is defined further by the Aspect Ratio (A.R) (the actual length (L) divided by the width (W)) as illustrated in Figure 15.b. The effective radius of the equivolume sphere for the nanocube and the nanobar is $r_{\text{eff}} = (3/4\pi)^{1/3}W$ and $r_{\text{eff}} = (3W^2L/4\pi)^{1/3}$, respectively.

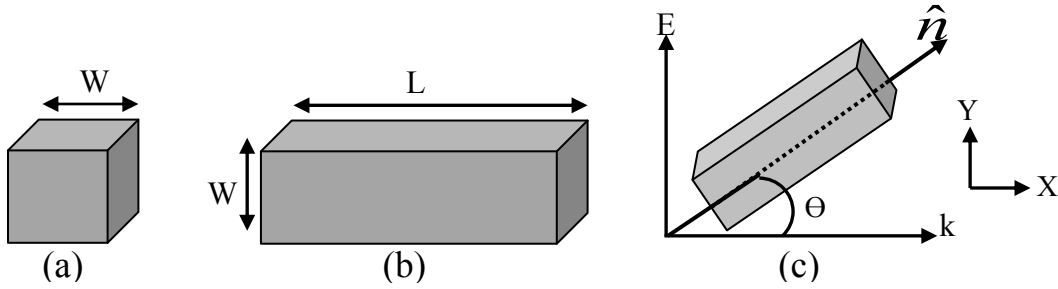


Figure 15: Structural parameters of (a) a cube, (b) a nanobar, (c) orientation of the nanobar with respect to the incident radiation (p-polarized light).

The geometry of the other target under investigation is a quadric surface where the morphology is characterized by three semi-principal axes. The structural parameters of the ellipsoidal nanoparticles are represented by two semi-minor ($2b$ and $2c$) axes oriented along the y and z axes, respectively, and a semi-major ($2a$) axis perpendicular to the yz plane.

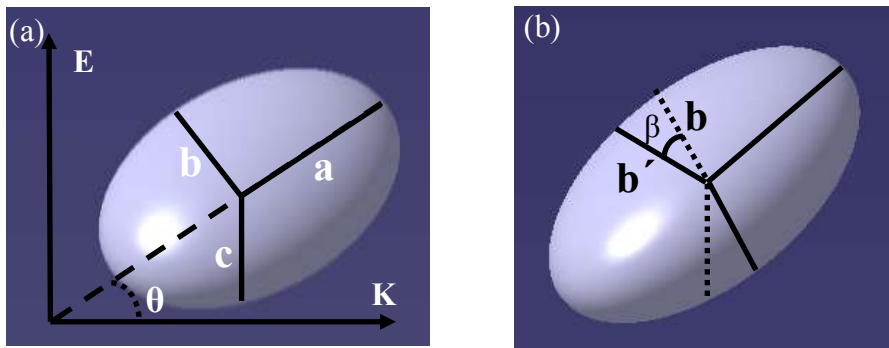


Figure 16: (a) Geometrical parameters of the ellipsoidal nanoparticle, and the orientation of the particle in the lab frame around the x -axis with angle θ , (b) the rotation of the nanoellipsoid in the target frame around the a -axis with angle β .

According to the relative length of the three principal axes, the types of the ellipsoidal particles are classified into oblate spheroids ($a = b > c$), prolate spheroids ($a = b < c$), and scalene ellipsoids ($a > b > c$). The latter case is considered in this study as illustrated in Figure 16. The effective radius of the equivolume sphere for the ellipsoidal nanoparticles is given by $r_{\text{eff}} = (a*b*c)^{1/3}$. The corresponding A.R is defined as the ratio of the longest axis to the shortest axis (a/c).

4.2.2 Orientation of the target

It is assumed that the incident radiation is linearly polarized in the y -direction (p-polarized) and propagates along the x -direction. The orientation of the target in the lab frame is achieved by rotating the major axis with respect to the propagation direction (k) by an angle θ as shown in Figure 15.a and 16.a. At oblique angles, the incident electric field has two components: one parallel to the major axis and the other one oriented along the yz plan. The electric field of the s-polarized light has one component perpendicular to the main axis of the target at any angle of incidence, and no information, therefore, is reported on the excitation of all the PMs. In the case of unpolarized light, the absorption spectrum is calculated as an average over the two polarizations directions, and the spectrum exhibits all LSPR modes. The absorption spectrum exhibits different dipolar PMs when the electric field has a component along each principal axis. When the particles are rotated in the target frame around the main axis by an angle β as shown in Figure 16.b, one/two TMs are observed corresponding to the oscillations of the induced polarization charges perpendicularly to the main axis.

4.2.3 Optical properties of an isolated gold nanocube

Theoretical calculations of the absorption spectra are done by using DDA. All the calculations presented here refer to the air as the surrounding material where the nanostructures are embedded. Since the size of the nanoparticle considered here is larger than the mean free path of the conduction electrons, the scattering process of the conduction electron on the

nanoparticle surface has insignificant effect on the dielectric function, and no further size correction is required for the bulk dielectric function.

To investigate the size effect on the optical behaviour of an isolated metallic nanocube, a series of absorption spectra have been simulated. The side length of the nanocube has been chosen in the range 20–100 nm. In all the simulations, the inter-dipole separation was kept constant at around 1 nm, giving a total of 8000 to 1000000 dipoles per nanocube.

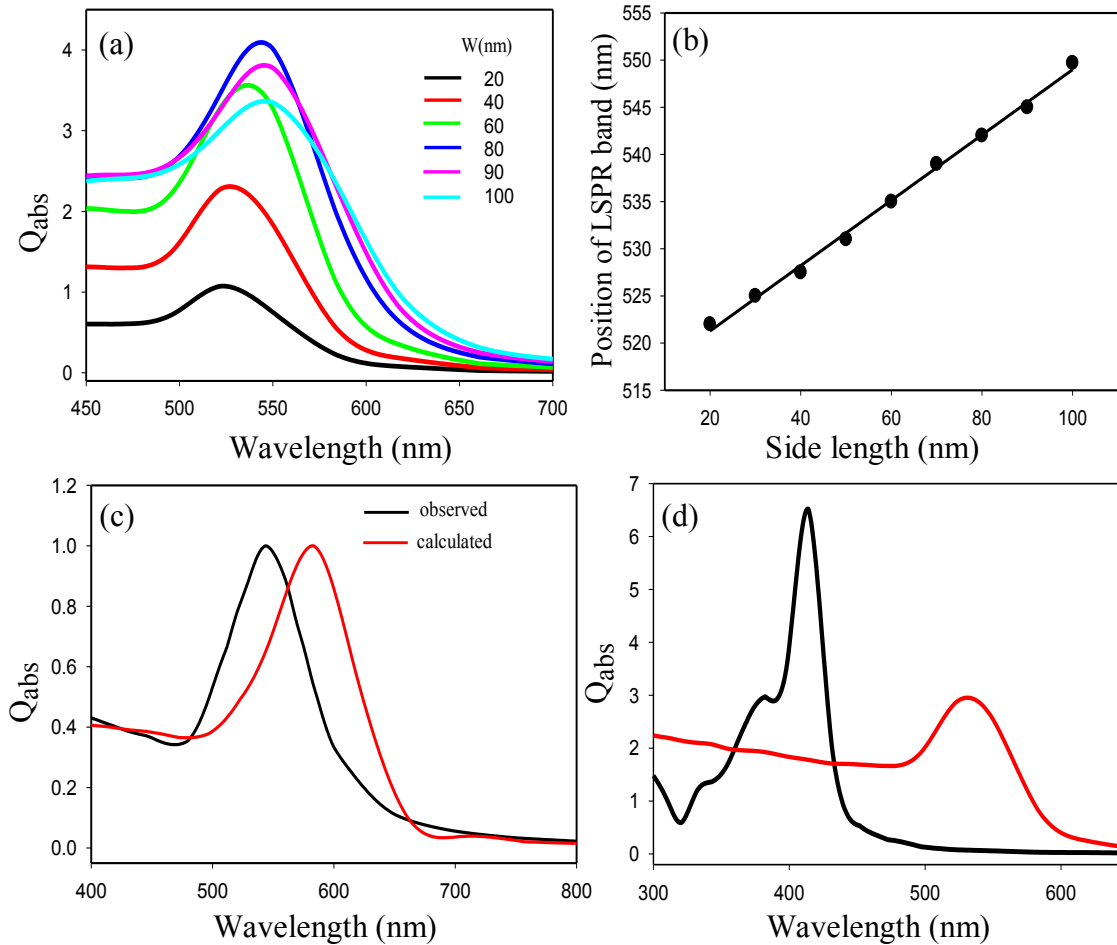


Figure 17: (a) Dependency of the absorption spectrum on the nanocube width, (b) the maximum absorption efficiency as a function of the width, (c) Comparison between observed and calculated absorption spectra of a gold nanocube of width 45 nm embedded in water, (d) Absorption spectra of both gold (red) and silver (black) cubic nanoparticles of the same size embedded in air.

The result of the simulations shows that the absorption spectrum depends strongly on the size of the nanocube. Upon increasing the size, it is found that the amplitude increases with increasing W , the scattering cross-section significantly contributes to the extinction efficiency resulting in a decreased absorption amplitude, that is, when $W > 80\text{nm}$ as shown in Figure 17.a. In addition, the band position of LSPR band is affected by changing the width, and it appears linearly red shifted with increasing side width as shown in Figure 17.b. The observed linear relation is in good agreement with published experimental results in the case of the silver nanocube [126]. The calculated absorption spectrum of a nanocube with a width of 45 nm is compared with the one measured recently by Wu et al. for gold nanocubes in water [127]. The band position of the calculated spectrum is at a longer wavelength as compared to the observed experimental one as shown in Figure 17.c. The difference in the wavelength locations between the experimental and calculated bands would be mainly attributed to the sharp edge nanocube considered in the simulation. The synthesized nanocubes have rounded edges which would result in a blue shift due to decrease in the particle size. Experimental observations of this nature were also made regarding triangular silver nanoparticles with sharp and rounded edges [112].

The observation of the well-separated PM in many fold symmetry particles depends on the type of the metallic particle (e.g silver or gold). The absorption spectrum of the gold nanocube of side length 50 nm is compared to that of silver one of the same size. The calculated spectra of the gold nanocube show the excitation of a single PM as in the case of the sphere. The nanocube has several symmetry axes, thus it is expected that the absorption spectrum exhibits several plasmonic bands. It seems, however, that the band positions of those modes are very close to each other making them indistinguishable, resulting in the excitation of a single broadened band. In the case of the silver nanocube, the plasmonic bands which correspond to the multifold symmetry are well-separated, resulting in the excitation of more than a single band, as shown in Figure 17.d. It is known that the polarization charges accumulated at a sharper area like the corner of the nanocube. That results in an increase in the separation between the electron cloud and the positive core, and thus the electrostatic columbic force (restoring force) is decreased. The increase in the opposite charges separation leads to a red shift of the observed PM as compared to the absorption spectrum for a corresponding spherical particle.

4.2.4 Optical properties of an isolated nanobar

4.2.4.1 Effect of orientation on the optical response of the nanobar

As mentioned earlier, the morphology of the nanobar evolves from the preliminary nanocube seed by elongation along one of its axis, and the cross section of the nanobar is still represented by the side length. As the morphology of the cube nanoparticle is changed to that of an elongated nanobar, the single plasmon band splits into two bands (LM and TM). The splitting occurs at a specific incident angle of the incident p-polarized light. The electric field of the p-polarized light has two components along and perpendicular to the main axis of the nanobar. The s-polarized light has an electric field component perpendicular to the main axis of the nanobar, leading to the excitation of the transverse mode, and the longitudinal mode is not observed even at different incident angles. Figure 18 shows the absorption efficiency of a nanobar of width 40 nm and length 80 nm. The intensity of LM and TM modes depends strongly on the incident angle. The TM is inversely related to the angle, while the LM is directly proportional to it. The band positions of both modes remain at the same wavelength. At the two extremes of the incident angles (0° , 90°), only one plasmon band is observed due to oscillations of the polarization charges parallel or perpendicular to the main axis. At intermediate angles in the range from 15° to 75° , both modes contribute to the total absorption spectra.

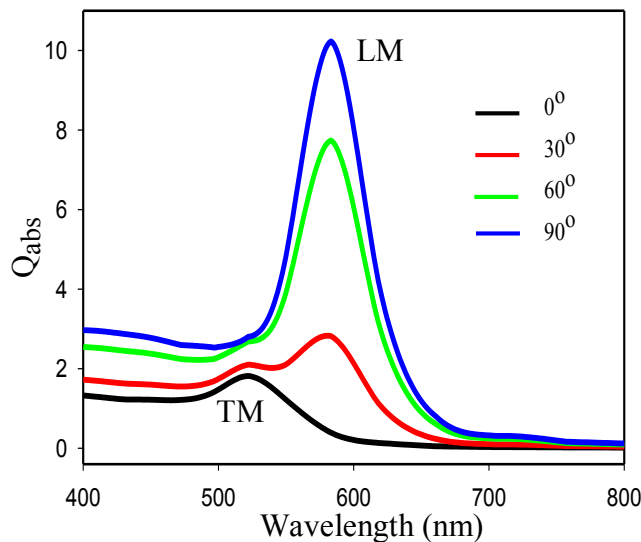


Figure 18: Absorption spectra for a gold nanobar (40 x 80 nm) at different incident angles and p-polarized light.

4.2.4.2 Effect of the length distributions on the optical response of the ellipsoidal nanoparticles

To investigate the effect of the nanobar length on the absorption spectrum, a series of simulation were performed for different lengths. The calculations were performed at a constant width (40 nm) with various lengths $L \in \{60, 80, 100, 120, 140\}$ nm and the corresponding A.R $\in \{1.5, 2, 2.5, 3, 3.5\}$. Figure 19.a shows the calculated spectra at various A.R at $\Theta = 30^\circ$. It can be seen that the plasmon band of the nanocube splits into two modes as the length increases. The position of the longitudinal band is observed to be the major change in the optical response of the nanobar due to the change in the structural parameters, whereas an insignificant change in the band position of the TM has been observed upon the increase in length. The band position can therefore be tuned in both the visible and near infrared regions. The change in the longitudinal band position with A.R shows a linear variation. The linear dependency of the band position of the LM on the A.R has been in fact observed experimentally for metallic nanostructures of different morphologies that included nanorods (characterized by the plain cylinder and spherically capped cylinder) and ellipsoids [9,46, 100].

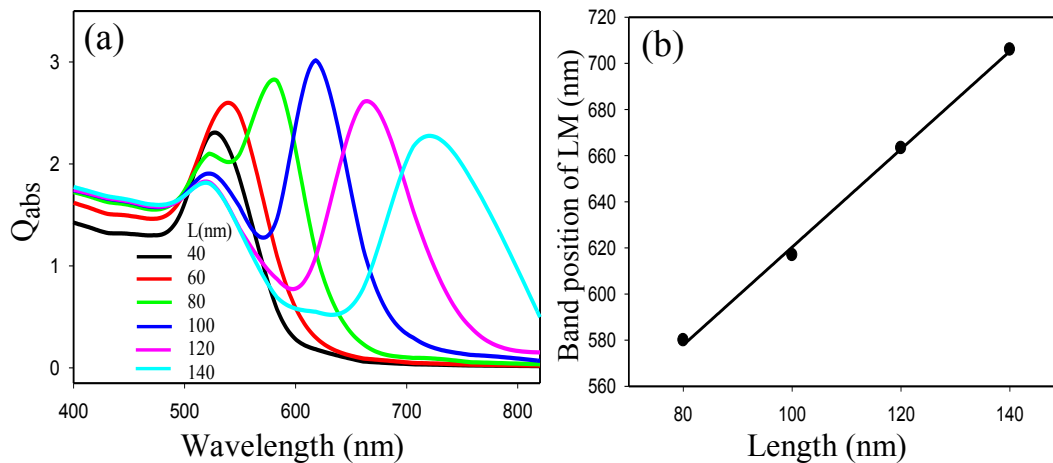


Figure 19: (a) Calculated absorption spectra of a nanobar of width of 40 nm and different aspect ratios at $\Theta=30^\circ$, (b) Position of the longitudinal band versus the nanobar length.

4.2.5 Optical properties of an isolated nanoellipsoid

4.2.5.1 Effect of orientation on the optical response of the ellipsoidal nanoparticles

The angle of rotation (θ) governs the probability of excitation of the LM. The β angle (Figure 16) plays an important role for the observation of TMs. On the other hand, all the possible PMs can be found at a distinct combination between the two angles. In multi-fold symmetry particles, the oscillations of the polarization charges along a certain direction determine the type of the LSPR bands. The redistribution of the charges along the axis of different length changes the separation of the driven electron cloud relative to the positive core, and result in tailoring the intensity and the band position of the LSPR modes.

The effect of the rotation and the orientation of both gold and silver ellipsoidal particles is investigated with the electric field oriented along each of the three axes. Three plasmonic bands are reported due to the oscillation of the charges along each one of them. When the angle of incidence is chosen to be 90° , the major axis is aligned parallel to the incident electric field resulting in the excitation of the LM. Whatever the value of angle β is, no other plasmonic band is observed due to the absence of the induced charges along the other semi-axes. At normal-incidence, the nanoellipsoidal particle can be rotated in such a way that the electric field has one component along either the b-axis or the c-axis, or along both of them. When $\theta=0^\circ$, and $\beta = 0^\circ$ and 90° , the TM along b-axis (b-TM) and c-axis (c-TM) is excited respectively as shown in Figure 20. The excitation of the three distinct PMs of a single ellipsoidal nanoparticle is consistent with experimental data reported earlier [48]. The most intense plasmonic band corresponds to the LM while the less intense one is for the c-TM (for clarity, data in Figure 20 are shown after normalization). The difference in the absorption amplitude would be attributed to the difference in the charge separation (the axis length).

Although the plasma frequencies for both gold and silver would be comparable, the corresponding LSPR mode of the ellipsoidal nanoparticle with the same size occurs at different wavelengths. The deviation originates from the additional contribution of the interband electronic transitions to the dielectric function. The resonance frequency of the LSPR (ω_{LSPR}) [91] is given by equation 12. In the case of the gold nanoparticle, the resonance occurs at higher wavelengths as compared to the one for silver because $\chi_{\text{-Au}} > \chi_{\text{-Ag}}$.

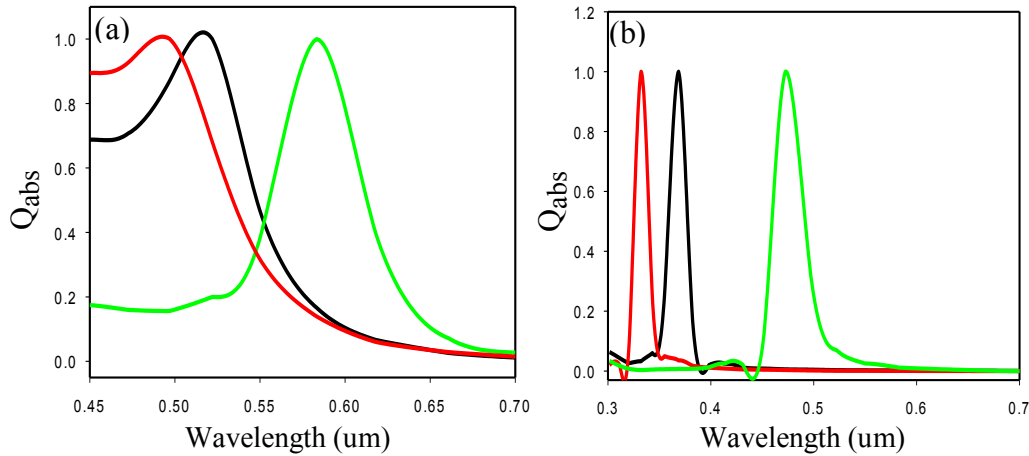


Figure 20: Normalized absorption spectra as a function of the incident wavelength for (a) Au and (b) Ag ellipsoidal nanoparticle. In both cases, the principal axis of the particle is aligned parallel to the incident electric field. The corresponding structural parameters are $2a=40$ nm, $2b=20$ nm and $2c=10$ nm. As well, the observed red shift in the LM as compared to the corresponding one in the TMs could be related to the decreasing in the restoring force (the columbic interaction) due to increase of charges separation along the longer axis.

The Full Width at Half Maximum (FWHM) can be compared between the different LSPR bands for both metallic particles. It can be seen that the LM has the larger value among the modes; the Ag-TMs have a comparable width while the Au-b-axis-TM is broadened as compared to the corresponding c-axis-TM. The value of FWHM for the noble metals [91] is given by equation 13. For silver, at the resonance frequency, because of the small value of χ_2 (χ_2 approaches zero), the square root of the equation 13 is about unity, therefore the value of the bandwidth is equal to γ as described in the free electron model. In the case of gold, the imaginary part of the interband transition contributes more to the bulk dielectric function as compared to silver. Therefore, the square root is larger than unity and hence the corresponding band width is larger than γ . This would explain why the PM of the gold nanoparticle is broadened as compared to the one for silver.

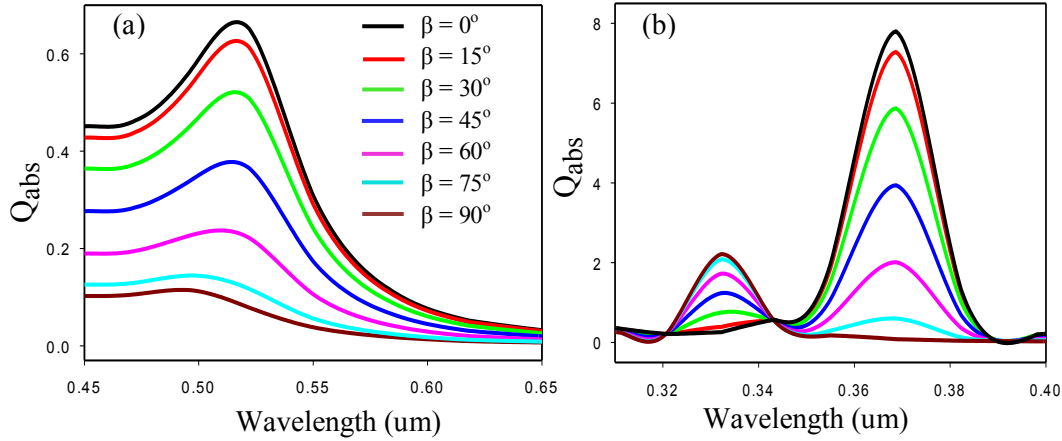


Figure 21: Dependency of the absorption efficiency on the rotation angle for (a) Au and (b) Ag ellipsoidal nanoparticles. The corresponding structural parameters are $2a= 40$ nm, $2b=20$ nm and $2c= 10$ nm.

In the case of the gold ellipsoidal particle, when the excitation of the LM is not possible, and the rotation angle is between 0° and 90° , apparently only a single TM is observed. In reality the band positions of the TMs are very close to each other, making them indistinguishable, resulting in the excitation of a single broadened band that we would label as a hybrid TM as illustrated in Figure 21.a. The plasmonic bands which correspond to the multi-fold symmetry are well separated in the case of the silver particle, showing the excitation of more than a single band (Figure 21.b). When $15^\circ < \beta < 75^\circ$, the intensity of the Au-TM has contributions from both b-TM and c-TM. The amplitude of the hybrid TM is decreased with β . Decreasing the value of β results in increasing the amplitude of the excited electric field along the b-axis. This enhances the absorption amplitude and shifts the TM to a lower energy. The energy difference of the Ag-TMs is larger compared with the calculated one for gold and it resulted in well separated modes. No change in the band position of Ag-modes is observed due to change in the rotation angle. Previous observations of the dependency of the absorption amplitude on β are still valid for the Ag-TMs.

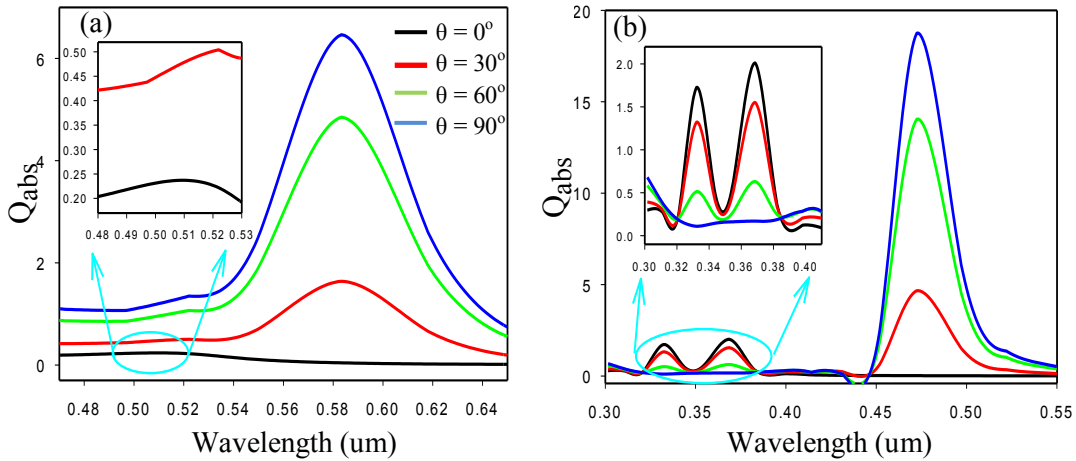


Figure 22: Dependency of the absorption efficiency on the incident angle at a constant rotation angle ($\beta=60^\circ$) for (a) Au and (b) Ag ellipsoidal nanoparticles. The insets represent the spectra in selected wavelength ranges.

The LM can be excited in the presence of the TMs. To demonstrate this, β has been chosen to be 60° while the incident angle is changed uniformly in steps of 30° between the two extreme values of 0° and 90° as shown in Figure 22. The absorption spectrum of the gold ellipsoidal particle is characterized by the presence of the most intense plasmonic LM band and the hybrid TM band. The intensity of the latter band is decreased dramatically with the incident angle, while the LM-intensity is directly proportional to the incident angle. At $\theta=90^\circ$, the incident electric field is perfectly aligned with the major axis which results in a maximum absorption for the LM. At the other extreme of the incident angle, the LM is not observed and the hybrid TM is predominant. Since the Ag-TMs are well separated, the three plasmonic bands can be observed simultaneously when $15^\circ \leq \beta \leq 75^\circ$ and $15^\circ \leq \theta \leq 75^\circ$. The previous observations regarding the dependency of the plasmonic band intensity on the incident angle remain valid for the silver ellipsoid.

4.2.5.2 Effect of the length distribution on the optical response of the ellipsoidal nanoparticles

To investigate the effect of length distribution on the absorption coefficient, a series of simulation were performed for different lengths of each semi-axis. The dependency of the band position of the dipolar PMs on the axis length is examined for both gold and silver scalene ellipsoidal nanoparticles.

First, at fixed length of b-axis and c-axis with various A.R., the characteristic of the LM is investigated in terms of its length. Secondly, the lengths of the a-axis and c-axis are kept constant at 50 nm and 10 nm, respectively, and the b-axis length is varied with $b \in \{15,20,25,30,35,40\}$ nm with a corresponding $A.R = 5$. Different c-axis lengths with fixed a,b-axis values will be the final case. In all cases, the wavelength of either the LM or the TMs will be plotted versus the axis length.

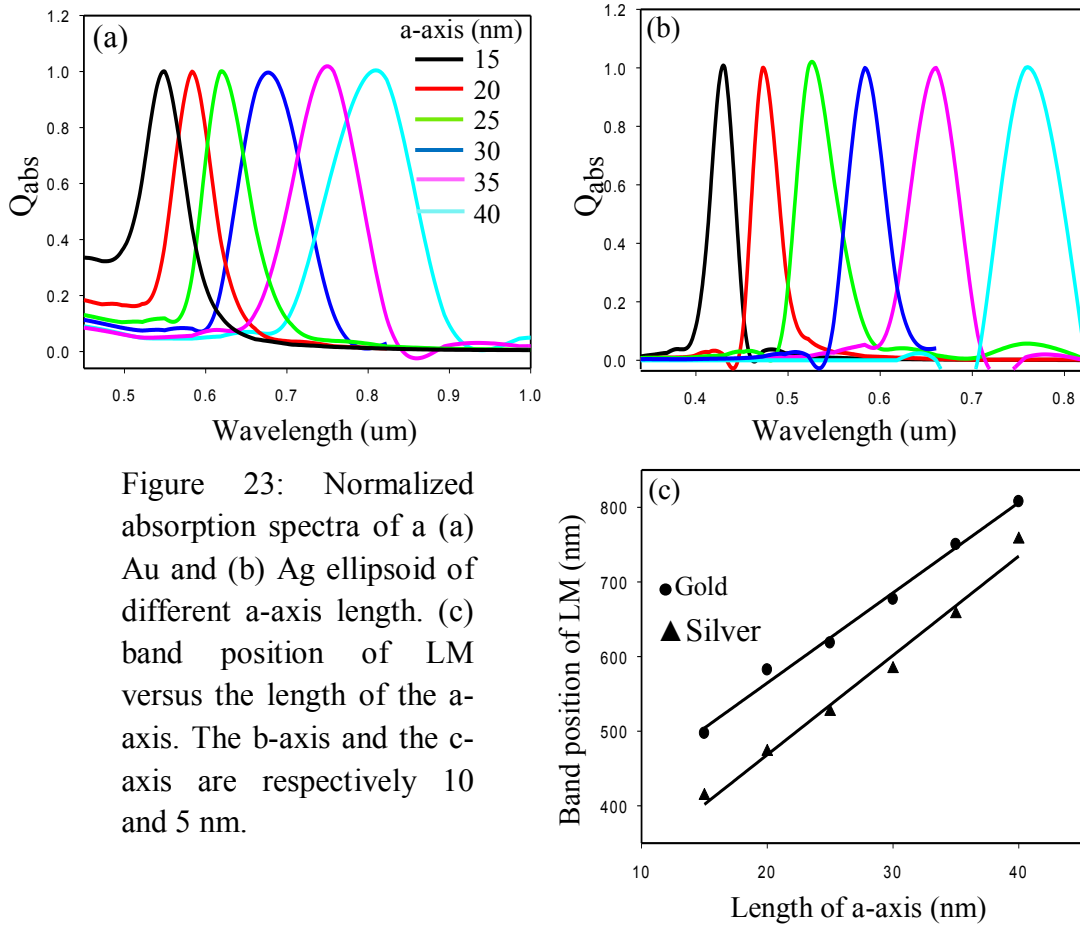


Figure 23: Normalized absorption spectra of a (a) Au and (b) Ag ellipsoid of different a-axis length. (c) band position of LM versus the length of the a-axis. The b-axis and the c-axis are respectively 10 and 5 nm.

The incident angle is set to be 90° when the a-axis is directed along the y-axis. In such a situation, the rotation of the ellipsoidal in the target frame occurs in the xz-plane such that β does not have any effect on the optical response of the particle as shown in Figure 23. The length of the transverse axes is kept constant at respectively 10 nm (b-axis) and 5 nm (c-axis) while the a-axis is varied in the domain $\in \{15,20,25,30,35,40\}$ nm.

To study the influence of the length distribution on the position of the LM, the simulated absorption is plotted versus the incident wavelength for different lengths as shown in Figure 23.a & b. The position of LM is found to be red shifted and its intensity is increased with the length. The band position can therefore be tuned in both the visible and near infrared regions. The Au-LM is broader when compared to the corresponding Ag-LM and the FWHM is increased with the length in both metallic nanoellipsoids. The change in the longitudinal band position with the length shows a linear variation with a comparable slope as shown in Figure 23.c.

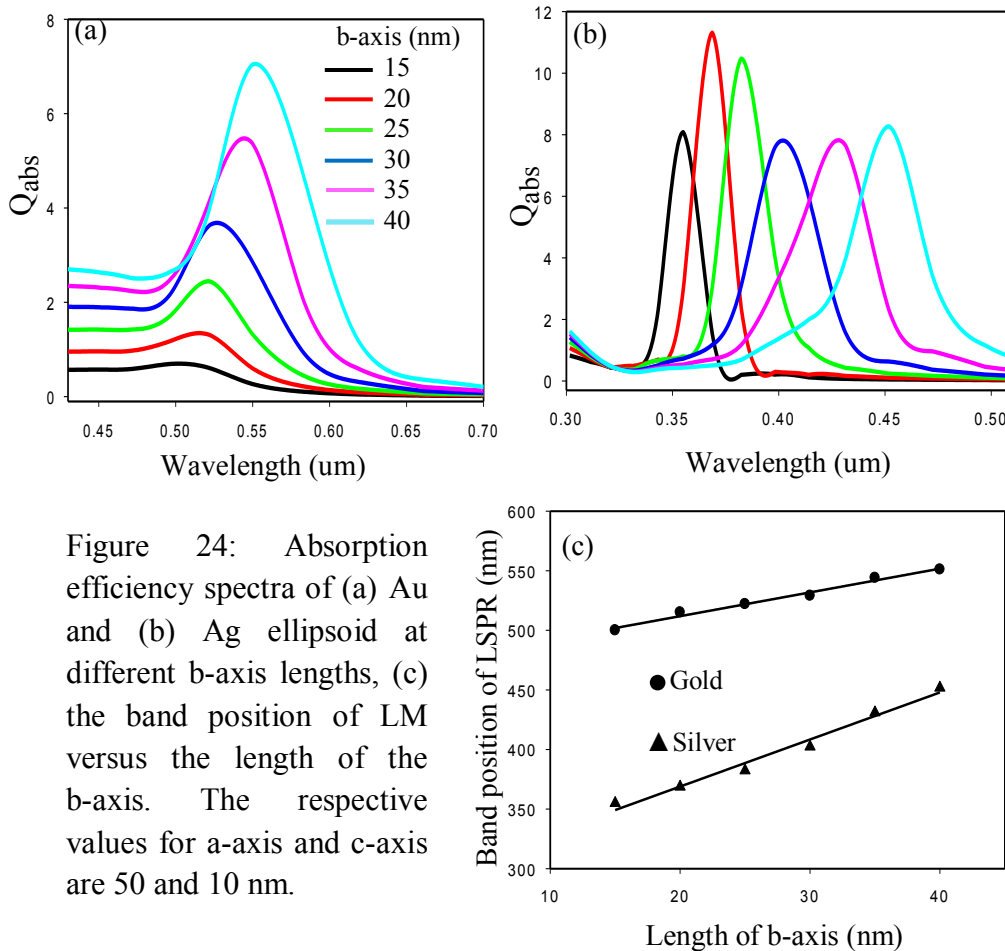


Figure 24: Absorption efficiency spectra of (a) Au and (b) Ag ellipsoid at different b-axis lengths, (c) the band position of LM versus the length of the b-axis. The respective values for a-axis and c-axis are 50 and 10 nm.

The excitation of the Ag-LM occurs at shorter wavelengths as compared to the calculated one for gold. It seems that the difference in the excited wavelength increases with the length, and it is larger in the case of silver as compared with the gold case.

We will now consider the effect of the length distribution of the b-axis on the characteristics of the induced charge oscillation along that axis. The target is oriented in the incident electromagnetic field in such a way that the major axis is parallel to the direction of the propagation and the b-axis is aligned along the incident electric field by ($\beta=0^\circ$). The absorption spectra for the gold ellipsoidal nanoparticles at different lengths of b-axis are shown in Figure 24.a. It can be noted that the band position of the b-TM is red shifted with the length. The change in the excited energy of the plasmonic band is accompanied by a dramatic increase in the absorption amplitude. On the other hand, the optical response of the corresponding silver nanoellipsoid is quite different regarding the change in the intensity and the red shift in the band position of the TM as illustrated in Figure 24.b. The slope of the silver-linear trend is twice compared to the one calculated for gold.

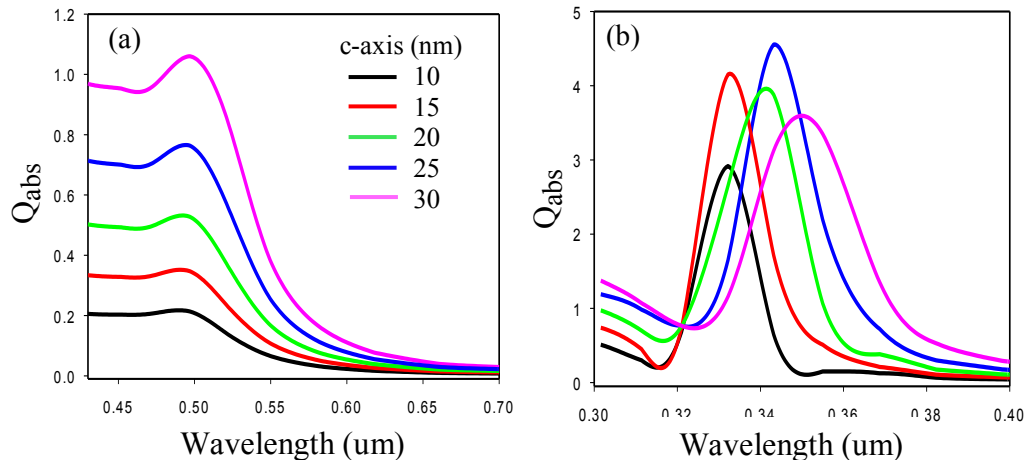


Figure 25: Absorption coefficient of (a) Au and (b) Ag ellipsoid at different c-axis lengths. The respective lengths of the a-axis and the b-axis are 50 and 40 nm.

The band position of the TM excited along the c-axis for gold (Figure 25.a) changes insignificantly with increases in the absorption amplitude while the calculations for silver show

more pronounced changes in both the excited wavelength and the absorption amplitude as shown in Figure 25.b. The band positions of the PMs that correspond to the plasmon oscillations along the b and c-axes show less dependency on the length distribution in both metals as compared with the one found for the length distribution of the a-axis.

4.3 Conclusions

DDA is used to model the absorption spectra for both gold and silver ultrafine spherical nanoparticles arranged in monolayer planar arrays. The results of simulation show that the extinction spectra of an isolated spherical particle exhibit the excitation of single PM. The isotropic optical behaviour of a single spherical nanoparticle can be altered if it is placed in the range of plasmonic coupling of other particles. The anisotropic optical response is represented by the excitation of both LM and TM modes. For particles arranged in hexagonal arrays of different sizes, the band positions of the PMs of silver particles are well separated and are shifted toward each other as the target size decreases. In the case of gold nanoparticles, the energy of both bands is very close, resulting in the excitation of a single band. The effect of the target orientation on the optical properties is also investigated. The modeled absorption spectra show that the excitation of the desired PM is controlled by the incident angle of the incident electric field.

The excitation of different dipolar PMs is also observed in the optical response of an isolated oriented nanoparticle of different symmetry orders. The absorption efficiencies of single nanocube, nanobar and nanoellipsoidal particles are modeled by the DDA method. The type and number of the excited PM strongly depends on the type of metal, the symmetry order of the nanostructure, the length distribution of the symmetry axis and the orientation of the particle in both the lab and the target frames. The absorption spectra of both nanobar and nanoellipsoidal particle show the possibility of simultaneous excitation of many PMs at a distinct combination between the rotation and orientation angles. The structural parameters of the nanobar are characterized by two major axes and hence its absorption spectra exhibit one LM and one TM. In the case of the nanoellipsoidal particle, one LM and two TM's are observed because of the need for an extra axis to define its elliptical cross section. This optical behaviour is shown when the silver nanoparticles are considered. In the case of gold particles, the two TM's are very close to each other making them indistinguishable, resulting in the excitation of a single broadened TM.

The band position of the PMs depends linearly on the axis length for both shapes. An increase in the axis length results in a red shift of the PM band position. The Ag-PMs are relatively more broadened when compared to the ones found for gold nanoparticles. For both metals, the LM shows a stronger dependency on the length distribution of the axis as compared to the TMs.

The tunability of the optical properties of many-fold symmetry particles over a wide range of wavelength is useful in many technical applications such as designing the plasmonic solar cells. Due to the high absorbance of the incident light at different wavelengths in the UV-Vis region, incorporating these nanostructures in the plasmonic solar cell will enhance effectively photoelectrons generation and hence the energy conversion efficiency. On the other hand, the anisotropic particles have a significant number of hotspots which is considered of great interest for both fundamental studies and practical applications such SERS and biosensing.

The synthesis of well defined particles arranged in planar arrays with good control over the shape and the size distribution is a desired goal in many applications. The nanoparticles tend to aggregate and form larger particles or clusters because of their small sizes (high surface energy). To avoid the aggregation process, nanoparticles are integrated in a polymer matrix to form nanocomposite materials. Different types of polymer can serve as a host medium for the metallic nanoparticles. The diversity of the refractive indices and chemical structures (adsorbed molecules on the particles surface) of the polymers, significantly affect the optical properties metallic nanoparticles and hence their sensing capability of the surrounding molecules. In the next chapter, the effect of the dielectric material on the optical properties of gold nanoparticles embedded in a polymer matrix is investigated experimentally.

CHAPTER FIVE

Optical properties of gold- poly(methyl methacrylate) nanocomposite films

The absorption spectra of metallic nanoparticles of different morphologies have been discussed in the previous chapter. The effect of the plasmonic coupling of spherical particles arranged in planar arrays has also been discussed. DDA method was used to model the optical properties of the target under investigation. In all the simulation, air was considered as the surrounding medium where the nanoparticles are embedded. Changing the dielectric function of the surrounding medium and hence the chemical properties of the adsorbed molecules on the surface of particles has a significant effect in the optical response of the metallic nanoparticles. The synthesis of gold nanoparticles in the presence of capping or protective agents (polymer matrix) affects both the growth rate and direction of different facets of nanocrystals and hence the shape and the size distributions of the nanostructures. These parameters will be experimentally explored in the current chapter.

The gold-polymer nanocomposite is a hybrid material that consists of gold nanoparticles integrated into a polymer host material. In the nineteenth century, Faraday was the first who succeeded to synthesis the gold suspension of sub-micrometre-sized particles stabilized in a polymer [85]. Incorporating nano-sized inorganic fillers like metallic nanoparticles in a polymer matrix allows the distinctiveness from both the fillers and the matrix to be combined to provide a novel material with unique physico-chemical and electro-catalytic properties [49-50]. The inherent properties of conjugated-polymer gold nanoparticles make them a potential candidate in many industrial applications [51-53]. The metallic nanoparticles tend to aggregate/agglomerate in the aqueous solution during their formation due to their small size. The most effective strategy to avoid this is preparing the colloidal solution in presence of protective agent like polymers, surfactants and thiols [54-56, 65]. The adsorbances of the protective agent molecules on the particles surface provide a valuable way to control the size distribution and improve the functionality of their surface. By careful selection of the physical environment (matrix) and gold ions-reduction techniques, a novel functional nanocomposite material can be fabricated and

designed for a specific technical application. The choice of the fillers/matrix is crucial depending on the desired properties of the nanocomposite. Frequently used inorganic fillers include metals, semiconductors and carbon-based materials [128]. The polymer matrix could be either transparent polymers (e.g polystyrene (PS), Poly(methyl methacrylate) (PMMA)) or conductive polymers (e.g polyacetylene (PA), polypyrrole (PPY), and polyaniline (PANI)). Due to distinctive optical properties of gold and silver nanoparticles, they are commonly used in the optical and biomedical applications. In such applications, the metallic nanoparticles are synthesized in polymer materials and they are called “optically effective additives” [128].

In general, to prepare gold nanocomposite films by the photochemical reduction methods (microwave irradiation, UV-irradiation and thermal reduction) [57, 60-61], the samples are prepared in a common polar solvent for both the polymer and the gold precursor. Both the UV- and thermal-methods have been used to prepare gold nanocomposite films by using the acetone as a solvent, while, microwave-assisted reactions have been carried out and studied only in solutions by using water because of its high dipole moment and high value of dielectric loss [63]. In the current chapter, MW-assisted synthesis of Au-PMMA material is carried out by using the acetone as a solvent. The optical properties of the nanocomposites are compared to that of nanocomposites prepared by the other photochemical methods. The sensitivity of the Au-PMMA nanocomposite prepared by the three photochemical methods to the refractive index of the dielectric environment is investigated. The effect of the thermal treatment (annealing effect) on the mobility of the nanoparticles in the nanocomposites and hence on their sensing capabilities is compared to the results obtained from non-annealed samples.

5.1 Synthetic technique of gold-PMMA nanocomposite films

PMMA is a lightweight transparent thermoplastic material, often used as shatterproof replacement for glass. Because of its hydrophobic structure, it's a good water resistant. The solubility of PMMA is achieved in organic solvent like benzene, toluene, and acetone. PMMA is more transparent than glass and it has a low glass-transition temperature, so it can be molten and modeled into thin film at a relatively lower temperature. Film casting approach is one of the most

common physical methods to prepare nanoparticles-polymer films. In this method, the polymer is used as a dispersant for the metallic nanoparticles, and then the mixture is casted on a solid substrate by spin coating. The thin film is formed upon evaporation of the solvent in the ambient environment or in an oven.

5.1.1 Experimental details

5.1.1.1 Materials and methods

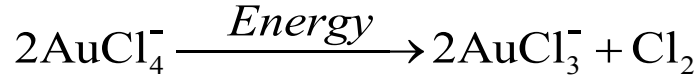
PMMA and acetone were purchased from Sigma-Aldrich, and gold salt (hydrogen tetrachloroaurate trihydrate ($\text{HAuCl}_4 \cdot 3\text{H}_2\text{O}$)) from Alfa Aesar. All chemical were used without any further purification. The UV-Vis absorption spectra were measured by using Perkin-Elmer (model lambda 650) spectrophotometer. The morphology/topography analyses were carried out on both Scanning Electron Microscope (SEM) (Model JEOL JSM-7600 TFE) and Atomic Force Microscopy (AFM) Model NSCRIPTOTM DPN system DS006 (Nano INK) . The AFM imaging were achieved by using a silicon cantilever of rectangular shape with a tip radius <10 nm and stiffness of 52-75 N/ m. The resonance frequency of the cantilever in air is 200-400 KHz. For the annealing process, the samples were kept in an oven at 90-300 °C for 30 min.

5.1.1.2 Preparation the nanocomposite materials

Gold-PMMA nanocomposite was prepared by dissolving 1 g of PMMA in 10 ml of acetone under heating. Then a 100 mg of the gold salt is dissolved separately in 5 ml of acetone. The gold solution is then added to the PMMA dispersion to form gold-PMMA nanocomposite. The molar ratio of the gold precursor to the PMMA kept constant. Subsequently, the nanocomposite mixture is spin-coated on a glass substrate at constant speed 300, 1500 rpm for around 15 and 30 s, respectively. The lower rotational speed is used to ensure a uniform film formation. The gold ions in freshly prepared nanocomposite film are reduced by using three different photochemical methods.

5.2 Results and discussion

The photochemical processes stepwise initiate the reduction of the gold salt into zerovalent gold (Au^0) according to the following reactions [58].



The photolysis of the gold chloride results in forming both chlorine anion (Cl_3^-) and molecule (Cl_2). In the second reaction, the molecule AuCl_3^- simultaneously reduces and oxidizes (dismutation reaction). The gold seed nuclei act as a catalytic material for further dismutation reactions, which results in the formation of the neutral gold. The photochemical methods include UV photo-reduction, microwave-assisted reduction and thermal reduction. Every method is separately addressed below.

5.2.1 UV photo-reduction

The freshly prepared spin-coated samples on glass substrate were irradiated in a Stratagene Strainlinker 2,400 unit equipped with five 25W UV lamps having the wavelength maximum at 254 nm and providing radiation with a power of 7 mW/cm^2 . The samples were kept at a distance of 8 cm from the lamps for different duration times. The effect of the irradiation time on the concentration of the gold nanoparticles is studied. Several samples were prepared with different irradiation times for duration ranging between 90 min and 210 min. Subsequently, the samples were annealed for 30 min at 90°C , as shown in Figure 26.a. It's clear that the gold anions are reduced even for a short irradiation time. The concentration of the gold nanoparticles increases with the irradiation time which is indicated by the increase in the absorption intensity.

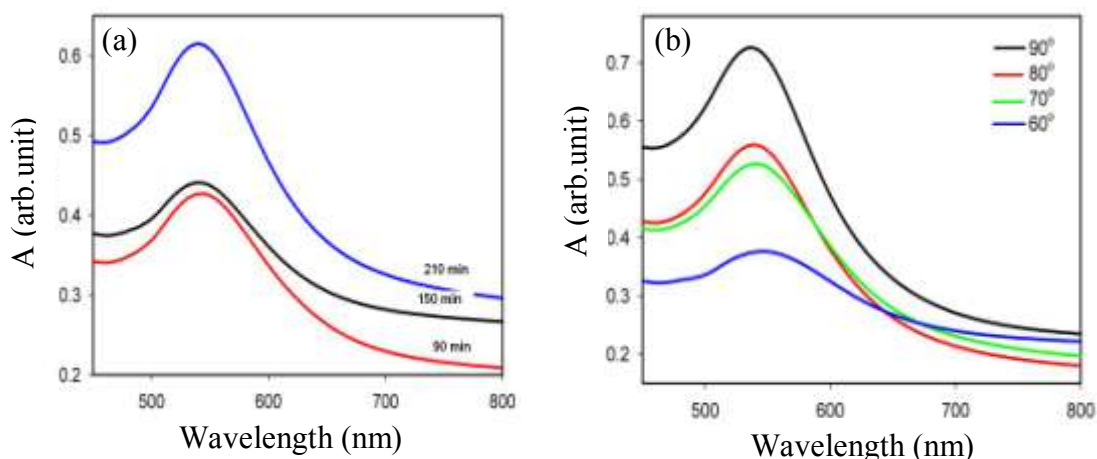


Figure 26: UV-Vis absorption spectra of Au-PMMA nanocomposites corresponding to different (a) irradiation times (sample annealed for 30 min at 90°C) and (b) annealing temperature (time of irradiation is kept constant at 90 min).

There is no change in the band position and band width of Au-LSPR band with the irradiation time; this indicates a narrow size distribution and no effect of UV-exposure time on the particle size. Hartling et al [58] studied the effect of the UV exposure time on the size distribution of gold nanoparticles arranged in 2D planar hexagonal array where they were embedded in PMMA. The exposure time ranged between 1 and 5 minutes. The results showed that the particles have grown monotonically with irradiation time. As well, an increase in the band width with the exposure time has been observed. The variation in the particles shape was noted with time, and anisotropic (elongated) particles have been observed with longer irradiation time.

The UV-irradiated samples were further annealed for different temperatures ranging between 60 °C and 90 °C in step of 10, as illustrated in Figure 26.b. Increases in the annealing temperature will yield increases in the amount of the gold nanoparticles and improve the size distribution. The maximum absorbance is accompanied by a highest temperature near to the glass transition temperature of PMMA with a blue shift of around 10 nm in the peak position. The change in the absorption band position toward lower wavelengths indicates a formation of smaller nanoparticles. The SEM shows the formation of nanoparticles of different shapes including spheres, triangles and hexagons. Even the UV-Vis absorption spectrum doesn't show

any band at higher wavelengths characterizing the presence of shapes other than spherical ones. The other morphologies insignificantly contribute to the observed spectrum because of their low concentrations.

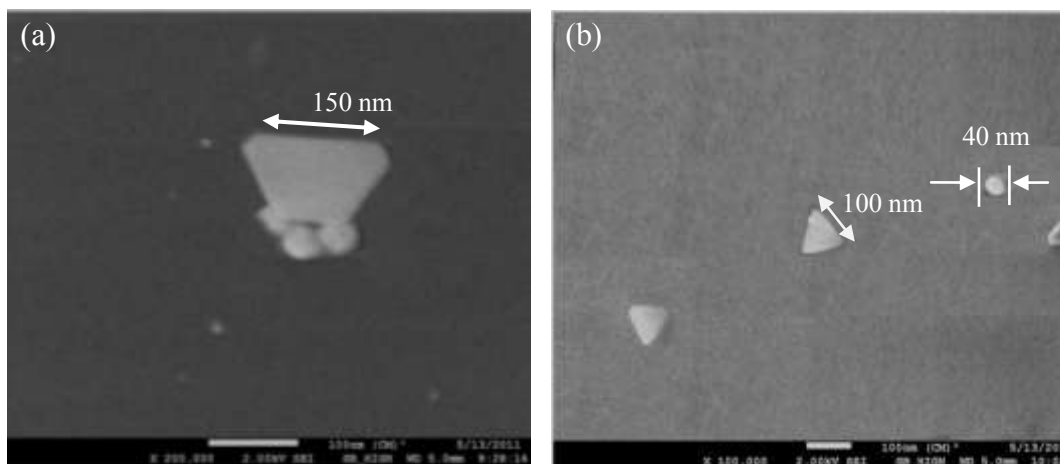


Figure 27: SEM images of samples UV-irradiated for 90 min and annealed for 30 min at (a) 70°C and (b) 90°C.

Figure 27.a shows SEM image of the UV-irradiated annealed sample for 30 min at 70 °C. It can be seen that the gold nanoparticles were produced as plate-like hexagon. Three spherical nanoparticles were observed to stack to the hexagon on one of its facets. They blocked the growth of the facet where they are adsorbed. The formation of nanohexagon was explained by both the different growth rates at different planes of the metallic nanocrystal and the competition between the growth of the nanoparticles and the surface capping process by the polymer [129]. During the particles nucleation stage and the initial stage of growing, a polymer, through its carbonyl groups, would attach to gold nanoparticles non-uniformly. As a result, the growth rate will be different for the different facets, depending on the concentration of the stabilizing molecules.

The effect of the annealing temperature on the nanoparticles shape is investigated. Upon increase the annealing temperature a dramatic change in both the shape and the size has been observed. Figure 27.b reveals that well-defined plate-like triangle nanoparticles of size of 100

nm were generated at higher temperatures, which demonstrate that those nanoparticles are individual crystal with growth direction along the Au (111) plane by using the PMMA as a capping agent [130]. Through the thermal treatment at higher temperature, the sample undergoes re-distribution process of the surface particles. As a result of re-crystallization of the surface nanoparticles, they tend to form a shape of lower surface energy [130-131]. The effect of the annealing temperature on the mobility of gold particles is discussed in the subsequent section.

5.2.2 Microwave-assisted reduction

The microwave-assisted synthesis of gold nanoparticles was carried out by irradiating the mixture of the gold salt and the PMMA for 1–3 min with a power of 1100 W. The conventional heating method usually involves using an oven or a furnace. The advantage of using the microwave irradiation over the thermal method is an increase in the reaction kinetics [132]. Due to the design of the microwave oven, uneven distribution of the energy occurs during the sample heating, this produces a localized heating at the reaction sites. The latter enhances the reaction rate and hence the nucleation process of gold. In our experiment, all the reactants are dissolved in a polar solvent (acetone).

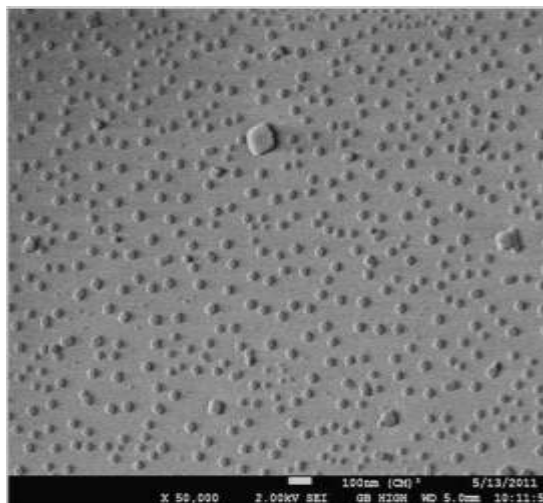


Figure 28: SEM image of the MW-irradiated sample for 2 min.

The polar molecules tend to re-orient in the alternating electric field and they lose their energy in the form of heat by molecular collisions. The ability of the material to dissipate the microwave energy to heat is measured by the dielectric loss constant. Water, acetone and alcohol have the highest value of the dielectric constant and they are ideal for the microwave-heating conversion process.

Figure 28 show the SEM image of PMMA-stabilized gold nanoparticles with an average size of 30 nm using MW-assisted reduction. The SEM reveals a very good coverage and clearly confirms the spherical morphology of gold nanoparticles. No other anisotropic shapes have been observed. The monodispersity of the particle shapes has been reported in silver-starch nanocomposite irradiated by MW [133]. Compared to the UV-photochemical reduction, the MW-assisted approach is preferable for the synthesis of small isotropic nanoparticles. All the samples were prepared with the excess of acetone. Due to its high polarity, it acts as hot spots and, therefore, it generates localized heat sites. The uniform distribution of the acetone all over the sample surface ensures the uniformity of the reduction process of the gold precursor, and hence, a better surface particle density and uniform size distribution.

5.2.3 Thermal reduction

In the thermal reduction method, the gold spin-coated sample is heated in an electric furnace for 15-20 min at 90⁰C. The completion of the reaction is indicated by the change of the color, from yellow, corresponding to the gold anions, to wine red, the color of gold nanoparticles.

Figure 29 shows absorption spectra of two thermal-reduced samples. The reduction process was initiated at two different times after the film casting, immediately and after 30 min. It can be seen that, heating treatment of a freshly prepared nanocomposite film (the film still contains some acetone) immediately after the casting results in the formation of nanoparticles with a well-defined LSPR band at 544 nm. If the heating is delayed by 30 minutes, the band appears to be broader and its intensity is lower. It seems that the acetone facilitates the nucleation process and acts as organizer for the particle distribution. The broader band is attributed to non-uniform size distribution. In the red trace, a weak absorption at longer wavelength can be seen as well. It can

be inferred that heating the film in the presence of only traces of acetone, triggers the formation of anisotropic nanoparticles as well. In this case, the reduction process of gold ions takes place on the spots containing acetone but the main route seems to be a thermal-reduction. Further work is needed to elucidate the mechanism of the reduction in this particular case, and most specifically, the role of acetone.

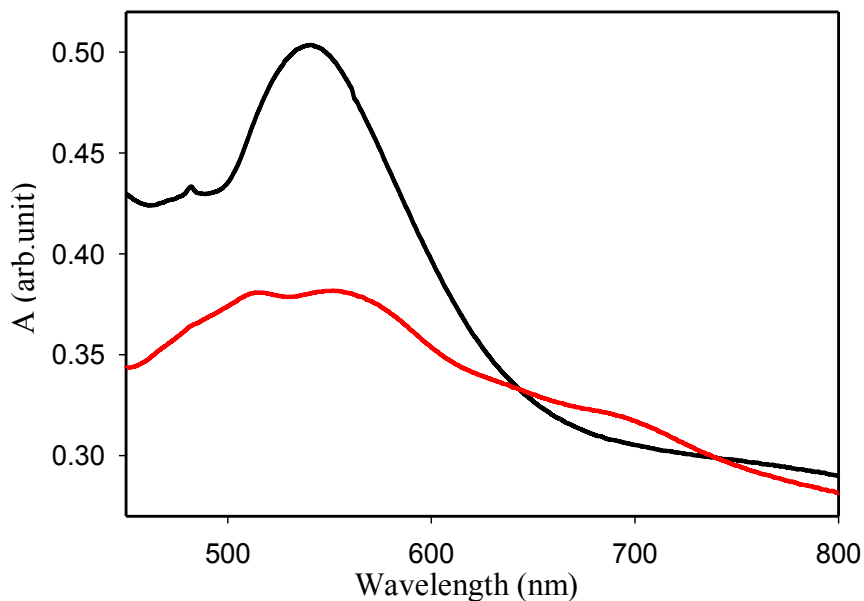


Figure 29: UV-Vis spectra corresponding to the thermal-reduced samples (red: sample is heated after 30 min after the deposition, black: the sample is heated immediately).

5.2.4 Effect of annealing temperature on the surface particles density

To investigate the effect of the annealing temperature on both the nanoparticles mobility and surface particles density, a freshly prepared MW-irradiated sample was annealed for 30 min at 300°C. Figure 30 shows the height-AFM images before and after the annealing process. The images show a significant increase in the surface particles density. Annealing the nanocomposite thin films to a temperature above the glass transition temperature of PMMA would transfer the polymer from the glassy state to the rubbery state. The change in the physical state of the polymer increases the mobility of the nanoparticles. Due to the depolymerisation process, the

presence of the monomers may contribute to the particles shape and mobility. The shape and the size of the nanoparticles are affected by the thermal treatment. During the change of the polymer physical structure and the depolymerisation process, the sample surface undergoes re-organization and some of the small nanoparticles go through a coalescence process. This would increase the average particle size and produce irregular elongated particles, as shown in Figure 30.b.

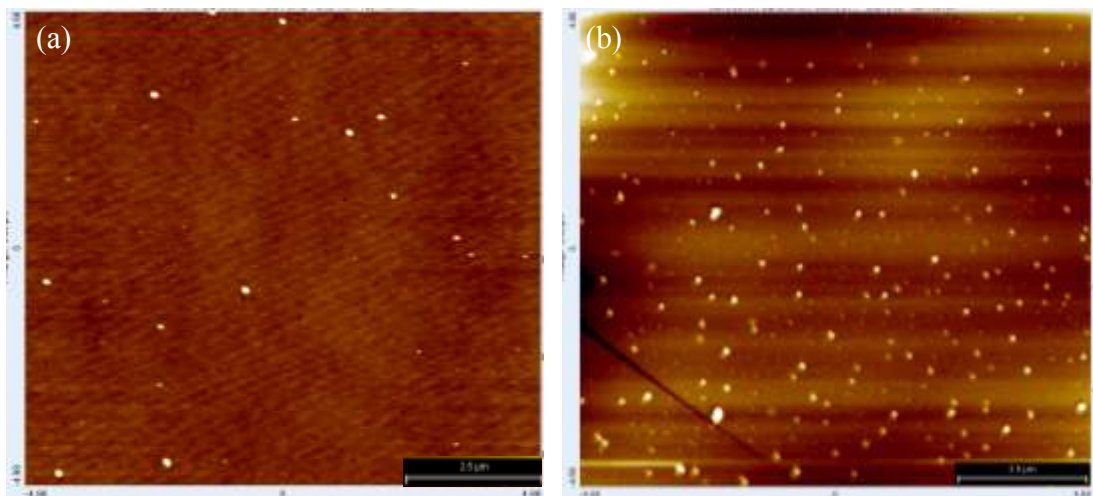
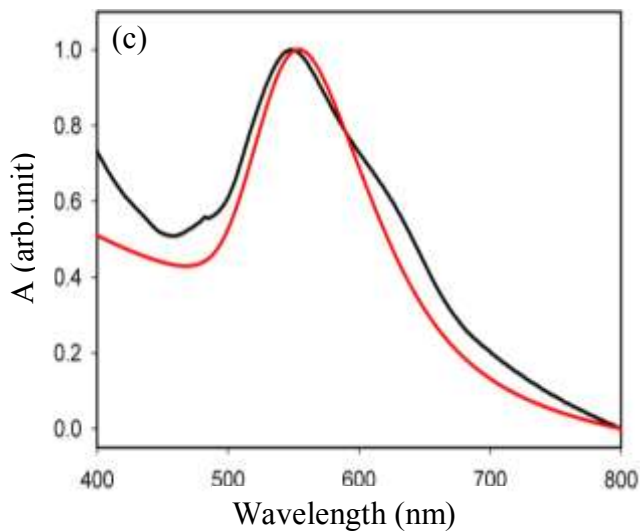


Figure 30: Height-AFM image of the Au-PMMA film on a glass substrate (a) before annealing and (b) after annealing. (c) Normalized absorption Spectra of the Au-PMMA samples prepared by MW-irradiation before annealing (black curve) and after annealing at 300⁰C for 30 min (red curve)



The absorption spectrum of MW-irradiated samples is compared before and after the annealing. The band width of the LSPR band of the annealed sample is smaller as compared to non-annealed one, which indicates a narrower size distribution. Insignificant change in the peak

position of the LSPR of the annealed sample is observed as compared to non-annealed one. The small red shift is attributed to the coalescence of the small nanoparticles into bigger ones.

5.2.5 Refractive index sensitivity measurements

The basic principle of the nanoscale biosensor is based on the change of the characteristics of the LSPR band. The change in the resonance wavelength is caused by the adsorbed molecules from the surrounding environment on the particles surface. The latter induce a change in surface charges distribution and hence the resonance frequency. The local refractive index sensitivity towards the dielectric environment is monitored by the change in the resonance wavelength (λ_{\max}) per Refractive Index Unit (RIU). The used solvents in the sensitivity test and the corresponding refractive indices are listed in table 2.

Dielectric Environment	Refractive index (n)
Water	1.3333
Ethyl alcohol	1.3614
1-pentanol	1.4083
N, N-Dimethylformamide	1.4305
Toluene	1.4969

Table 2: Solvents are used in the sensitivity test and the corresponding refractive indices.

The peak position of the LSPR band is linearly red shifted with refractive index of the host material. The slope of the linear variation ($\Delta\lambda_{\max}/\text{RIU}$) is the measure of the local sensitivity. The sensitivity test for both annealed and non-annealed samples prepared via the three different photochemical methods was compared as shown in Figure 31. The sensitivity test results are summarized in table 3. The results show that the annealed sample is more sensitive to the dielectric environments as compared to the non-annealed one. In all cases, all the samples show low sensitivity to the environment, which can be induced to the low concentration of the surface particles. To enhance the mobility of the surface particle and hence increase their density, the sample should be annealed at a higher temperature (> 300 °C). The higher temperature would further increase the rate of the depolymerisation process and the mobility of the monomers due

to the transition of the polymer physical state. On the other hand, the results show that, in spite of the moderate sensitivity, nanocomposites containing gold can be used for sensing purposes. This result is important because it opens the door to a lab-on-a-chip sensing by using polymer chips.

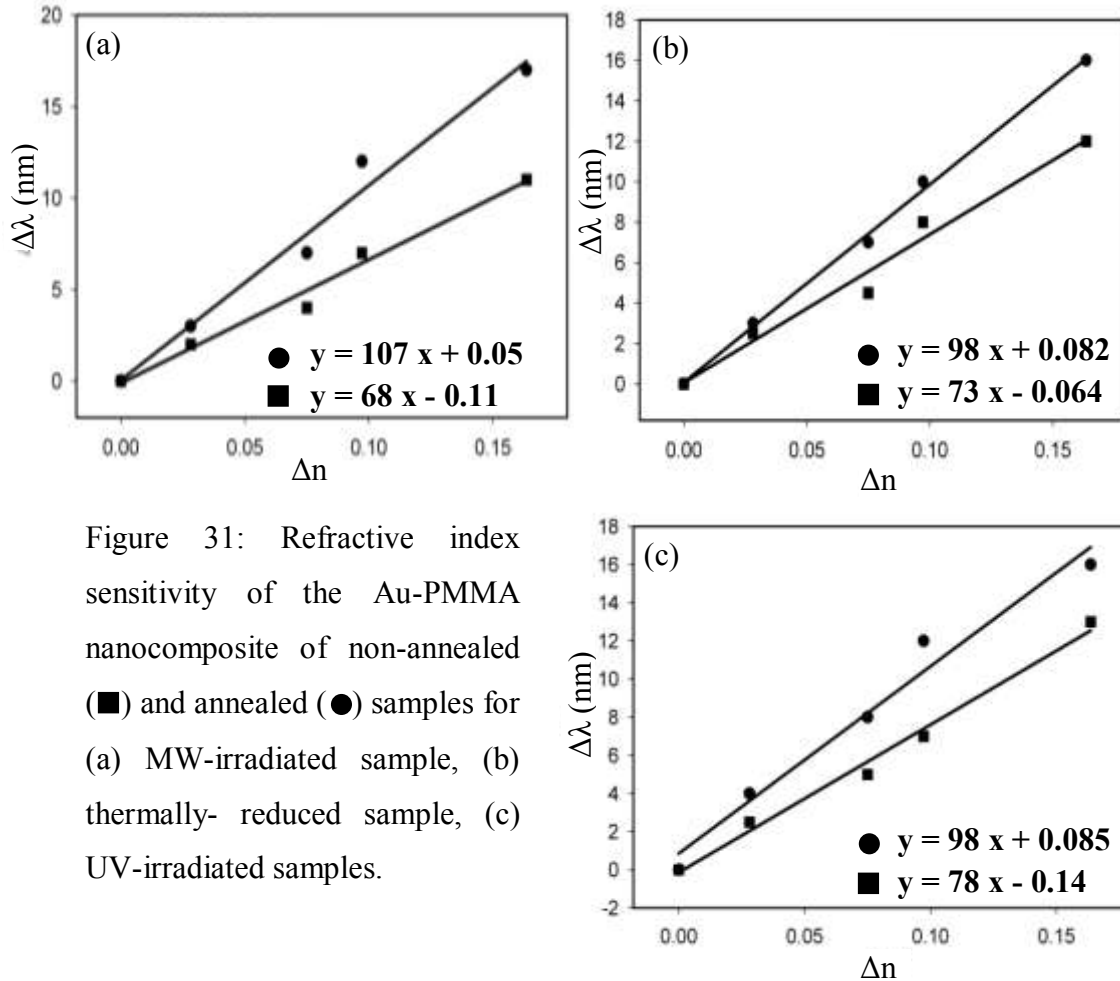


Figure 31: Refractive index sensitivity of the Au-PMMA nanocomposite of non-annealed (■) and annealed (●) samples for (a) MW-irradiated sample, (b) thermally- reduced sample, (c) UV-irradiated samples.

The sensitivity of LSPR nanosensor as compared to the one of SPR nanosensor should be addressed. The sensitivity of the latter is four orders of magnitude higher than the former nanosensor. The difference in their sensitivities originates from the decay length (l_d) of the electric field. For the LSPR sensor, l_d is very short (5-15 nm) [134] and it depends on the structural parameters, the composition and the density of the surface nanoparticles. The SPR-based sensors decay ~15-25 % of the incident wavelength, which means that the decay length is

~200-300 nm [135]. In other words, SPR-based sensor is able to detect any change occurring on the gold planar surface up to ~300 nm in the visible region, while the sensitive capability of LSPR-based sensor is limited to ~15 nm. The sensing area for SPR sensors is determined by the size of the illumination spot, which is in the order of few microns. In the LSPR-based sensing, the sensing spot can be approximated as individual sensing elements (metallic nanosensors). The spot size for LSPR-based sensors can be minimized to a single particle of few nanometres. One of the major differences between the two techniques is the cost and the portability. The portable LSPR-based sensor is much less expensive and smaller in size as compared to the other type of sensor.

Method of fabrication		S (nm/RIU)
UV- Irradiation	Non-annealed	77
	Annealed	98
Thermal reduction	Non-annealed	73
	Annealed	98
MW-irradiation	Non-annealed	68
	Annealed	107

Table 3: The sensitivity (S) results of the Au-PMMA nanocomposite for both annealed and non-annealed sample prepared through the three photochemical reduction processes.

5.2.6 Biosensing experiments by using LSPR nanosensor

Due to the sensitivity of the metallic PM to the refractive index of the surrounding medium, it has been used to detect analyte binding near or at a particles surface and has been widely used to monitor the binding interactions such as adsorption biomolecules, ligand-receptors binding and antibody-antigen binding.

Since the sensing capability of the nanocomposite films strongly depend on the surface particles population, the biosensing experiments are conducted by using freshly annealed Au-PMMA films. The functionalization of the particles surface in the nanocomposite film for the

sensing experiments is required. For this purpose, the annealed samples are immersed into a solution of 1-octadecane thiol solution for several hours. After immersion, a red shift of LSPR band of about 12 nm is observed, the change in the resonance wavelength is accompanied with an increase in the band width, as shown in Figure 32. This means that the change in the characteristics of LSPR band indicates the adsorption of the thiol molecules on the particle surface and they can feel and absorb the surrounding molecules. The broadening of the LSPR band may be due to the unexposed gold nanoparticles. In addition, other effects may also contribute to the broadening such as the polydispersity in nanoparticles size and shape. Indeed, nanoparticles having different sizes and/or shapes interact in a different way with the adsorbed molecules yielding slightly different shifts.

Further, the functionalized gold film is immersed in a buffered solution of antibody to form antibody-conjugated nanoparticles. The conjugation of nanoparticles with antibodies combines the properties of the nanoparticles with a specific and selective recognition ability of the antibodies to other biomolecules like antigens.

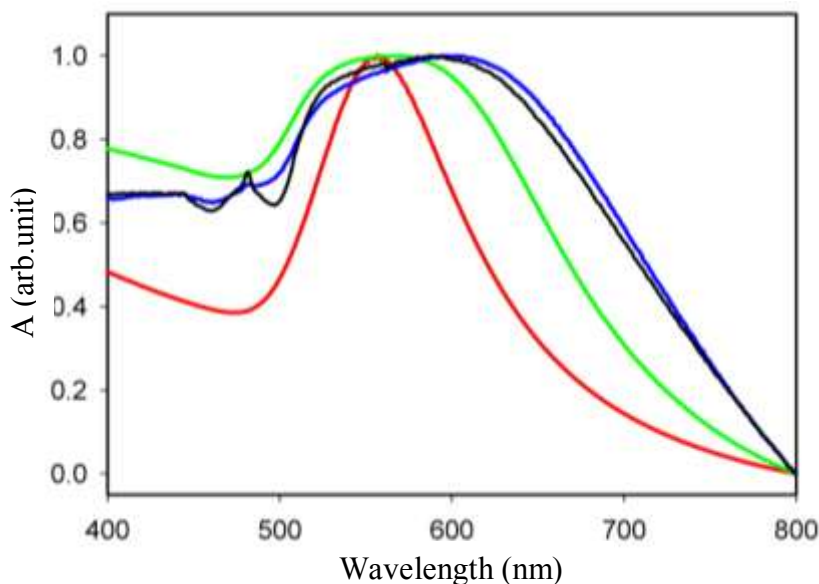


Figure 32: Sensing experiment performed on the annealed sample. Red curve: LSPR gold band in the annealed nanocomposite, green curve: after immersion in ethanol solution of 1-octadecane thiol, black curve: after immersion in the antibody solution, and blue curve: after immersion in the antigen solution.

The adsorption of the antibody molecules on the particles surface is indicated by a further red shift in the Au-LSPR. Finally, the antibody-conjugated sample is immersed in antigen solution. The LSPR band of the biconjugated film is further red shifted. Figure 32 shows, step by step, the changes in the Au-LSPR band, as a result of the changes in the immediate environment. The results reveal that Au-PMMA nanocomposites, annealed to increase the mobility of Au nanoparticles, can be successfully used as sensing platforms for detecting biomolecules. More quantitative experiments are necessary to determine the sensitivity of this platform and the detection limit for different antigens.

5.2.7 Comparison between the observed and simulated LSPR band in Au-PMMA nanocomposite

The observed absorbance spectrum of the gold spherical nanoparticle of a size of 30 nm (size measured in the SEM images) is compared with the simulated spectra (Figure 33) by using both the DDA and Mie's theory.

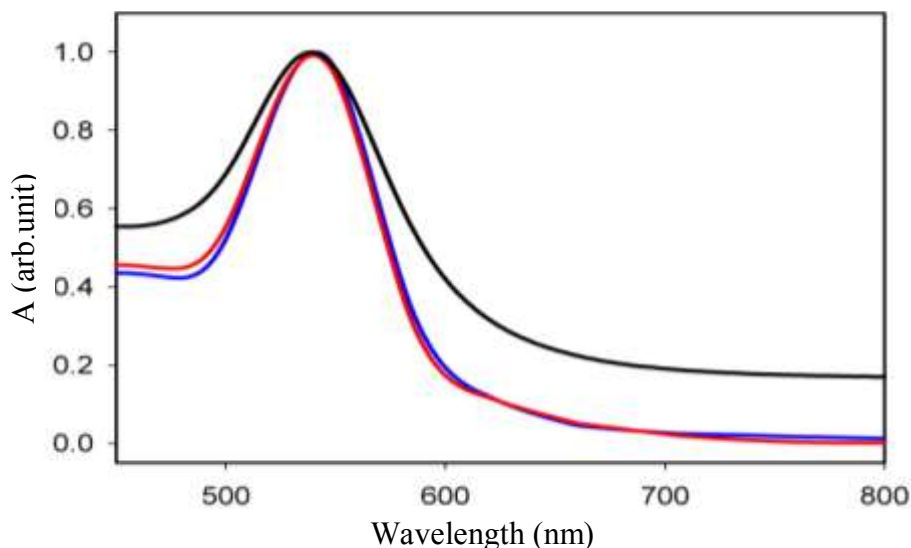


Figure 33: Comparison between the observed (black) and simulated optical properties (blue for the DDA-simulated curve and red corresponding to Mie's theory) of Au-PMMA nanostructure. The curve corresponding to the experimental results corresponds to the MW-irradiated sample.

In the DDA approximation, the inter-dipole separation is chosen to be a few tenths of nanometre, giving a total of about 72000 dipoles, sufficient to mimic the structure of the spherical particle, and to achieve a proper convergence of the simulation. The band position of both the simulated spectra shows an excellent agreement with the observed one. For particles with a size much smaller than the wavelength of the incident radiation, the quasi-static approximation is used. Therefore, the observed LSPR band centered at 540 nm is attributed to the dipolar distribution of the polarization charges. Because of the particles size distribution in the measured sample, the observed band width is larger than the modeled ones.

5.2 Conclusions

Gold nanocomposite materials have been prepared by using different photochemical methods to reduce the gold precursor in the presence of the polymer matrix (PMMA). The reducing methods have a significant effect on both the size and the shape distribution of the gold nanoparticles. The microwave-synthesized composite showed a uniform distribution of spherical nanoparticles, while a large number of triangular particles can be seen as a result of UV irradiation. The size and the shape distribution of the nanoparticles can be improved by thermal treatment (annealing process) of the nanocomposite films. The annealing process at moderate temperature increases the mobility of the polymer chains and, therefore, the nanocomposite films undergo a re-organization process of the surface particles. This increases the particles surface density and hence, more particles will sense the change in the surrounding medium. The sensing capability of annealed samples has been tested and then compared to that of non-annealed samples. The results show that, for both samples, the band position of Au-LSPR is red shifted linearly with the refractive index of the dielectric medium. In the annealed samples, the surface density of gold nanoparticles is highly increased, and, under these conditions, the nanocomposites show an enhanced sensitivity toward the surrounding molecules.

Altering the host medium and the reduction process of the gold chloride significantly affects the optical response and the stability of the gold nanoparticles. In the next chapter, the optical properties of gold nanoparticles are studied in the presence of another host polymer

(gelatin). The reduction of the gold salt is achieved chemically by using a strong reducing agent (sodium borohydride). The released hydrogen gas due to the reduction process may affect both the effective refractive index of the host medium and hence the band position LSPR of the gold nanoparticles and their stability. This is the main issue to be explored in the next chapter.

CHAPTER SIX

Optical and surface properties of gold– gelatin bio-nanocomposite films

In the previous chapter, the optical properties and the sensing capability of Au-PMMA nanocomposite films have been studied. The nanocomposite materials were prepared by using different reduction methods, either thermally or by irradiation. Changing the host material (adsorbed molecules on particle surface) and the reducing method of the metal salt, introduce a useful method for optimizing/controlling both optical response of the nanoparticles and their stability. In the current chapter, a natural polymer is used to prepare gold nanocomposite materials. The reduction methods will be achieved chemically by using sodium borohydride as a reducing agent. The borohydride is considered as a hydrogen gas (H_2) source. The presence of the H_2 in the particles' environment will affect the effective refractive index of the surrounding medium and hence the optical response of the nanoparticles. On the other hand, the gas can be trapped inside the polymer film which results in formation of surface bubbles. This chapter aims at exploring the influence of two-state environments on the stability of gold nanoparticles and the morphological features of gold –gelatin nanocomposite.

The polymers are classified either as synthetic or natural polymers. Examples of the man-made polymers are polystyrene, polyethylene and nylon. The natural or bio-polymers are indirectly available in the nature and can be extracted from the micro-organisms, plants, and animals. One of the most abundant bio-polymer is proteins, nucleic acids, starch, cellulose, gelatin and chitin.

In general, the synthetic polymers are used to prepare metals nanocomposite materials as the one described in the previous chapter. Recently, a new class of composites, called BioNanoComposites (BNC) has emerged. The BNC is a bio-based nanocomposite material where the bio-polymers are used to stabilize the metal nanoparticles against the aggregation. Under certain conditions, the natural polymers can be used to reduce the metal salt (the green synthesis of metal nanoparticles) [66, 136]

Gelatine is water-soluble polypeptide (protein), it is derived from water-insoluble collagen by the hydrolysis. The protein precursor (collagen) is abundant in animals' skin, bones and tissues. The collagen is mainly consisted of three different α -amino acids (glycine, proline, and hydroxyproline) in a triple-helix structure. Due to the presence of both acidic and basic charged functional groups (-NH₂, -SH and -COOH), the gelatine can interact with noble-metal nanoparticles. In principle, because of its steric properties, the gelatin is used as a stabilizing agent. Gelatin-BNCs with well-dispersed gold nanoparticles have been successfully synthesized [137]. The average size of the nanoparticles can be controlled by altering the gelatin to the gold chloride molar ratio.

One of the versatile inorganic reducing agent widely used in chemistry is the sodium borohydride (NaBH₄). Mixing the borohydride with water or alcohol decompose the reductant into hydrogen gas and borates. Under controlled catalytic reaction, the borohydride is used as a hydrogen source for engine/fuel cell systems [138]. It has been used as a foaming agent (hydrogen bubbles) in rubber composites to control their mechanical and chemical properties [139].

The nanoscale gas phase at the interface between the water and the hydrophilic surface has been proved experimentally by using AFM [140-141]. The existence of the interfacial nanobubbles has been used to understand the nature of the long-ranged hydrophobic force [142]. Theoretically, Due to the high pressure within the surface bubbles, the gas pressed out and they collapse in less than 100 ms [143]. Taking into consideration the effect of surface counter-ions density, the lifetime of the bubbles is extended to days or even months. The surface tension tend to reduce their surface area and hence the corresponding volume. The surface charges can count the surface tension until the equilibrium state is reached and hence the stability.

Nanobubbles have been used as templates to form hollow gold nanoparticles [67] and core-shell nanoparticles [68]. It has been shown that, next to the tremendous scientific interest attracted by nanobubbles, they have also a great potential for applications such as nanofluidics, ultrasound diagnostics, gaseous drug delivery, etc. For a comprehensive review on nanobubbles, see ref. [144-154].

Gold suspensions are prepared by using an excess of borohydride to reduce the gold ions. The reaction takes place with the formation of gold nanoparticles and a large amount of gaseous hydrogen. The effect of the borohydride concentration (the bubbles volume density) on both the stability and the resonance wavelength of the Au-LRPR band is the main point to be addressed in the first section of the current chapter. The physical mechanism of nanobubble-induced nanoindent formation is discussed in details in terms of the surface tension. In subsequent sections, the DDA is employed to find out which relative composition of the surrounding environment of the gold nanoparticles would better correspond to the observed LSPR band. Since the nanobubbles are indeed part of the direct environment of gold nanoparticles, it should be taken into consideration to have a good agreement between the simulated and experimental position of the band.

6.1 Experimental details

6.1.1 Material and methods

Gelatin from cold water fish skin was purchased from Sigma-Aldrich, sodium borohydride (NaBH_4) from Fluka and gold salt ($\text{HAuCl}_4 \cdot 3\text{H}_2\text{O}$) from Alfa Aesar. All chemical were used without any further purification. The UV-Vis absorption spectra were measured by using Perkin-Elmer (model lambda 650) spectrophotometer. The morphology/topography analyses were carried out on Atomic Force Microscopy (AFM) Model NSCRIPTOTM DPN system DS006 (Nano INK). The AFM imaging were done by using a silicon cantilever of rectangular shape with a tip radius <10 nm and stiffness of 52-75 N/ m. The resonance frequency of the cantilever in air is 200-400 KHz.

6.1.2 Preparation of the gold nanoparticles-embedded gelatin

The aqueous gelatin solution is prepared by dissolving 150 mg of gelatin in 50 ml of DI water under stirring and heating to 50 °C. After the dissolution, the gelatin solution is cooled down to the room temperature in the ambient air. An appropriate amount of gold chloride is dissolved separately in water and added to the freshly prepared gelatin solution under stirring at room temperature. Finally, a solution of sodium borohydride is added drop by drop to the

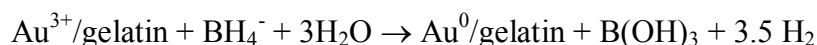
mixture, before bringing the final volume to 75 ml. The solution was then stirred for 15 min at room temperature and casted on a pre-cleaned glass substrate. Experiments have been performed by using a molar ratio of 12.5 of sodium borohydride to gold salt. The film was left for approximately one day to dry in the atmosphere.

6.2 Results and discussion

6.2.1 Optical properties of gold-gelatin nanocomposite and the formation of trapped hydrogen bubbles

The gold-gelatin nanocomposite is prepared by using the gelatin to stabilize the gold particles. The borohydride is used to reduce the gold salt in the presence of the gelatin solution. After adding the borohydride, the color of the mixture turned immediately to red wine, indicating the formation of the gold suspension. At the same time, a large amount of foam (hydrogen bubbles) was observed above the colloidal solution as shown in Figure 34.a. The inset in Figure 34.a shows a thin film of gold nanocomposite casted on a glass substrate. The interfacial bubbles are clear on the hydrophilic surface, the large bubbles are formed due to the aggregation/coalescent process of the smaller surface bubbles.

The interaction between the gold-gelatin solution and the borohydride is illustrated in the following equation [146]



The gelatin mainly is made from both essential and non essential amino acids. It is a good source of tyrosine, methionine and lysine. These amino acids are strong electron donor for the reduction process of the gold anion. Figure 34.b shows typical absorption spectra of freshly prepared gold-gelatin nanocomposite in both solution and film. The resonance wavelength of Au-LSPR band is found at 510 nm in the solution and at 522 nm in the film. In the former measured spectrum, the position of the band corresponds to small nanoparticles with a diameter inferior to 10 nm [13,94,147]. However, the presence of bubbles surrounding the gold nanoparticles may influence significantly the position of the band, that is, the nanoparticles may be larger than the size predicted from spectral data in aqueous solution.

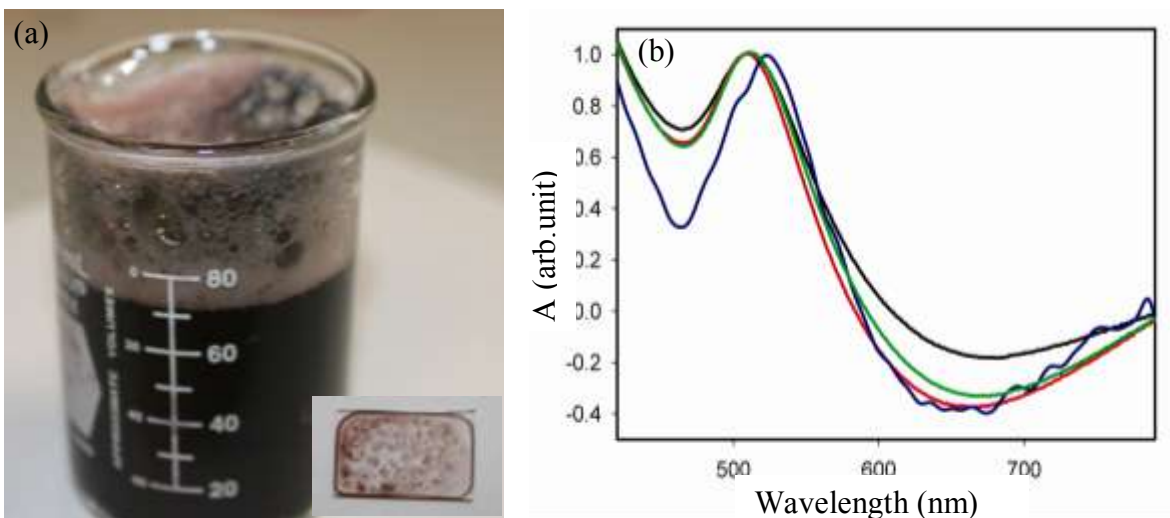


Figure 34: (a) Suspension of the Au-gelatin nanocomposite with hydrogen bubbles. The inset shows the nanocomposite film on a glass substrate. (b) UV-Vis absorption spectrum of gold-gelatin nanocomposite, (black curve: measured in solution directly after synthesis, red curve: in solution, one month from the synthesis; green curve: solution, 2 months from the synthesis; blue curve: film on glass).

The gold particles in the nanocomposite show an excellent stability against aggregation which can be inferred from no change in the resonance frequency of the Au-LSPR band in two months. The high stability of the nanocomposite is accounted of by the stabilizing effect from the gelatin. The positive charged gelatin functional group ($-NH_2$) balance the negative surface charges of gold particles and form gelatin-coated gold particles. As well as, the hydrogen bubbles have strong effect on the gold nanoparticles stability. They act as isolating agent, however, at this stage; it is difficult to discriminate between the two effects. The Au-LSPR band in film is red shifted as compared to the one measured in solution. The deposition of the gold nanocomposite on the glass substrate disturbs the distribution of the surface electron density. That results in non uniform electric field across the film and hence decreases the resonance frequency.

6.2.2 Morphological features of the gold – gelatin nanocomposite film with hydrogen bubble inclusions

Gold-gelatin films were casted from the solution on pre-cleaned glass substrates and left for 1 day to dry in the ambient air. Optical microscopy is not suitable technique to observe the morphology of the small bubbles especially when their size is less than the diffraction limit. The direct evidence of the nanobubbles existence at the water-repellent surfaces comes from the employment of the AFM in tapping mode. On the other hand, the use of the AFM in the contact mode is not the effective methods to identify the bubbles and their surface topography because of the high contact force. That will probably destroy or displace the bubbles. Some results are reported by using AFM in low contact mode, the images were low in quality and the discrimination between the real bubbles and the surface contaminations was very difficult. The use of the AFM in the tapping modes adds more advantages such as the discrimination between the surface properties of the deposited object and the bare substrate. This ability is represented by the phase image which is sensitive to the viscosity, the adhesion forces and the surface contrast. Therefore, the tapping mode is the most reliable AFM modes to characterize the interfacial gaseous structures.

Well-separated hydrogen bubbles traces of nanometre size (300-400 nm) were produced on a flat glass surfaces as shown in Figure 35. The bubbles form as a gas state on the boundary between aqueous solution (in our case, the gelatine solution) and gas phase (hydrogen). The bubbles' traces and gold nanoparticles are both distributed non uniformly and the gelatin patches are connected to each other, resulting in micronized structures. Figure 35 shows gelatin patches, mostly of circular shapes, with inclusions of bubbles and only a small number of gold nanoparticles. As well, the image shows that the formed gold nanoparticles are dispersed and embedded in the gelatin template. It seems that as the film was being dried at the room temperature, the gold nanoparticles are self-assembled in the polymer matrix instead of forming an isolated clusters.

In that selected area, the nanobubbles are not stable and they were dissolved because of their high internal pressure as compared to the atmospheric pressure. According to Laplace equation, the internal pressure is inversely proportional to their diameter. A bubble of size of 100

nm would have an internal pressure of 28 atm, it could be not in thermodynamic equilibrium with the atmosphere as it shown in AFM image. Due to their delicate ephemeral nature, the applied oscillation amplitude to the vibrated cantilever may cause the tip to break in the bubbles.

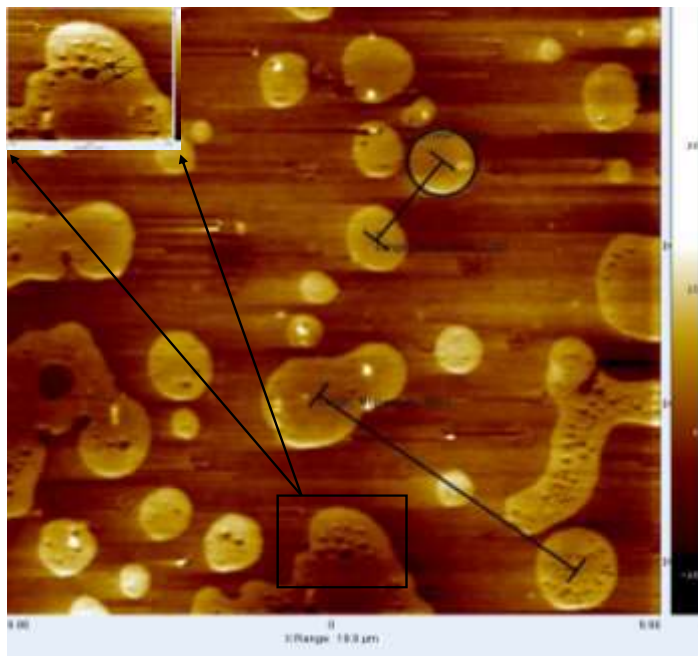


Figure 35: AFM image of gold–gelatin nanocomposite film on a glass substrate shows the embedded gold nanoparticles (white dots) in the gelatine matrix. The inset shows the bubbles trapped inside a gelatin patch.

Figure 36.a shows hemispherical shape microbubbles of non uniform circular cross-section and they are more or less distributed around one peak (narrow size distribution). The line scan profile of a selected bubble shows the spherical cap morphology as shown in Figure 36.c. The microbubbles shown in Figure 36 are well-separated with a good surface coverage. Although, the bubbles are dissimilar in size, they are in thermodynamic equilibrium with the surrounding environment. The size distribution is mainly dominated from the bubbles of the moderate size and the corresponding surface density around $5.12 \times 10^4 \text{ mm}^{-2}$. The Root-Mean-Square (RMS) roughness of the bare glass substrate measured by AFM is about few nanometres, while the measured value after the deposition of the nanocomposite film on glass is about 19.8 nm.

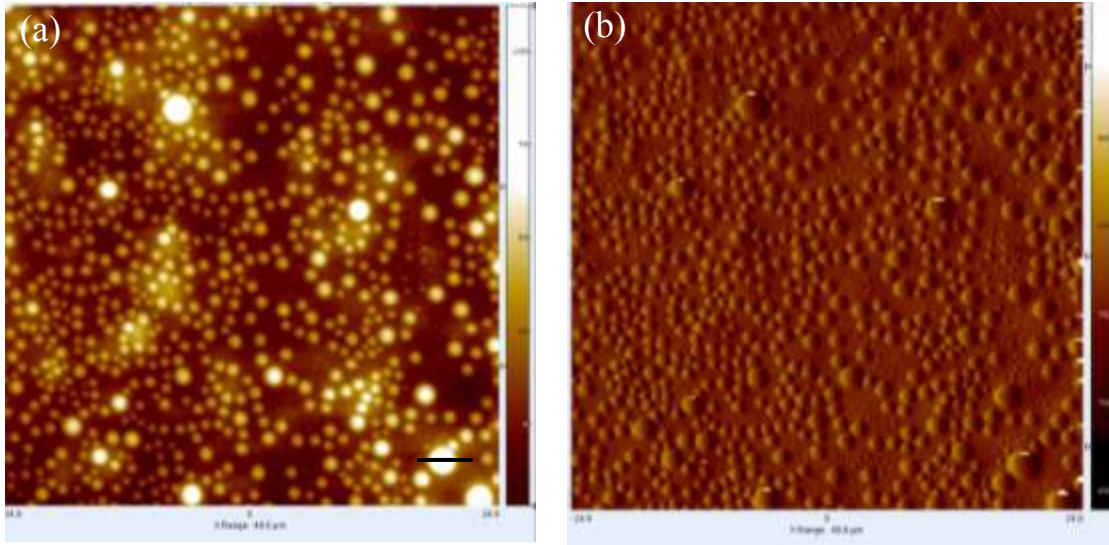
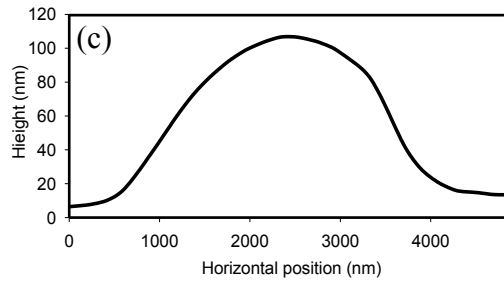


Figure 36: AFM-height image (a) of well distributed bubbles and the corresponding phase image (b). (c) Line scan profile across the bubble marked by a segment in figure a.



The significantly increase in the surface roughness is attributed to the formation of high topographic domains (microbubbles). Y.Wang et al [140] measured the RMS roughness for the polystyrene coated silicon waver (underlying substrate) in both air and water, and they were 0.22 nm 1.3 nm, respectively. The insignificant increase in the roughness can be inferred for the generation of soft surface topographic features (nanobubbles). In this experimental observations, the bubbles sizes were roughly distributed around two peaks (100nm and 50 nm), and the corresponding bubbles surface densities were around $0.632 \times 10^8 \text{ mm}^{-2}$ and $2 \times 10^8 \text{ mm}^{-2}$, respectively. The difference in the underlying substrate and hence the surface roughness between the glass and the polystyrene substrate explains the diversity in the bubbles surface populations and their size distributions. Therefore, the formed bubbles on rough surface are larger in size and less densely populated as compared to those formed on smother surface [148].

The phenomenon of the bubbles integration on pin-free surface proves their presence, softness and mobility to form larger domains. The coalescence phenomenon of the bubbles on ultra-smooth surface has been reported by many research groups [148-150]. The tapping force was used to dislocate the bubbles and the degree of coalescence is controlled by the tapping amplitude. In the case of the roughness surface, it is thought that the surface asperities cause the generation of what called bubbles formation sites (cavities). Due to unfavourable water droplets penetration to those sites which results in formation gaseous structures. In our case, the tapping force is kept constant during all the measurement. The existence of the larger bubbles as shown in Figure 36 can be explained as a natural coalescence of the neighbouring bubbles of moderate size while the bubbles of very small size would dissolve in the bulk material.

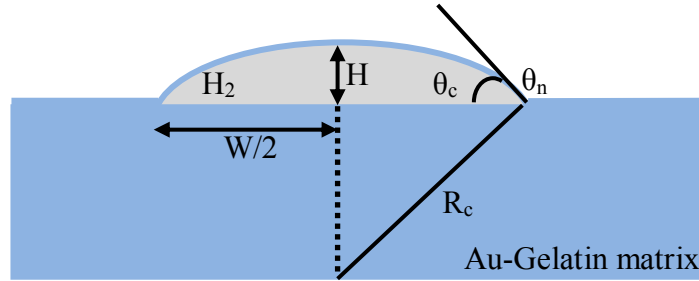


Figure 37: Schematic representation of a bubble formed on the Au-gelatin film.

For more quantitative analysis of the structural parameters (the size and the height distributions) of the surface bubbles, Figure 37 shows a schematic representation of the geometry of a spherical cap bubble. The geometrical cross-section of the bubbles is represented by the Height (H) and the Width (w). The corresponding radius of curvature (R_c) of spherical caped bubbles is defined in terms of both H and W through

$$R_c = \frac{(W/2)^2 + H^2}{2H}$$

The contact angle (θ_c) is given by

$$\theta_c = \sin^{-1}[W/2R_c]$$

The bubbles appear in the AFM-topography image is analyzed by using the free grain analysis software for scanning probe microscopy images (Gwyddion, version 2.20). The software is used to find the width and the height distribution of the bubbles. The height is defined as the difference between the maximums and the minimum AFM-tip vertical displacement. While, the width parameters is the diameter of the circular base of the bubbles. Figure 38 shows the histograms of both the bubbles width and height. A total of around 700 bubbles were detected and the histograms are fitted with a Gaussian distribution function with a corresponding mean value $\langle H \rangle = 60$ nm and $\langle W/2 \rangle = 400$ nm. The mean value of the both R_c and θ_c are calculated to be 1363 nm and 17° , respectively. The extracted structural parameters show a high aspect ratio (width/height) which reflects the flat-like plat structure of the observed bubbles. Ishida et al [151] measured the contact angle of the formed bubbles on the hydrophobic surface (silicon wafer hydrophobized with octadecyltrichlorosilane) in water. He found that θ_c is within the range of 10° to 30° .

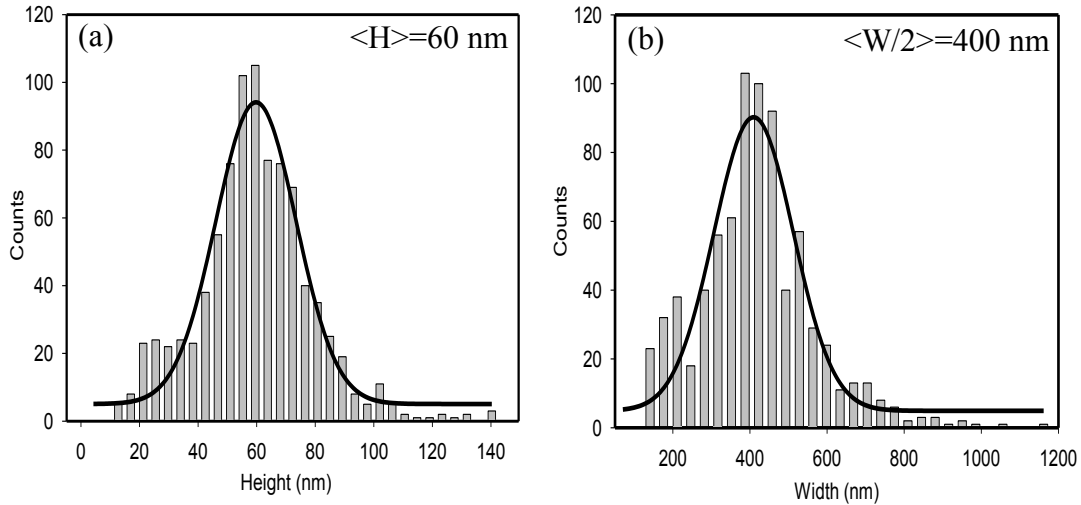


Figure 38: Histogram of (a) bubbles height and (b) Width.

Due to the effect of the AFM tip convolution, the height and width could be imprecisely estimated. Song et al [152] discussed the influence of the tip's size (R_{tip}) on the actual estimation of the bubbles width, assuming that the apparent bubble height truly represents the measured one. For the bubbles with $R_c > H$, the nanoscopic contact angle ($\theta_n = 180^\circ - \theta_c$) is greater than 90° , the measured AFM image is acquired by using the tip apex and the effect of its wall on the imaging process is insignificant. For the other case, where the $\theta_n < 90^\circ$, the tip's side walls is also

interacted with the bubbles surface which add another systematic error to R_c measurement and hence the H . Therefore, in both cases, the measured (apparent) value of both R_c and H should be modified to include the tip radius effect. Anyhow, the second case is not applicable here because of the plat-like surface bubbles ($\langle\theta_n\rangle = 163^\circ$). In all cases, in the current observations, the tip size (<10 nm) is considered negligible as compared to the estimated R_c ($=1343$ nm). Therefore, no further correction of the R_c and the height is required.

6.2.3 Stability mechanism of the bubbles

The classical thermodynamic theory ensures that the bubbles are not stable and they should decay and dissolve in time scale of milliseconds. Based on experimental observation, once the bubbles are formed, they are stable for hours and even for days. Now, the question is why the bubbles' lifetime predicated by the thermodynamics is much shorter than the experimental observed time?

Understanding the mechanical stability of the surface bubbles starts with a deep look into the equilibrium contact angle (θ_c). The equilibrium angle is measured at the gas-liquid interface to the solid substrate and it is evaluated when the free energy at the three phase line is minimum. The surface tension is affected by the smoothness and the heterogeneity of the solid substrate and hence affects the measured θ_c . The value of θ_c falls between the upper value (the advancing angle) and the lower value (the receding angle).

The macroscopic water drop (another name to angle θ_c) on a glass substrate is measured experimentally by using a goniometer. The θ_c value is reported to be close to 51° which is larger than the calculated one ($=17^\circ$). The discrepancy between the observed value and macroscopic calculation of θ_c gives a deep insight into the possible stability mechanisms for the bubbles at the micro- and nano-metric scale.

Many theoretical approaches have been proposed to explain the mechanical stability of the bubbles. The influence of the bubble contact angle on the bubble size and hence the surface-bubble contact radius is believed to affect their stability mechanism. Two concepts have been

suggested to explain their stability. The first concept is the line tension along the base of the bubble [153], which has been suggested as a special theoretical treatment for a spherical capped bubble formed on smooth and isotropic solid surface. But in reality, this ideal surface doesn't exist and the line tension theory should be extended to include the surface heterogeneity of the underlying substrate. The concept of the pseudo line tension [153] comes into play to include the effect of the surface roughness and heterogeneity on the bubbles stability. The deviation between the measured and the calculated bubbles contact angle is might be attributed to both line tension and pseudo line tension depending on the bubble size. It is believed that discrepancy results in increase the value of R_c . The latter decreases the inside pressure and hence increase the lifetime of the bubbles. In despite of, the difference in pressure stills high for their long time stability, some other factors should be included to understand the constancy method.

As the gas flow out of the bubble due to the enormous internal pressure, the bubbles will collapse and dissolve in a very short time. If there is an equal inward gas flow from the three-phase contact line, the bubbles remain intact because of the zero gas exchange rates. Such a dynamic equilibrium has been suggested by Brenner et al [154] to demonstrate the stability of the surface bubbles on the hydrophobic surface. According to the second law of the classical thermodynamic theory, the proposed stability mechanism is metastable state. That implies that equilibrium state is transitional and the bubbles dissolution will be finally reached. Brenner et al could not explain the origin of the driving force for the gas exchange process. On the other hand, the formation of stable surface bubbles on hydrophilic surface like mica and glass has been observed [155]. On such surface there is no inward gas flux at the contact line due to the absent of the density depletion layer. Therefore, according to their model, the bubbles are not stable. In our case, this model is not adequate because a glass substrate has been used as an underlying surface.

Ducker et el suggested that the contaminations in the water may be responsible for the bubbles stability. The presence of the contaminant molecules reduce the surface tension and increase the contact angle measured at the gas phase and hence increase the stability lifetime. The improper preparing of the solid surface, the insoluble organic contaminants in the solvents and air are the potential sources for the contaminations. The contaminations could occur during

mixing the solvent (e.g as in the solvent exchange process) or the imaging process in the AFM liquid cell, the latter adds one more source of the contaminations.

Another theoretical treatment suggested that the equilibrium steady state originates from the adsorbed counter-ion layer on the bubbles surface [156]. The effect of the surface charges is to count for the high surface tension. The repulsion force between like surface charges at the air interface increase bubbles curvature and hence they tend to increase the bubbles diameter. While, the repulsion force stretches out the surface, the surface tension acts in the opposite way. The moment, the two forces are balanced, the equilibrium state is achieved. As the electrostatic forces decrease inversely with the square of the charges separation, the adsorbed charges strongly tend to decrease the outward pressure as the bubbles expand according to Laplace equation. Presumably, the more the bubbles are charged, the more they are stable against aggregation.

In summary, there is no adopted theory the small bubbles stability and the stability mechanism is still in question. In our case, the situation is somehow different and more complicated because of the chemical formation of the bubbles. We believe that many mechanisms contribute partially to the bubbles stability. The presence of the stabilizing agent (e.g the polymer matrix in our case) might be able to increase lifetime stability.

6.2.4 Formation of nanoindents

It seems that the formation of the surface bubbles experienced different conditions which result in distinguished morphologies. Perfectly identical spherical bubbles with smooth profile are observed, those domains are surrounded by circular rim as shown in Figure 39. This kind of structure have been observed on ultrathin polystyrene films in water and they were called “nanoindented structures” [140].

For in detail explanation on how the bubbles can induce the formation of indents on the gold nanocomposite film, a schematic representation of spherically capped bubble on film surface and the relevant forces act at the three phase line, is illustrated in Figure 40. The

nanoindentations are induced by the bubbles under the condition of imbalanced relative forces. Through the evolution of the bubbles, two main forces control the size and the stability of the bubbles.

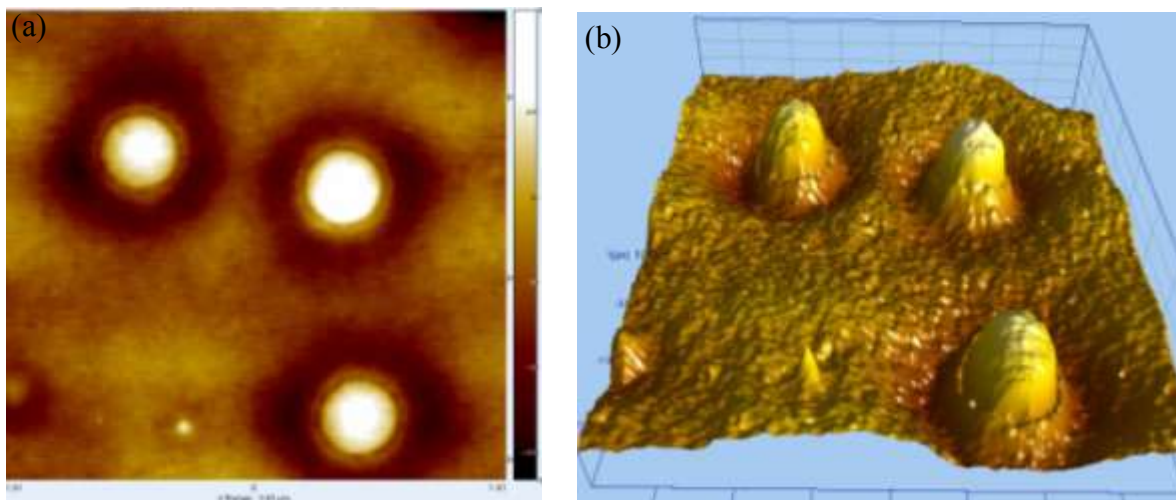


Figure 39: (A) 2D AFM topography image of nanoindentations, (b) the corresponding 3D image.

The forces are the surface tension (F_{st}) and the Laplace pressure (P). The former force is cohesive in nature and acts tangentially along the three-phase contact line. The tension force can be analyzed into two components, the perpendicular force (F_{\perp}) and the other one acts horizontally (F_{\parallel}), as shown in Figure 40. The latter component affects the surface extension of the bubble and cooperatively works with the internal pressure to control the height of the bubble. In general, both components affect the bubble stability.

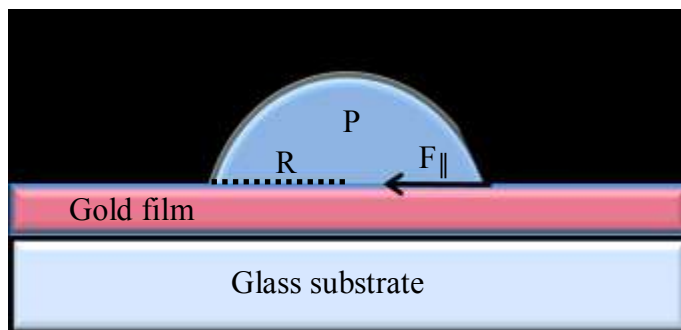


Figure 40: Schematic representation of a bubble formed on the Au-gelatin film.

The Laplace pressure is order of magnitude higher than the atmospheric pressure; make the bubbles in non equilibrium state with the surrounding environment. The high inside pressure pushes the polymer out to form the rib around the bubbles. During the diffusion process of the hydrogen gas at the air-gold film interface, the weak interaction between the polymer molecules enhances the mobility of the polymer chains. As a results of the reduced entanglement in the matrix, the polymer chains move toward the interface due to both the high pressure and the perpendicular component of the surface tension.

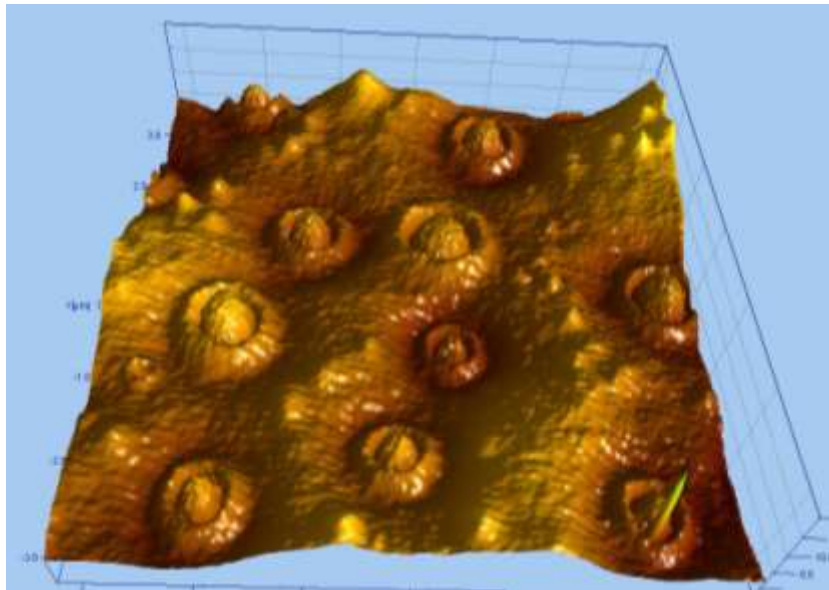


Figure 41: 3D AFM-height image of stable nanoindentations.

The formation of the circular rib around the bubbles affects their size and it appears that the bubbles shrink. For the bubbles appear in Figure 40, the rim is still attached to the outer surface of the bubbles and it appears less in height as compared to the bubbles height. The presence of the rib adds more inward horizontal pressure and hence the bubbles size is reduced. That increases the gas outflow and increase polymer chains motion outward the interface and hence increase the rib size. In this case, the rib appears higher than the confined bubble as shown in Figure 41, which results in well-separated rim structure. The presence of the rib decreases the bubbles surface area and hence the internal pressure is increased. Because of imbalance net force in smaller bubbles, that probably causes explosion and forming hollow indents as seen in Figure

42. While, the high surface tension of the larger bubble encounter for the inside pressure and hence the equilibrium condition is achieved.

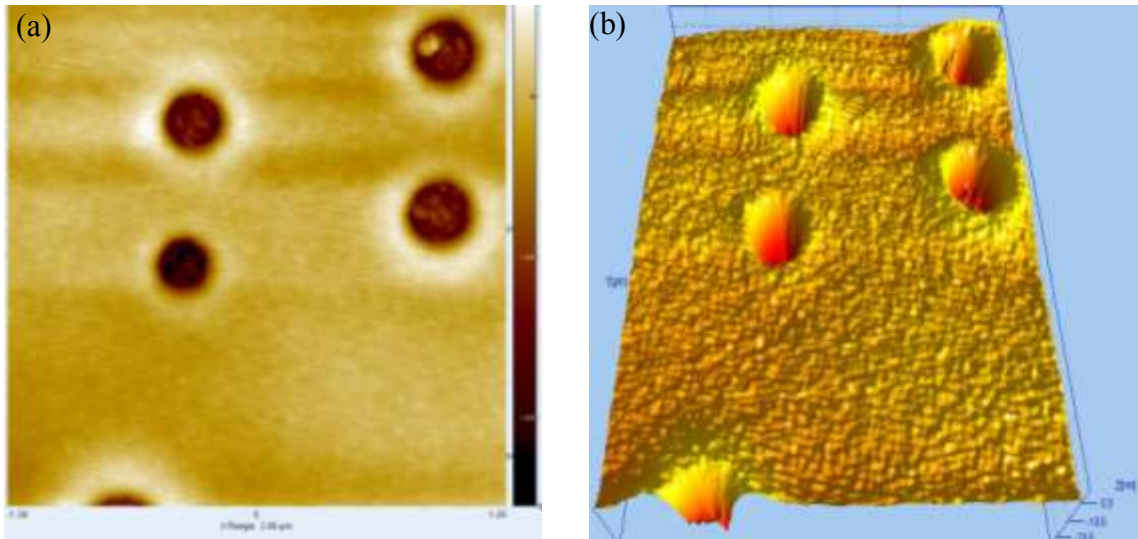
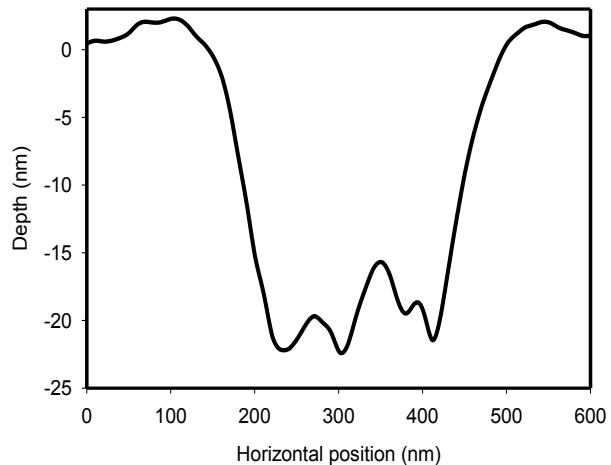


Figure 42 : AFM images of the traces of nanobubbles (a) that left the surface of the film (dark holes in the 2D image) and the corresponding 3D image (b).(c) 1D scan profile across the hole marked by a segment in the height image.



6.2.5 Influence of the bubbles on the gold particles stability

The instable/stable bubbles and the presence of the surface hollow indents add a remarkable change in the surface topography of the nanocomposite film especially regarding the gold particles stability. It sounds that the some bubbles have pressed out in many places, probably during the drying process. That suggests that bubbles have formed inside the thin films during the diffusion of the hydrogen gas. On the other hand, some of them are still stable and trapped under the surface of the film. Those stable bubbles somehow are formed deeper inside

the film and had not the time to reach the surface and explode, before the film dried, as shown in Figure 43. As well, the image shows a unique intermixing between the craters and the gold nanoparticles. Even such traces contain few aggregated gold particles; the presence of the gold particles in the middle of the circular craters provides a distinguished method to preserve the particle for long period of time. In this case, the formation of the empty indents on surface of gelatin becomes a kind of receptacle for nanoparticles.

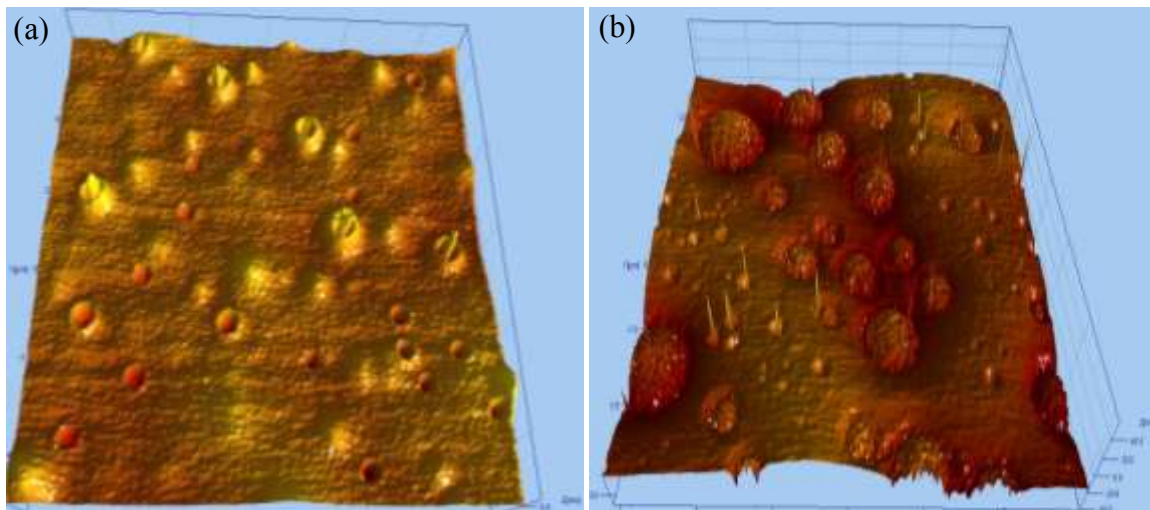


Figure 43: 3D AFM-height image, the scan size is 10.2 and 6.2 micron for image a and b respectively, Gold nanoparticles appear sparks in the images.

The Figure 43.b shows the entrapment of single nanoparticles of size around 50 nm inside the craters. We believe that the bubbles, in their way to the surface, draw the nanoparticles and carry them along. By controlling the diffusion of the bubbles, it becomes possible to carry and deposit nanoparticles at well-defined places, that is, to pattern the surface of the film. As it can be seen in the Figure 43, some of the traces are empty, meaning that the bubbles left the film without meeting nanoparticles. The size of the bubbles in this image are around 150 nm compared to around 300 nm to the ones shown in Figure 43.a. It sounds that the size of the craters controls to some extent the number of the entrapped gold particle.

6.2.6 Simulation of the optical properties of gold – gelatin nanocomposite films with hydrogen bubble inclusions using DDA

DDA is employed to model the absorption spectrum of the Au-LSPR band and then compared to the observed one in the gelatin aqueous solution. In all the simulations, the inter-dipole separation was kept constant at around 1 nm, giving a total of 34000 dipoles per target.

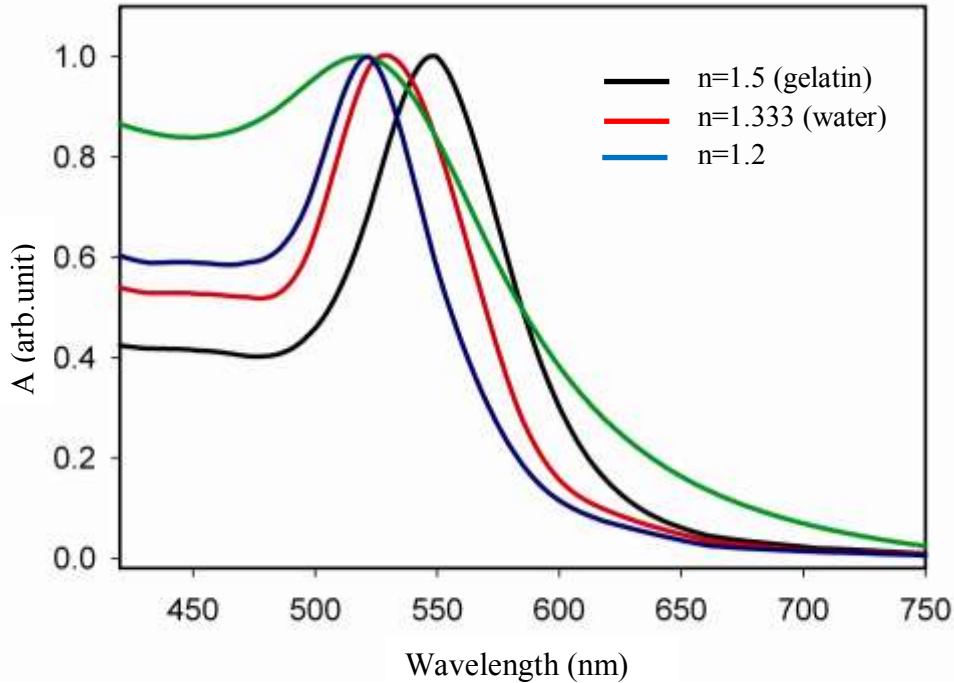


Figure 44: DDA simulation of the optical properties of gold nanoparticles of size of 50 nm embedded in gelatin. The green curve shows the experimental band (520 nm) and the others show the position of the bands by assuming different refractive indices to simulate the environment.

Figure 44 shows the position of the Au-LSPR band assuming several values for the refractive index of the environment surrounding the gold nanoparticles. When the gelatin ($n = 1.5$) and the water ($n = 1.33$) are considered separately, do not correspond to the real host material. The calculated plasmonic band appears to be red shifted compared to the observed band. The hydrogen bubbles present in the real environment lower the effective refractive index and, for

this reason, the best agreement with the experimental spectrum is found by assuming a hypothetical value ($n=1.2$) which is lower than both that of gelatin and water.

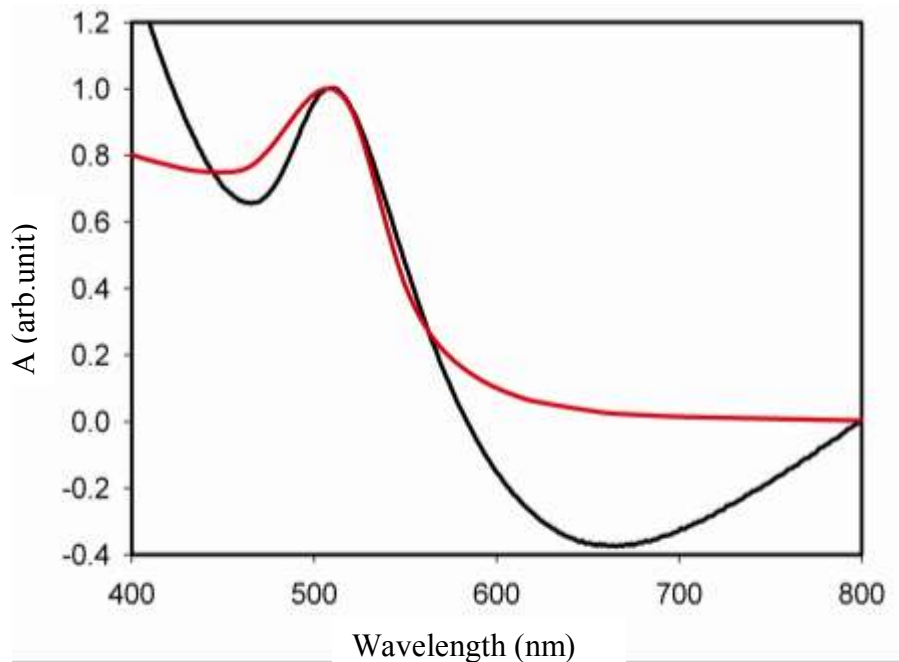


Figure 45: DDA simulation of the position of the Au LSPR band (black curve) by assuming $n = 1$ (air); red curve: experimental spectrum (510 nm).

The experimental Au-LSPR band measured in solution which corresponds to a nanocomposite prepared with a large excess of sodium borohydride, which is of hydrogen nanobubbles is illustrated in Figure 45. By lowering even more the refractive index of the environment and assuming that the gold nanoparticles would be surrounded by air, a good agreement between the simulated and experimental positions of the band is found. From this result it can be inferred that, in the nanocomposite film, there is a large amount of nanobubbles surrounding the gold nanoparticles.

6.3 Conclusions

Gold–gelatin nanocomposites have been prepared by using sodium borohydride as a reducing agent. The reduction process yields to formation of the gold nanoparticles with a large amount of hydrogen bubbles. The geometry of the bubbles is mainly represented by hemispherical shapes. Different morphologies are also found such as holes (pores or exploded bubbles) and indentic structures. The bubbles are entrapped in the polymer films during the drying process of the nanocomposite material and they form stable interfacial gas domains. The cone-shaped gelatin features provoked by the raising bubbles may be interesting in the future for patterning applications. On the other hand, some bubbles are formed very close to the sample surface and they are exploded after the film is dried. The traces left behind the exploded bubbles become receptacles, convenient to hold the gold nanoparticles carried by the bubbles on their way to the surface of the drying film. To some extent, the size of the traces controls the number of the entrapped gold particles. Small traces contain one nanoparticle while larger cavities may have 2–3 or more nanoparticles. The presence of the gold particles in the middle of the circular craters provides a distinguished method to preserve the particle for long period of time against the natural process of aggregation. Other interesting applications of this system may be for micro- and nanofluidics and drug release may also be possible. However, more work is necessary to better control the reaction in order to synthesize a nanocomposite for a specific application. It is thought that a microfluidic environment would be advantageous for this purpose.

Interestingly, DDA simulation of the optical properties points to the gaseous bubbles as being the major part of the nanoparticles' environment when a large excess of sodium borohydride is used for the synthesis, that is, a large amount of hydrogen is formed.

CHAPTER SEVEN

Conclusions

7.1 Modeling the optical properties of metallic nanoparticles

7.1.1 Spherical nanoparticles arranged in planar arrays

The extinction spectrum of metallic nanoparticles has contributions from both the absorption and the scattering properties. For nanoparticles smaller in size (few tens of nanometers), the absorption cross-section is mainly contributed to the extinction one. The scattering properties become dominant as the particle size increases.

Due to the uniform distribution of the polarization charges over the surface of isotropic particles, their extinction spectra show the excitation of single PM. The spectral characteristics of spherical particles may exhibit both LM and TM as they are brought in contact. The plasmonic coupling between the interacting particles distributes the negative clouds non uniformly over the cluster surface and hence increases the anisotropy in their optical response.

The DDA is employed to model the absorption efficiency for silver and gold nanoparticles arranged in monolayer 2D arrays of different sizes. The size of the array is controlled by the number of nanospheres used to generate the target. The results of the simulations show that the optical response for both metals (silver and gold) is size dependent such that the amplitude of the LSPR band increases with the size. The band position of both silver particle modes is shifted toward each other as the target size decreases and they overlap when the smallest array is considered. In the case of gold nanoparticles, the resonance wavelengths of both longitudinal and transverse band are very close, resulting in excitation of a single band. Both plasmon modes can be distinguished at the extremes of the incident angle.

7.1.2 Single oriented nanoparticles of different shapes (multi-fold symmetry)

The optical properties of three selected anisotropic particles (nanocube, nanobar and nanoellipsoid) have been modeled by the DDA methods. These particle shapes are among the most interesting shapes due to many observed PMs in the visible region. The result of simulation show the possibility of excitation of simultaneous PMs. Different dipolar PMs have been observed under illumination of p-type light and at specific incident angles. The observation of this unique optical response is also dependent on the type of metallic nanostructures. For example, the nanocube has several symmetry axes, thus it is expected that the absorption spectrum exhibits several plasmonic bands. It seems, however, that the band positions of gold nanocube modes are very close to each other making them indistinguishable, resulting in the excitation of a single broadened band. In the case of silver nanocube, the plasmonic bands which correspond to the multifold symmetry are well separated, resulting in the excitation of more than a single band. The excitation of the Ag-LSPR modes always occurs at higher energy as compared with the ones calculated for the gold particle. In general, the distribution of the polarization on the corner of the nanocube increases the separation between the negative/positive charges, leading to a red shift in the band position of the LSPR mode as compared to a spherical particle of the same size.

The number of excited PM is related to the number of symmetry axes. The geometrical parameters of nanobar are mainly represented by two main axes. The absorption spectra of an oriented nanobar exhibit two PMs. Due to the oscillations of the polarization charges parallel and perpendicular to the main axis of the nanobar, both TM and LM are observed. Due to non-uniform cross-sectional area of the ellipsoidal particle, its structure is characterized by three main axes. The optical response of the metallic ellipsoidal nanoparticle is quite specific when compared to other nanoparticle morphologies due to the possibility of three different LSPR modes (one LM and two TMs). These modes are associated with the electronic fluctuations along each symmetry principal axis. The possibility of observing distinct plasmonic bands depends on the orientation of the particles in both the lab and the target frames.

The band position of the excited PM is controlled by the length distribution of the symmetry axis and hence the separation of the opposite charges. The band position of the PMs depends linearly on the axis length in both metals (gold and silver). Increase in the axis length results in a red shift of the PM band position. The Au-PMs are relatively more broadened when compared to the ones found for silver nanoparticles. For both metals, the LM shows a stronger dependency on the length distribution of the axis as compared to the TMs.

The calculations done in this thesis have contributed to a better understanding of plasmon resonance modes that can be observed in actual experimental particles, particularly regarding conditions in which the modes can be produced. These particle optical properties, among other things, are strongly dependent on their size as well as their shape.

7.2 Effect of the host material on the optical properties of gold nanoparticles

7.2.1 Gold-Poly(methyl methacrylate) nanocomposite material

Au-PMMA nanocomposites have been prepared by using three different photochemical methods (UV exposure, microwave irradiation and thermal reduction) specifically, for sensing applications. The synthesis was carried out by irradiation of a spin-coated film containing a mixture of gold precursor (HAuCl_4) and poly(methyl methacrylate) dissolved in acetone. It is found that the microwave-synthesized composite showed a uniform distribution of spherical nanoparticles, while a large number of triangular particles can be seen as a result of UV irradiation. The sensitivity of the band position of Au-LSPR toward the refractive index of the surrounding material has been tested for non-annealed samples and then compared to that of annealed ones. For both annealed and non-annealed samples, the resonance wavelength is linearly shifted with the refractive index of the dielectric medium. As-prepared nanocomposites lacked sensitivity toward the surrounding environment. Annealing at 300 °C, temperature well above the glass transition temperature, brought about an important change in the structure and properties of the nanocomposite. It is inferred that in the rubbery state of the nanocomposite, the interactions between the gold and the polymer chains are weakened and, at the same time, the mobility of gold nanoparticles is augmented. The results show that, in the annealed samples, the surface density of gold nanoparticles is highly increased. Under these conditions, the

nanocomposites show an enhanced sensitivity toward the surrounding molecules. The results also indicate that, by using an adequate post-synthesis heat treatment, gold-polymer nanocomposites can be successfully used as sensing platforms.

7.2.2 Gold-gelatin nanocomposite material

Gold-gelatin nanocomposites were prepared by using sodium borohydride as a reducing agent. The reduction process of the gold salt is combined with the generation of a large amount of hydrogen bubbles. The presence of bubbles in the film engenders a number of interesting optical properties and morphological features that are useful for future applications. For example, the large traces left behind by the exploding bubbles are thought to become receptacles, convenient to hold the gold nanoparticles carried by the bubbles on their way to the surface of the drying film. Also, the cone-shaped gelatin features provoked by the raising bubbles may be interesting in the future for patterning applications. Application of this system for micro- and nanofluidics and drug release is also possible. However, more work is necessary to better control the reaction in order to synthesize a nanocomposite for a specific application. It is thought that a microfluidic environment would be advantageous for this purpose. Interestingly, DDA simulation of the optical properties points to the gaseous bubbles as being the major part of the nanoparticles' environment when a large excess of sodium borohydride is used for the synthesis. The results of this work are highly relevant to the new and exciting field of micro- and nanobubbles at surfaces and interfaces of films.

7.3 Future perspectives

We have studied the optical properties of gold and silver nanoparticles both theoretically and experimentally. The initial simulations given here are considered as a critical step for tuning the LSPR modes of both isolated and assembled nanostructures. Technical applications of metal nanoparticles normally require incorporating an assembly of these nanostructures of different size and shape distributions with a good control over the inter-particle separation. Thus understanding the optical behavior of an isolated nanoparticle and the effect of the coupling between the LSPR of nearby particles is needed. More work is required to study the optical

properties of multi-fold symmetry particles arranged in both 2D and 3D arrays on specific substrates. The systematic variation in geometrical parameters, orientation and inter-particle coupling will be useful for designing/ minimizing the active plasmonic device for optical components in nanoscale devices in specific applications of nanophotonic and nanomedical applications.

Based on the anisotropic optical features (e.g. several hot spots and absorbance of the incident light at different wavelengths in the UV-Vis region) of many-fold symmetry particles, it will also be of great interest to incorporate these structures in

- 1- Surface-Enhanced Raman Scattering (SERS) systems to improve the detection and characterization capabilities down to single-molecule level.
- 2- Plasmonic solar cells to examine their ability to increase the photoelectron generation and hence the energy conversion efficiency. In this context, light trapping using particles of various shapes and concentrations is of particular interest.

Simultaneous excitation of several PMs might be useful in bio-sensing applications. Using anisotropic nanoparticles for biosensing may add more information about the spatial adsorbances of molecules. This can be monitored by the change of the resonance wavelength along specific symmetry axis.

The experimental work presented here to study the effect of the surrounding material on the optical properties of the metallic nanoparticles can be extended to include different polymers and metallic particles. The diversity of both the nanoparticles and the host material might be useful to prepare a novel material of unique physical, chemical and optical properties. It will be interesting to study the influence of the annealing temperature (above and below the glass transition temperature of the polymer) on the surface particles density and hence on the sensing capabilities of the nanocomposite films.

The optical properties and morphological features in the gold-gelatin nanocomposite material show an inclusion of the stable/unstable surface bubbles in the nanocomposite films.

These interesting surface properties might be useful for patterning applications. However, more work is necessary to better control the reaction in order to synthesize a nanocomposite for these applications. Possible future work is summarized below:

- 1- Controlling the gas diffusion and hence the nucleation rate of surface bubbles. This might be achieved by drying the nanocomposite films at different temperatures.
- 2- Better control of both size and shape distribution of bubbles might be achieved by the synthesis of the nanocomposite materials by using a micro-reactor.
- 3- It has been proved that hydrogen bubbles contribute significantly to the surrounding medium of the nanoparticles. It will be interesting to investigate the effect of bubbles on the shape and size distribution of nanoparticles.

References

- [1]P. Englebienne, A. V. Hoonacker, and M. Verhas, "Surface plasmon resonance: principles, methods and applications in biomedical sciences," *Spectroscopy* **17**, 255-273 (2003).
- [2]R. Schasfoort, and A. Tudos, *Handbook of Surface Plasmon Resonance* (Royal Society of Chemistry, 2008).
- [3]Y. Yao, B. Yi, J. Xiao, and Z. Li, "Surface plasmon resonance biosensors and its application," *IEEE*, 1043-1046 (2007).
- [4]K. A. Willets, and R. P. Van Duyne, "Localized surface plasmon resonance spectroscopy and sensing," *Annual Review of Physical Chemistry* **58**, 267–297 (2007).
- [5]E. Hutter, and J. H. Fendler, "Exploitation surface plasmon resonance," *Adv. Mater* **16**, 19 (2004).
- [6]Y. Xia, and N. J. Halas, "Shape-controlled synthesis and surface plasmonic properties of metallic nanoparticles," *MRS Bulletin* **30**, 338-348 (2005).
- [7]V.-V. Truong, and G. D. Scott, "The optical properties of aggregated noble-metal films", *J. Opt. Soc. Am* **67**, 502-510 (1977).
- [8]V.-V. Truong, and G.D. Scott, "Optical constants of aggregated gold films," *J. Opt. Soc. Am* **66**, 124-131 (1976).
- [9]B. J. Wiley, S. H. Im, Z. Y. Li, J. McLellan, A. Siekkinen, and Y. Xia, "Maneuvering the surface Plasmon resonance of silver nanostructures through shape-controlled synthesis," *J. Phys. Chem. B* **110**, 15666-15675 (2006).

- [10]K.-S Lee, and M. A. El-Sayed, "Gold and silver nanoparticles in sensing and imaging: sensitivity of plasmon response to size, shape, and metal composition," *J. Phys. Chem. B* **110**, 19220-19225 (2006).
- [11]E. Hao, G. C. Schatz, and J. T. Hupp, "Synthesis and optical properties of anisotropic metal nanoparticles," *Journal of Fluorescence* **14**, 331-341 (2004).
- [12]E. S. Kooij, and B. Poelsema, "Shape and size effects in the optical properties of metallic nanorods," *Phys. Chem. Chem. Phys* **28**, 3349-3357 (2006).
- [13]S. Link, and M. A. El-Sayed, "Spectral properties and relaxation dynamics of surface plasmon electronic oscillations in gold and silver nanodots and nanorods," *J. Phys. Chem. B* **103**, 8410-8426 (1999).
- [14]W. S. Prescott, and P. Mulvaney, "Gold nanorod extinction spectra," *J. Appl. Phys* **99**, 123504 (2006).
- [15]G. Bader, A. Haché, and V.-V. Truong, "Anisotropic optical constants of aggregated gold films by reflection and transmission ellipsometry," *Thin Solid Films* **375**, 73-76 (2000).
- [16]G. Bader, P.V. Ashrit, F.E. Girouard, and V.-V. Truong, "P-polarized optical properties of aggregated gold films," *J. Appl. Physics* **68**, 1820-1824 (1990).
- [17]S. Kim, Y. J. Jung, G. H. Gu, J. S. Suh, S. M. Park, and S. Ryu, "Discrete dipole approximation calculations of optical properties of silver nanorod arrays in porous anodic alumina," *J. Phys. Chem. C* **113**, 16321-16328 (2009).
- [18]M. Alsawafta, M. Wahbeh, and V.-V. Truong, "Simulated optical properties of gold nanocubes and nanobars by discrete dipole approximation," *Journal of Nanomaterials*, 283230 (2011).

- [19]M. Alsawafta, M. Wahbeh, and V.-V. Truong, “Plasmonic modes and optical properties of gold and silver ellipsoidal nanoparticles by the discrete dipole approximation,” *Journal of Nanomaterials* , 457968 (2011).
- [20]B. T. Draine, and P. J. Flatau, “Discrete-dipole approximation for periodic targets: theory and tests,” *J. Opt. Soc. Am. A* **11**, 2693-2703 (1994).
- [21]M. J. Collinge, and B. T. Draine, “Discrete-dipole approximation with polarizabilities that account for both finite wavelength and target geometry,” *J. Opt. Soc. Am. A* **21**, 2023-2028 (2004).
- [22]J. J. Goodman, B. T. Draine, and P. J. Flatau, “Application of fast-Fourier-transform techniques to the discrete-dipole approximation,” *Opt. Lett* **16**, 1198-1200 (1991).
- [23]P. W. Barber, and S. Chill, *Light scattering by particles: computational methods* (World Scientific, 1990).
- [24]K. L. Kelly, A. A. Lazarides, and G. C. Schatz, “Computational electromagnetics of metal nanoparticles and nanoparticle aggregates,” *Comput. Sci. Eng* **3**, 67-73 (2001).
- [25]E. J. Zeman, and G. C. Schatz, “An accurate electromagnetic theory study of surface enhancement factors for silver, gold, copper, lithium, sodium, aluminum, gallium, indium, zinc, and cadmium,” *J. Phys. Chem* **91**, 634-643 (1987).
- [26]H. Portalès, N. Pinna, and M.-P. Pileni, “Optical response of ultrafine spherical silver nanoparticles arranged in hexagonal planar arrays studied by the DDA method,” *J. Phys. Chem. A* **113**, 4094-4099 (2009).
- [27]N. Féridj, J. Aubard, and G. Lévi, “Discrete dipole approximation for ultraviolet–visible extinction spectra simulation of silver and gold colloids,” *J. Chem. Phys* **111**, 1195-1207 (1999).

- [28]L. Mulfinger, S. D. Solomon, M. Bahadory, A. V. Jeyarajasingam, S. A. Rutkowsky, and C. Boritz, "Synthesis and study of silver nanoparticles," *J. Chem. Educ* **84**, 322-325 (2007).
- [29]M. Alsawafta, M. Wahbeh, S. K. Misra, and Vo-Van Truong, "The effect of target size on the optical response of ultrafine metallic spherical particles arranged in a two-dimensional array," *Proc. SPIE* **8007**, 80071H-80071H-9 (2011).
- [30]M. Wahbeh, M. Alsawafta, S.K. Misra, and Vo-Van Truong, "Optical properties of two-dimensional and three-dimensional arrays of noble metal nanoparticles by the discrete dipole approximation method," *Proc. SPIE* **8007**, 80071I (2011).
- [31]P. Yang, H. Portalès, and M.-P. Pileni, "Ability to discern the splitting between longitudinal and transverse plasmon resonances in Au compared to Ag nanoparticles in close-packed planar arrays," *Phys. Rev B* **81**, 205405 (2010).
- [32]E. Hao, G. C. Schatz, and J. T. Hupp, "Synthesis and optical properties of anisotropic metal nanoparticles," *Journal of Fluorescence* **14**, 331-341 (2004).
- [33]E. Hao and G. C. Schatz, "Electromagnetic fields around silver nanoparticles and dimers," *J. Chem. Phys* **120**, 357-366 (2004).
- [34]I. O. Sosa, C. Noguez, and R. G. Barrera, "Optical properties of metal nanoparticles with arbitrary shapes," *J. Phys. Chem B* **107**, 6269-6275 (2003).
- [35]J. Zhu, C. Kan, X. Zhu, J.-G. Wan, M. Han, Y. Zhao, B. Wang, and G. Wang, "Synthesis of perfect silver nanocubes by a simple polyol process," *J. Mater. Res* **22**, 1479-1485 (2007).
- [36]B. J. Wiley, Y. Chen, J. M. McLellan, Y. Xiong, Z.-Y Li, D. Ginger, and Y. Xia, "Synthesis and optical properties of silver nanobars and nanorice," *Nano Lett* **7**, 1032-1036 (2007).

- [37]J. Grand, P.-M. Adam, A. S. Grimault A. Vial, M. L. Chapelle, J.-L. Bijeon, S. Kostcheev, and P. Royer, “Optical extinction spectroscopy of oblate, prolate and ellipsoid shaped gold nanoparticles: experiments and theory,” *Plasmonics* **1**, 135-140 (2006).
- [38]H. Chen, Z. Sun, W. Ni, K. C. Woo, H.-Q. Lin, L. Sun, C. Yan, and J. Wang, “Plasmon coupling in clusters composed of two-dimensionally ordered gold nanocubes,” *Small* **5**, 2111-2119 (2009).
- [39]J. N. Anker, W. P. Hall, O. Lyandres, N. C. Shah, J. Zhao, and R. P. Van Duyne, “Biosensing with plasmonic nanosensors,” *Nature Materials* **7**, 442-453 (2008).
- [40]W. J. Galush, S. A. Shelby, M. J. Mulvihill, A. Tao, P. Yang, and J. T. Groves, “A nanocube plasmonic sensor for molecular binding on membrane surfaces,” *Nano Lett* **9**, 2077-2082 (2009).
- [41]V. E. Ferry, M. A. Verschuuren, H. B. T. Li, E. Verhagen, R. J. Walters, R. E. I. Schropp, H. A. Atwater, and A. Polman, “Light trapping in ultrathin plasmonic solar cells,” *Opt. Exp* **18**, 237-245 (2010).
- [42]N. Chandrasekharan and P. Y. Kainat, “Improving the photo-electrochemical performance of nanostructured TiO₂ films by adsorption of gold nanoparticles,” *J. Phys. Chem B* **104**, 10851-10857 (2000).
- [43]B. Nikoobakht, J. Wang, and M. A. El-Sayed, “Surface-enhanced Raman scattering of molecules adsorbed on gold nanorods: off-surface plasmon resonance condition,” *Chem. Phys. Lett* **366**, 17-23 (2002).
- [44]R. F. Aroca, R. A. Alvarez-Puebla, N. Piczonka, S. Sanchez- Cortez, and J. V. Garcia-Ramos, “Surface-enhanced Raman scattering on colloidal nanostructures,” *Advances in Colloid and Interface Science* **116**, 45-61 (2005).

- [45]C. Ungureanu, R. G. Rayavarapu, S. Manohar, and T. G. Van Leeuwen, “Discrete dipole approximation simulations of gold nanorod optical properties: choice of input parameters and comparison with experiment,” *J. Appl. Phys* **105**, 102032 (2009).
- [46]P. K. Jain, K. S. Lee, I. H. El-Sayed, and M. A. El- Sayed, “Calculated absorption and scattering properties of gold nanoparticles of different size, shape, and composition: applications in biological imaging and biomedicine,” *J. Phys. Chem. B* **110**, 7238-7248 (2006).
- [47]A. Brioude, X. C. Jiang, and M. P. Pileni, “Optical properties of gold nanorods: DDA simulations supported by experiments,” *J. Phys. Chem. B* **109**, 13138-13142 (2005).
- [48]T. Kalkbrenner, U. H Akanson, and V. Sandoghdar, “Tomographic plasmon spectroscopy of a single gold nanoparticle,” *Nano Lett* **4**, 2309-2314 (2004).
- [49]T. Ramanathan, S. Stankovich, D. A. Dikin, H. Liu, S. H, S. T. Nguyen, and L. C. Brinson, “Graphitic nanofillers in PMMA nanocomposites: an investigation of particle size and dispersion and their influence on nanocomposite properties,” *J. Polymer. Sci B. Polymer. Phys* **45**, 2097-2112 (2007).
- [50]L. Vaisman, E, Wachtel, H.D Wagner, and G. Marom, “Polymer–nanoinclusion interactions in carbon nanotube based polyacrylonitrile extruded and electrospun fibers,” *Polymer* **48**, 6843-6854 (2007).
- [51]R. Lévy, U. Shaheen, Y. Cesbron, and V. Sée, “Gold nanoparticles delivery in mammalian live cells: a critical review,” *Nano Rev* **1**, 4889 (2010).
- [52]M. M. Lin, H. H Kim, H. Kim, M. Muhammed, and D.K Kim, “Iron oxide-based nanomagnets in nanomedicine: fabrication and applications,” *Nano Rev* **1**, 4883 (2010).

- [53]J. Macanas, J. Parrondo, M. Munoz, S. Alegret, F. Mijangos, and D. N. Muraviev, "Preparation and characterisation of metal-polymer nanocomposite membranes for electrochemical applications," *Phys. Stat. Sol* **204**, 1699-705 (2007).
- [54]J.-J. Zhang, M.-M. Gu, T.-T. Zheng, and J.-J. Zhu, "Synthesis of gelatin-stabilized gold nanoparticles and assembly of carboxylic single-walled carbon nanotubes/Au composites for cytosensing and drug uptake Anal," *Chem* **81**, 6641-6648 (2009).
- [55]Y. Liu, X. Liu, and X. Wang, "Biomimetic synthesis of gelatin polypeptide-assisted noble metal nanoparticles and their interaction stud," *Nanoscale Res. Lett* **6**, 22-32 (2011).
- [56]M. Torres-Cisneros, N. Yanagihara, B. Gonzalez-Rolon, M. A. Meneses-Nava, O.G. Ibarra-Manzano, D. A. May-Arrijo, J. Sanchez-Mondragon, E. Aguilera-Gomez, and L. A. Aguilera-Cortes, "Synthesis and nonlinear optical behavior of Ag nanoparticles in PMMA," *Microelectronics Journal* **40**, 621-623 (2009).
- [57] M. K. Abyaneh, D. Paramanik, S. Varma, S.W. Gosavi, and S. K. Kulkarni, "Formation of gold nanoparticles in polymethylmethacrylate by UV irradiation," *J. Phys. D: Appl. Phys* **40**, 3771-3779 (2007).
- [58]T. Hartling, A. S. Ucker, P. Olk, A. Plettl, P. Ziemann, and L. M. Eng, "Controlled photochemical particle growth in two-dimensional ordered metal nanoparticle arrays," *Nanotechnology* **21**, 145309 (2010).
- [59]E. Yilmaz, G. Ertas, E. Bengu, and S. Suzer, "Photopatterning of PMMA films with gold nanoparticles: Diffusion of AuCl₄ ions," *J. Phys. Chem. C* **14**, 18401-18406 (2010).
- [60]K. J. Sreeram, M. Nidhin, and B. U. Nair, "Microwave-assisted template synthesis of silver nanoparticles," *Bull. Mater. Sci* **31**, 937-942 (2008).

- [61]G.V. Ramesh, K. Sudheendran, K. C. J. Raju, B. Streedhar, and T. P. Radhakrishnan, “Microwave absorber based on silver nanoparticle-embedded polymer thin film,” *J. Nanosci. Nanotechnol* **9**, 261-266 (2009).
- [62]A. Irzh, N. Perkash, and A. Gedanken, “Microwave-assisted coating of PMMA beads by silver nanoparticles,” *Langmuir* **23**, 9891-9897 (2007).
- [63]M. Tsuji, Y. Hashimoto, Y. Nishizawa, M. Kubokawa, and T. Tsuji, “Microwave-assisted synthesis of metallic nanostructures in solution,” *Chem. A Eur. J* **11**, 440-452 (2005).
- [64]M. Bin Ahmad, J.J. Lim, K. Shameli, N.A. Ibrahim, and M.Y. Tay, “Synthesis of silver nanoparticles in chitosan, gelatin and chitosan/gelatin bionanoparticles by a chemical reducing agent and their characterization,” *Molecules* **16**, 7237-7248 (2011).
- [65]M. Alsawafta, S. Badilescu, V.-V. Truong, and M. Packirisamy, “The effect of hydrogen nanobubbles on the morphology of gold–gelatin bionanocomposite films and their optical properties,” *Nanotechnology* **23**, 065305 (2012).
- [66]M. Darroudi, M. Bin Ahmad, A.H. Abdullah, and N.A Ibrahim, “Green synthesis and characterization of gelatin-based and sugar-reduced silver nanoparticles,” *Int. J. Nanomedicine* **6**, 569-574 (2011).
- [67] C. Huang, J. Jiang, M. Lu, L. Sun, E. I. Meletis, and Y. Hao, “Capturing Electrochemically Evolved Nanobubbles by Electroless Deposition. A Facile Route to the Synthesis of Hollow Nanoparticles,” *Nano Lett* **11**, 4297-4301(2009).
- F. Hui, B. Li, P. He, J. Hu, and Y. Fang, “Electrochemical fabrication of nanoporous polypyrrole film on HOPG using nanobubbles as templates,” *Electrochem. Commun* **11**, 639-642 (2009).
- [68]L. Zhang, D. Xia, and Q. Shen, “Synthesis and characterization of Ag@TiO₂ core–shell nanoparticles and TiO₂ nanobubbles,” *J. Nanoparticle Res* **8**, 23-28 (2006).

- [69]Y. Fang, "Optical absorption of nanoscale colloidal silver: aggregate band and adsorbate-silver surface band," J. Chem. Phys **108**, 4315-4318 (1998).
- [70]G. Schmid, *Clusters and colloids: From theory to application* (VCH: Weinheim, 1994).
- [71]J. R. Heath, and J. J. Shiang, "Covalency in semiconductor quantum dots," Chem. Soc. Rev **27**, 65-71 (1998).
- [72]H. S. Nalwa, *Handbook of thin films Materials : Nanomaterials and magnetic thin films* (Academic, 2007).
- [73]T. G. Schaaff, G. Knight, M. N. Shafigullin, R. F. Borkman, and R. L. Whetten, "Isolation and Selected Properties of a 10.4 kDa gold:glutathione cluster compound," J. phys. Chem B **102**, 10643 (1998).
- [74]D. J. Campbell and Y. Xia, "Plasmons: why should we care?," Journal of Chemical Education **84**, 91-96 (2007).
- [75]R. M. Dickson, and L. A. Lyon, "Unidirectional plasmon propagation in metallic nanowires," J. Phys. Chem. B **104**, 6095 (2000).
- [76]A. Kocabas, A. Dâna, and A. Aydinlia, "Excitation of a surface plasmon with an elastomeric grating," Appl. Phys. Lett **89**, 041123 (2006).
- [77]J. R. Sambles, G. W. Bradbery, F. Yang, "Optical excitation of surface plasmons: an introduction," Contemporary physics **32**, 173-183 (1991).
- [78]J. R. Sambles, "Optical excitation of surface plasmons," J. Phys. Chem. Solids **50**, 1-4 (1989).

- [79]S. S. Akarca-Biyikli, I. Bulu, and E. Ozbay, “Resonant excitation of surface plasmons in one-dimensional metallic grating structures at microwave frequencies,” *J. Opt. A: Pure Appl. Opt* **7**, 159-164 (2005).
- [80]T. Inagaki, M. Motosuga, E. T. Arakawa and J. P. Goudonnet, “Coupled surface plasmons in periodically corrugated thin silver films,” *Phys. Rev B* **32**, 1015 (1985).
- [81]X. Lu, M. Rycenga, S. E. Skrabalak, B. Wiley, and Y. Xia, “Chemical synthesis of novel plasmonic nanoparticles,” *Annu. Rev. Phys. Chem* **60**, 167-192 (2009).
- [82]D. P. Fromm, A. Sundaramurthy, P. James Schuck, G. Kino, and W. E. Moerner, “Gap-dependent optical coupling of single “bowtie” nanoantennas resonant in the visible,” *Nano Lett* **4**, 957-961 (2004).
- [83]J. R. Krenn, B. Lamprecht, H. Ditlbacher, G. Schider, M. Salerno, A. Leitner, and F. R. Aussenegg, “Non-diffraction-limited light transport by gold nanowires,” *Europhys. Lett* **60**, 663-669 (2002).
- [84]S. A. Maier, P. G. Kik, H. A. Atwater, S. Meltzer, E. Harel, B. E. Koel, and A. A. G. Requicha, “Local detection of electromagnetic energy transport below the diffraction limit in metal nanoparticle plasmon waveguides,” *Nature Materials* **2**, 229 (2003).
- [85]M. Faraday, “Experimental relations of gold (and other metals) to light,” *Philosophical Transactions of the Royal Society B* **47**, 145-181(1857).
- [86]G. Mie, “Beitrage zur optik truber medien, speziell kolloida ler metallosungen,” *Ann. Physik.* **25**, 377 (1908).
- [87]D. V. Guzatova, V. V. Klimovb and M. Yu. Pikhota, “Plasmon oscillations in ellipsoid nanoparticles: beyond dipole approximation,” *Laser Physics* **20**, 85-99 (2010).

- [88]K. L. Kelly, E. Coronado, L. L. Zhao, and G. C. Schatz, "The optical properties of metal nanoparticles: the influence of size, shape, and dielectric environment," *Phys. Chem. B* **107**, 668 (2003).
- [89]S. Link, and M. A. El-Sayed, "Shape and size dependence of radiative, non-radiative and photothermal properties of gold nanocrystals," *Int. Rev. Phys. Chem* **19**, 409-453 (2000).
- [90]M. M. Alvarez, J. T. Khoury, G. Schaaff, M. N. Shafigullin, I. Vezmar, and R. L. Whetten, "Optical absorption spectra of nanocrystal gold molecules," *Phys. Chem. B* **101**, 3706 (1997).
- [91]A. Pinchuk, G. V. Plessen, and U. Kreibig, "Influence of interband electronic transitions on the optical absorption in metallic nanoparticles," *J. Phys. D: Appl. Phys* **37**, 3133-3139 (2004).
- [92]M. Sastry, M. Rao, and K. N. Ganesh, "Electrostatic assembly of nanoparticles and biomacromolecules," *Acc. Chem. Res* **35**, 847-855 (2002).
- [93]L. B. Scaffardi, and J. O. Toch, "Size dependence of refractive index of gold nanoparticles," *Nanotechnology* **17**, 1309-1315 (2006).
- [94]S. Link, and M. A. El-Sayed, "Size and temperature dependence of the plasmon absorption of colloidal gold nanoparticles," *J. Phys. Chem. B* **103**, 4212-4217 (1999).
- [95]U. Kreibig, and C. V. Fragstein, "The limitation of electron mean free path in small silver particles," *Z. Phys* **224**, 307-323 (1969).
- [96]N. W. Ashcroft, and N. D. Mermin, *Solid State Physics* (Holt-Saunders International Editions: Philadelphia, 1976).
- [97]L. Mulfinger, S. D. Solomon, M. Bahadory, A. V. Jeyarajasingam, S. A. Rutkowsky, and C. Boritz, "Synthesis and study of silver nanoparticles," *J. Chem. Educ* **84**, 322-325 (2007).

- [98]P. B. Johnson and R. W. Christy, "Optical constants of the noble metals," *Phys. Rev B* **6**, 4370-4379 (1972).
- [99]L. Gunnarsson, T. Rindzevicius, J. Prikulis, B. Kasemo, M. Kal, S. Zou, and G. C. Schatz, "Confined plasmons in nanofabricated single silver particle pairs: experimental observations of strong interparticle interactions," *J. Phys. Chem. B* **109**, 1079-1087 (2005).
- [100]Y.-Y. Yu, S.-S. Chang, C.-L. Lee, and C. R. Chris Wang, "Gold nanorods: electrochemical synthesis and optical properties," *J. Phys. Chem. B* **101**, 6661-6664 (1997).
- [101]A. S. Kumbhar, M. K. Kinnan, and G. Chumanov, "Multipole plasmon resonances of submicron silver particles," *J. Am. Chem. Soc* **127**, 12444-12445 (2005).
- [102]J. Lermé, "Size evolution of the surface plasmon resonance damping in silver nanoparticles: confinement and dielectric effects," *J. Phys. Chem. C* **115**, 14098-14110 (2011).
- [103]H. Hovel, S. Fritz, A. Hilger, U. Kreibig and M. Vollmer, "Width of cluster plasmon resonance: Bulk dielectric function and chemical interface damping," *Phys. Rev* **24**, 18178–18188 (1993).
- [104]E. A. Coronado, and G. C. Schatz, "Surface plasmon broadening for arbitrary shape nanoparticles: A geometrical probability approach," *J. Chem. Phys* **119**, 3926-3932 (2003).
- [105]U. Kreibig, and M. Vollmer, *Optical properties of metal clusters* (Springer, 1995).
- [106]G. Barbillon, J.-L. Bijeon, J. Plain, M. Lamy de la Chapelle, P.-M. Adam, and P. Royer, "Biological and chemical nanosensors based on localized surface plasmon resonance," *Gold Bull* **40**, 240-244 (2007).

- [107]M. Alsawafta, S. Badilescu, A. Paneri, V.-V. Truong, and M. Packirisamy, “Gold-poly(methyl methacrylate) nanocomposite films for plasmonic biosensing applications,” *Polymers* **3**, 1833-1848 (2011).
- [108]M. D. Malinsky, K. L. Kelly, G. C. Schatz, and R. P. Van Duyne, “Nanosphere lithography: effect of substrate on the localized surface plasmon resonance spectrum of silver nanoparticles,” *J. Phys. Chem. B* **105**, 2343-2350 (2001).
- [109]E. Ringe, J. M. McMahon, K. Sohn, C. Cobley, Y. Xia, J. Huang, G. C. Schatz, L. D. Marks, and R. P. Van Duyne, “Unraveling the effects of size, composition, and substrate on the localized surface plasmon resonance frequencies of gold and silver nanocubes: a systematic single-particle approach,” *J. Phys. Chem. C* **114**, 12511-12516 (2010).
- [110]P. K. Jain, and M. A. El-Sayed, “Noble metal nanoparticle pairs: effect of medium for enhanced nanosensing,” *Nano Lett* **8**, 4347-4352 (2008).
- [111]V. Amendola, O. M Bakr, and F. Stellacci, “A study of the surface plasmon resonance of silver nanoparticles by the discrete dipole approximation method: effect of shape, size, structure, and assembly,” *Plasmonics* **5**, 85-97 (2010).
- [112]J. J. Mock, M. Barbic, D. R. Smith, D. A. Schultz, and S. Schultz, “Shape effects in plasmon resonance of individual colloidal silver nanoparticles,” *J. Chem. Phys* **116**, 6755-6760 (2002).
- [113]S. A. Maier, M. L. Brongersma, P. G. Kik, and H. A. Atwater, “Observation of near-field coupling in metal nanoparticle chains using far-field polarization spectroscopy,” *Phys. Rev B* **65**, 193408 (2002).
- [114]Y. Tanaka, G. Obara, A. Zenidaka, N. N Nedyalkov, M. Terakawa, and Minoru Obara, “Near-field interaction of two-dimensional high-permittivity spherical particle arrays on substrate in the Mie resonance scattering domain,” *Opt. Exp* **18**, 27228 (2010).

[115]W. Rechberger, A. Hohenau, A. Leitner, J. R. Krenn, B. Lamprecht, and F.R. Aussenegg, "Optical properties of two interacting gold nanoparticles," *Opt. Comm* **220**, 137-141 (2003).

[116]M. K. Kinnan and G. Chumanov, "Plasmon coupling in two-dimensional arrays of silver nanoparticles: ii. effect of the particle size and interparticle distance," *J. Phys. Chem. C* **144**, 7496-7501 (2010).

[117]J. Sung, E. M. Hicks, R. P. Van Duyne, and K. G. Spears, "Nanoparticle spectroscopy: plasmon coupling in finite-sized two-dimensional arrays of cylindrical silver nanoparticles," *J. Phys. Chem. C* **112**, 4091-4096 (2008).

[118]C. F. Bohren, and D. R. Huffman, *Absorption and Scattering of Light by Small Particles* (Wiley, 1983).

[119]M. I. Mishchenko, L.D. Travis, and D.W. Mackowski, "T-matrix computations of light scattering by nonspherical particles: A review," *JQSRT* **55**, 535-575 (1996).

[120]P. Yang, and K. N. Liou, "Finite difference time domain method for light scattering by nonspherical and inhomogeneous particles," in *Light Scattering by Nonspherical Particles: Theory, Measurements, and Applications*, M. I. Mishchenko, J. W. Hovenier, and L. D. Travis, (Academic, 2000), pp.173-221

[121]H. DeVoe, "Optical properties of molecular aggregates. I. Classical model of electronic absorption and refraction," *J. Chem. Phys* **41**, 393-400 (1964).

[122]H. DeVoe, "Optical properties of molecular aggregates. II. Classical theory of the refraction, absorption, and optical activity of solutions and crystals," *J. Chem. Phys* **43**, 3199-3208 (1965).

- [123]E. M. Purcell and C. R. Pennypacker, "Scattering and absorption of light by nonspherical dielectric grains," *Astrophys. J* **186**, 705-714 (1973).
- [124]B.T. Drain, "The discrete-dipole approximation and its application to interstellar graphite grains," *Amer. Astro. Soc* **333**, 848-872 (1988).
- [125]C. Noguez, "Optical properties of isolated and supported metal nanopart," *Opt. Mat* **27**, 1204-1211 (2005).
- [126]Q. Zhang, W. Li, L. P. Wen, J. Chen, and Y. Xia, "Facile synthesis of Ag nanocubes of 30 to 70 nm in edge length with CF₃COO Ag as a precursor," *Chem-A Euro. J* **16**, 10234-10239 (2010).
- [127]X. Wu, T. Ming, X. Wang, P. Wang, J. Wang, and J. Chen, "High-photoluminescence yield gold nanocubes: for cell imaging and photothermal therapy," *ACS Nano* **4**, 113-120 (2010).
- [128]W. Caseri, "Inorganic nanoparticles as optically effective additives for polymers," *Chem Eng Comm* **196**, 549-572 (2009).
- [129]J. M. Petroski, Z. L. Wang, T. C. Green, and M. El-Sayed, "Kinetically controlled growth and shape formation mechanism of platinum nanoparticles," *J. Phys. Chem. B* **102**, 3316-3320 (1998).
- [130]M. Tsuji, M. Hashimoto, Y. Nishizawa, M. Kubokawa, and T. Tsuji, "Microwave-assisted synthesis of metallic nanostructures in solution," *Chem. Eur. J* **11**, 440-452 (2005).
- [131]Y. Sun and Y. Xia, "Shape-controlled synthesis of gold and silver nanoparticles," *Science*, **298**, 2176-2179 (2002).

- [132]F.K. Liu, P.W. Huang, T.C. Chu, and F.H. Ko, "Gold seed-assisted synthesis of silver nanomaterials under microwave heating," *Mater Lett* **59**, 940 (2005).
- [133]M. B. Ahmad, K. Shameli, W. M. Yunus, N. A. Ibrahim, and M. Darroudi, "Synthesis and characterization of silver/clay/starch bionanocomposites by green method," *Aust. J. Basic & Appl. Sci* **4**, 2158-2165 (2010).
- [134]M. D. Malinsky, K. L. Kelly, G. C. Schatz, and R. P. Van Duyne, "Chain length dependence and sensing capabilities of the localized surface plasmon resonance of silver nanoparticles chemically modified with alkanethiol self-assembled monolayers," *J. Am. Chem. Soc* **123**, 1471 (2001).
- [135]L.S. Jung, C. T. Campbell, T. M. Chinowsky, M. N. Mar, and S. S. Yee, "Quantitative interpretation of the response of surface plasmon resonance sensors to adsorbed films," *Langmuir* **14**, 5636 (1998).
- [136]X. Huang, H. Wu, X. Liao, and B. Shi, "One-step, size-controlled synthesis of gold nanoparticles at room temperature using plant tannin," *Green Chem* **12**, 395-399 (2010).
- [137]M. P. Neupane, S. J. Lee, I. S. Park , M. H. Lee , T. S. Bae, Y. Kuboki, M. Uo, and F. Watari, "Synthesis of gelatin-capped gold nanoparticles with variable gelatin concentration," *J Nanopart Res* **13**, 491-498 (2011).
- [138]K. Kima, T. Kimb, K. Leec, and S. Kwon, "Fuel cell system with sodium borohydride as hydrogen source for unmanned aerial vehicles, *Journal of Power Sources*," **196**, 9069-9075 (2011).
- [139]J. Yamabe, and S. Nishimura, "Influence of fillers on hydrogen penetration properties and blister fracture of rubber composites for O-ring exposed to high-pressure hydrogen gas," *Inter. J. Hydrogen Energy* **34**, 1977-1989 (2009).

- [140]Y. Wang, B. Bhushan, and X, Zhao, “Nanoindentations produced by nanobubbles on ultrathin polystyrene films in water,” *Nanotechnology* **20**, 045301 (2009).
- [141]B. Song, W. Walczyk, and H. Schönherr, “Contact angles of surface nanobubbles on mixed self-assembled monolayers with systematically varied macroscopic wettability by atomic force microscopy,” *Langmuir* **27**, 8223-8232 (2011).
- [142]T.D. Blake, and J.A. Kitchener, “Stability of aqueous films on hydrophobic methylated silica,” *J. Chem. Soc. Faraday Trans 1*, 1435-1442 (1972).
- [143]S. Ljunggren, J. C. Eriksson, *colloids surf*, “The lifetime of a colloid-sized gas bubble in water and the cause of the hydrophobic attraction,” *Colloids Surfaces A: Physicochem. Eng. Aspects* **129**, 151-155 (1997).
- [144]M. A. Hampton, and A. V. and Nguyen, “Nanobubbles and the nanobubble bridging capillary force,” *Adv. Coll. Interf. Sci* **1**, 1-19 (2010).
- [145]J. R. T. Seddon and D. Lohse, “Nanobubbles and micropancakes: gaseous domains on immersed substrates,” *J. Phys.: Condens. Matter* **23**, 133001 (2010).
- [146]J. P. Chen, and L. L. Lim, “Key factors in chemical reduction by hydrazine for recovery of preciousmetals,” *Chemosphere* **49**, 363-370 (2002).
- [147]D. Philip, “Synthesis and spectroscopic characterization of gold nanoparticles,” *Spectrochim Acta A* **71**, 80-85 (2007).
- [148]J. W. Yang, J. M. Duan, D. Fornasiero, and J. Ralston, “Very small bubble formation at the solid–water interface,” *J. Phys. Chem. B* **107**, 6139-6147 (2003).

[149]B. Bhushan, Y. Wang, and A. Maali, “ Coalescence and movement of nanobubbles studied with tapping mode AFM and tip–bubble interaction analysis,” *J. Phys.: Condens. Matter* **20**, 485004 (2008).

[150]A. C. Simonsen, P. L. Hansen, and B. Klosgen, “Nanobubbles give evidence of incomplete wetting at a hydrophobic interface,” *J. Colloid Interface Sci* **273**, 291-299 (2004).

[151]N. Ishida, T. Inoue, M. Miyahara, and K. Higashitani, “ Nano bubbles on a hydrophobic surface in water observed by tapping-mode atomic force microscopy,” *Langmuir* **16**, 6377-6380 (2000).

[152]J. Drelich, and J. D. Miller, “The effect of surfaceheterogeneity on pseudo-linetension and the flotationlimit of fineparticles,” *Colloids Surf* **69**, 35-43 (1992).

[153]M. P. Brenner, and D. Lohse, “Dynamic equilibrium mechanism for surface nanobubble stabilization,” *Phys. Rev. Lett* **101**, 214505 (2008).

[154]X. H. Zhang, X. D. Zhang, S. T. Lou, Z. X. Zhang, J. L. Sun, and J. Hu, “Degassing and Temperature effects on the formation of nanobubbles at the mica/water interface,” *Langmuir* **20**, 3813-3815 (2004).

[155]X. H. Zhang, A. Khan, and W. A. Ducker, “A nanoscale gas state,” *Phys. Rev. Lett* **98**, 136101 (2007).